Doctoral Dissertation

# Preparation and Applications of Smart Composite Hydrogels Using Cellulose

# セルロースを用いたスマート複合ハイドロゲルの創製と応用

WANG JUAN

July 2024

Graduate School of Engineering
Osaka University

**General Introduction** **1**

References 11

**Chapter 1**

**Cellulose Luminescent Hydrogels Loaded with Stable Carbon Dots for Duplicable Information Encryption and Anti-counterfeiting** **13**

1.1 Introduction **13**

1.2 Experimental Section **16**

1.3 Results and discussion **21**

1.4 Conclusion **34**

1.5 References **35**

**Chapter 2**

**Rapid Preparation of Dynamic-Crosslinked Cellulose Nanocomposite Hydrogel Sensors with Efficient Self-healing and Adhesion Properties** **39**

2.1 Introduction **39**

2.2 Experimental Section **42**

2.3 Results and Discussion **48**

2.4 Conclusions **64**

2.5 References **64**

**Chapter 3**

**Smart versatile hydrogels tailored by metal-phenolic coordinating carbon and polypyrrole for soft actuation, strain sensing and writing recognition** **68**

3.1 Introduction **68**

3.2 Materials and methods **71**

3.3 Results and Discussion **78**

3.4 Conclusions **92**

3.5 References **92**

**Concluding remarks** **96**

**List of Publications** **99**

**Acknowledgments** **100**

# General Introduction

## Hydrogels overview

Hydrogels are a class of soft materials with a three-dimensional (3D) networks structure formed by hydrophilic polymer chains embedded in a water-rich environment, possessing highly tunable physicochemical properties,[1] have emerged as promising candidate materials in various fields such as electronic skins, wearable sensors, human-machine interaction systems, bioengineering, information storage, and soft robotics.[2] Various natural polymers and its derivatives (protein, alginate, cellulose, chitosan, *etc.*) as well as synthetic polymers (polyacrylamide, polyvinyl alcohol, polyethylene glycol, etc.) can be processed into hydrogels through chemical or physical cross-linking methods (**Figure 1**). In chemically crosslinked hydrogels, polymer chains form strong and permanent covalent bonds, providing high stability, good mechanical properties, and adjustable degradation behavior under physiological conditions.[3] Physically crosslinked hydrogels are mostly formed through intermolecular reversible non-covalent interactions, such as ionic/electrostatic interactions, host-guest interactions, hydrophobic/hydrophilic interactions, hydrogen bonding, metal coordination, and π-π stacking. Compared to chemical crosslinking, physical crosslinking offers biocompatibility, as it avoids potentially cytotoxic chemical crosslinkers, and provides certain self-healing and stimuli-responsive properties at room temperature.[4] In recent years, researchers have also developed hydrogel networks through

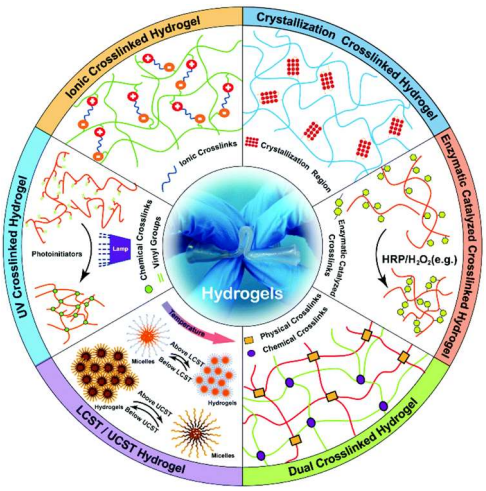


**Figure 1.** Various crosslinking methods for hydrogel formation including physical crosslinking, chemical crosslinking and hybrid crosslinking.[3]

dynamic crosslinking by forming dynamic covalent bonds, such as disulfide bonds[5, 6], boronate ester bonds[7, 8], imine bonds (Schiff bases)[9, 10], and acylhydrazone bonds[11, 12]. Additionally, many nanomaterials such as silica nanoparticles[13], carbon nanotubes (CNTs)[14], graphene[15], graphene oxide (GO)[16], cellulose nanorods[17] and nano clays[18] can interact with polymer chains through various interactions and can also serve as macro-crosslinking points to form nanocomposite hydrogels. As a result, a well-designed crosslinked network endows hydrogel materials with excellent physical and chemical properties.[19] Due to the broad development prospects in applications such as biology, robotics, and electronic skin, stimuli-responsive hydrogels and conductive hydrogels are the most popular and discussed research directions.[20]

**Stimuli-responsive hydrogels**

Stimuli-responsive hydrogels, also known as "smart" hydrogels, can reversibly respond to various external stimuli such as temperature, pH, light, and electromagnetic fields, resulting in changes to their morphology, structure, or properties in the environmental condition (**Figure 2**).[19, 21] These smart hydrogels are widely used in the development of bio-inspired actuators, drug delivery systems, on-off switches, artificial muscles, information storage and anti-counterfeiting.[22] For instance, Li *et al.* synthesized a highly fluorescent hydrogel that is pH-sensitive by copolymerizing a monomer containing naphthalimide-based fluorophore with acrylamide. The fluorescence of this hydrogel could be quenched by $OH^-$ ions in a controlled behavior, both spatially and

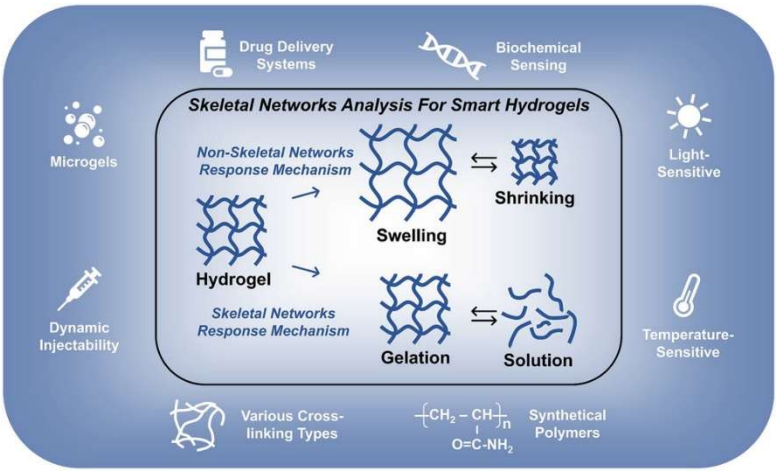


**Figure 2.** An analysis of skeletal networks in smart hydrogels.[19]

temporally. This property enabled the use of ion-transfer-printing to locally control fluorescence, embedding high-precision patterns into the hydrogel. In addition, these patterns are invisible under daylight and only appear under specific UV light, thus achieving a process for information encryption and decryption.[23] Bao *et al.* introduced the thermally responsive monomer *N*-isopropylacrylamide (NIPAM) into the hydrogel backbone to mitigate secondary skin damage when peeling off adhesive electrodes. They designed a smart hydrogel "bandage" with on-demand adhesion and detachment at the skin interface. This hydrogel exhibits adhesive strength that decreases by two orders of magnitude at high temperatures compared to low temperatures. It provides good adhesion during treatment but can be easily and gently removed with slight heating.[24]

**Conductive hydrogels**

Compared to metals, carbon, and conjugated polymers, ordinary hydrogels are usually considered non-conductive due to their low electrical conductivity, which is less than a few Siemens per meter, similar to that of saline water.[2] Therefore, the design principle of conductive hydrogels is to introduce conductive phases such as liquid metals, carbon, conductive polymers, and high concentrations of salt ions into the hydrogel matrix to impart electrical conductivity. This integration enables the hydrogel to transduce mechanical stimuli (*e.g.*, pressure and strain) into electrical signals (*e.g.* resistance, current, or capacitance signals) with high precision. Consequently, this capability is essential for applications in flexible strain sensors, bioelectrodes, and supercapacitors, allowing for accurate signal detection and measurement.[25] For instance, Someya *et al.* developed a skin-applicable conductive bio hydrogel based on natural gelatin, utilizing an ionic conductivity mechanism. This innovation enabled stable contact between the gel electrodes and hairy scalp, facilitating long-term, high-quality electroencephalogram (EEG) monitoring.[26] Lei *et al.* developed single-network and multi-

network hydrogels based on water-soluble N-type cationic semiconductor polymers, endowing traditional hydrogels with unique semiconductor properties. These semiconductor hydrogels, which exhibit good bio-adhesiveness and biocompatibility, can be used to fabricate low-power and high-gain complementary logic circuits and signal amplifiers, and can sense and amplify various electrophysiological signals in bioelectronics.[27]

The methods for preparing conductive hydrogels generally including: (1) constructing a single-component network through the self-assembly or self-polymerization of rigid electronic conductors/conductive polymers; (2) forming interpenetrating networks by combining rigid electronic conductors/conductive polymers with stretchable gels; and (3) doping the hydrogel matrix with free or crosslinked mobile ions or ionic polymers.[28] (**Figure 3**). Based on conductive mechanisms, the prepared hydrogels can be classified as electronic, ionic, or hybrid electronic-ionic conductive hydrogels. Hydrogels based on rigid electronic conductors as conductive fillers (*e.g.*, liquid metals, MXene, CNTs, graphene) primarily rely on the electronic conduction of the fillers. These conductive fillers not only establish stable contact with the gel network but also ensure more efficient electron transport paths through contact junctions formed at various angles between the fillers.[29] Similarly, conductive polymer-based hydrogels also primarily rely on electronic conduction, where the conductivity originates from the conjugated π bonds of conductive polymers such as polyaniline (PANI), polypyrrole (PPy), polythiophene (PT), and poly(3,4-ethylenedioxythiophene) (PEDOT). For ionically conductive hydrogels, conductivity arises from the migration of free-moving or cross-linked ions, where ions act as charge carriers, and the three-dimensional gel

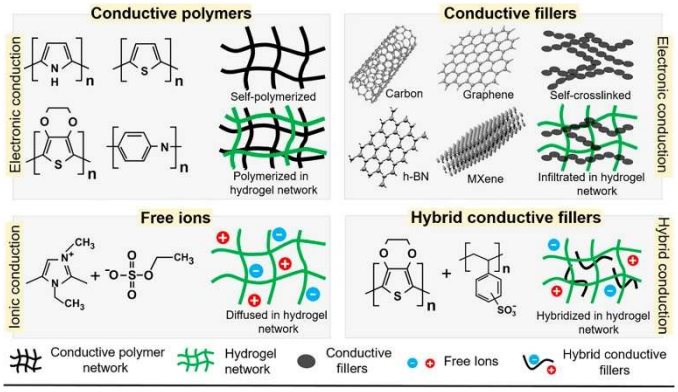


**Figure 3.** Various types of conductive hydrogel structures.[27]

network structure serves as the ion migration pathway.[30] Importantly, many hydrogels exhibit both electronic and ionic conductivity.[31] For instance, poly(styrene sulfonate) (PSS) doped PEDOT (PEDOT:PSS) hydrogels fall under the category of hybrid electronic-ionic conductive hydrogels due to the presence of the charge-conducting PEDOT backbone and the ion-conducting PSS chains.[32]

**Cellulose hydrogels**

As previously mentioned, natural polymers and their derivatives are widely used in constructing hydrogel networks due to biocompatibility, degradability, and the abundance of reactive sites on their molecular chains. (**Figure 4**). Amongst them, cellulose is the most abundant natural polymer on earth, derived from renewable plants such as wood, cotton, flax, and from bacteria like *acetobacter xylinum*, making it low-cost and sustainable.[33] As shown in **Figure 4**, cellulose consists of linear chains of *β*-(1,4)-linked *d*-glucose units, ranging from partially crystalline to fully crystalline, and is almost insoluble in most organic solvents and water because of the high inter and intramolecular hydrogen bonding and van der Waals forces.[34, 35] To address the solubility limitations and expand the application range of cellulose, researchers have developed a few solvent systems to dissolve cellulose, such as ionic liquids[36], alkali/urea[37], and alkali/thiourea[38]. Additionally, cellulose derivatives obtained by partial esterification or

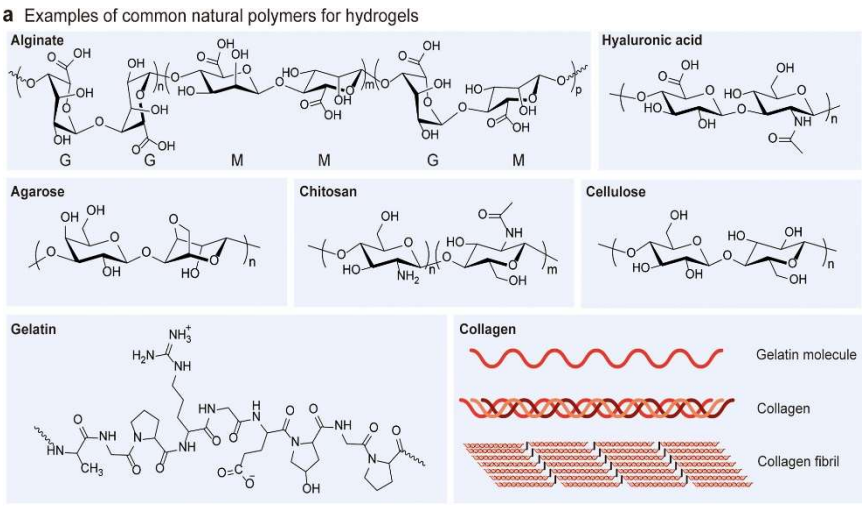


**Figure 4.** Chemical structure schematics of common natural polymers used for hydrogel fabrication.[2]

etherification of hydroxyl groups on the cellulose backbone (such as hydroxypropyl cellulose, methyl cellulose, hydroxypropyl methylcellulose, carboxymethyl cellulose, *etc*.) are easier to dissolve and process.

Because cellulose contains a large number of hydroxyl functional groups, the gel network can be easily prepared directly from natural cellulose solutions. Suenaga *et al*. achieved the gelation of cellulose nanofibers (CNF) without the need for chemical crosslinkers or any chemical modification by using pulverization process and hydrothermal gelation method. The prepared CNF hydrogel belong to a physical gel, and the network structure is likely formed through simple attractive forces, such as van der Waals forces.[39] Cellulose and its derivatives can be used to prepare hydrogels with stable structures through chemical cross-linking. Functional molecules such as carboxylic acids, acid anhydrides, organic chlorides, epoxides, and vinyl compounds serve as chemical cross-linkers, forming covalent ester or ether bonds between the main chains. For instance, Demitri *et al*. demonstrated that superabsorbent hydrogels of hydroxyethyl cellulose/sodium carboxymethyl cellulose can be prepared using citric acid as a crosslinker, providing a green approach for the design of novel environmentally friendly hydrogels.[40] Zhou *et al*. dissolved cellulose powder in NaOH/urea aqueous solution and used epichlorohydrin as a crosslinker to synthesize a chemically crosslinked cellulose hydrogel in one step. This hydrogel exhibited good water absorption capacity and transparency.[41] Covalent bonds between cellulose chains can also be formed through radiation crosslinking methods (electron beam and γ-rays), which avoid the use of toxic crosslinkers and simultaneously sterilize the resulting hydrogels. Notably, bacterial cellulose can directly form cellulose hydrogels with high purity, high crystallinity, and stable mechanical properties, expanding the applications of cellulose hydrogels in medical fields such as micro vessels, tissue engineering scaffolds, and soft tissue materials.[42, 43]

However, hydrogels prepared directly from natural cellulose are often limited by weak

mechanical properties, complex solvent systems and conditions, and poor tunability of structure and performance.[44] Composites of cellulose and its derivatives with other polymers, forming interpenetrating polymer network (IPN) hydrogels, can partially overcome these limitations by combining the advantages of both components, thus enhancing the mechanical and processing properties of the hydrogels. These polymers include synthetic polymers such as polyvinyl alcohol (PVA), polyethylene glycol (PEG), polyacrylic acid (PAA), and natural polymers such as starch, alginate, chitosan, and hyaluronic acid.[33] Zhao *et al*. prepared a chitosan/cellulose composite hydrogel, combining the excellent mechanical properties of cellulose with the outstanding antibacterial properties and biocompatibility of chitosan, and has potential applications in facial masks and antibacterial packaging.[45] Chang *et al*. used cellulose hydrogel as the first network, and then in-situ radical polymerized/crosslinked *N*-isopropylacrylamide (NIPAM) within the hydrogel network to form the second network, creating an IPN hydrogel (**Figure 5**). This hydrogel exhibited high mechanical strength and adjustable thermal sensitivity.[46]

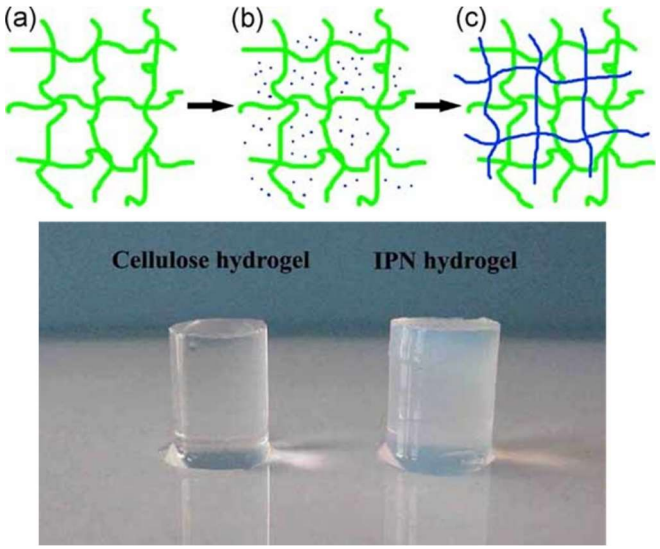


**Figure 5.** The method and photographs of cellulose/PNIPAM IPN hydrogel.[46]

On top of that, in critical applications such as electrochemical sensors and tissue engineering, achieving robust mechanical properties simply in hydrogels cannot meet actual needs. Firstly, hydrogels need to exhibit excellent elasticity and self-recovery to ensure they maintain their performance under large cyclic stress.[47] Secondly, inevitable cracking may occur during the use of gel materials, and self-healing functionality enables the gel to repair itself after

damage, thereby preserving structural and functional integrity and extending the material's lifespan.[48] Therefore, synchronously achieving essential multifunctionality within the same hydrogel remains a challenge.

**Outline of this thesis**

In this dissertation, the author incorporated biomass cellulose into polymer matrices to prepare three types of smart hydrogel sensors with excellent physical properties, and investigated the applications in information storage, strain sensors, and actuators. This thesis is expected to provide new avenues for the development of next-generation smart anti-counterfeiting materials, intelligent information storage and recognition devices, flexible electronic health monitoring equipment, and soft robotics.

**Chapter 1**

To overcome the shortcomings of nanoparticle leaching, avoiding the migration of CDs outside the gel when swollen, a facile fabrication of chemistry bonding fluorescent nanocomposite hydrogel based on green-synthesized CDs and fibrillated citric acid-modified cellulose (F-CAC) was reported in this chapter. Through the stupendous chemical interaction between the CDs and F-CAC, CDs/F-CAC was incorporated into a biocompatible, flexible hydrogel matrix of acrylamide (AAm) and the hydroxyethyl methyl acrylate (HEMA) copolymer, P(AAm-*co*-HEMA). The CDs/F-CAC not only significantly improved the mechanical properties and anti-fatigue performance of P(AAm-*co*-HEMA) but also endowed the hydrogels with excellent fluorescence properties. Satisfyingly, the fluorescence of the CDs/F-CAC hydrogels was quenched by $Fe^{3+}$ ions and recovered in an ascorbic acid/EDTA-2Na mixture solution. Thus, the as-prepared display platform of fluorescent hydrogel via ionoprinting technique could be used repeatedly.

**Chapter 2**

In this chapter, a multi-functional hydrogel-based flexible sensor was developed through an "one-pot" strategy benefiting from lignin sulfonate (LS)-metal ions ($Fe^{3+}$) dynamic redox system and reversible non-covalent cross-linking formed between 3-acrylamidophenyboronic acid (APBA) and cellulose nanocrystals (CNC). In detail, the LS-$Fe^{3+}$ dynamic catalytic system resulted in rapid copolymerization of acrylamide (AM), sodium acrylate (AAS) and APBA at room temperature in the presence of ammonium persulfate (APS) as the initiator. The synergistic interactions of massive hydrogen bonding, the boronic ester bond between APBA and CNC as well as the metal-ligand complexation of $Fe^{3+}$ and polymer chain endowed the hydrogel with reliable and efficient self-healing properties. The AAS offered physical crosslinking sites, contributing to the significant toughness and anti-fatigue performance. Apart from facilitating the rapid preparation system, an appropriate amount of LS avoided implosion as a dispersant and enhanced mechanical strength. Furthermore, the intermediate catechol groups generated by LS enabled the hydrogel with repeatable self-adhesive behavior.

**Chapter 3**

In this chapter, the author proposed a versatile conductive composite hydrogel with integrated near-infrared light (NIR)-driven deformation and strain sensing behaviors by combining a synthetic process of incorporation of metal-organic coordination bond into carbon nanotubes with a post in-situ polymerization. Specifically, the $Fe^{3+}$-tannic acid (TA) complex-modified single-walled nanotubes (Fe-TA@SWNT) was introduced into a hydrogel network composed of carboxymethylcellulose (CMC), copolymer of acrylic acid (AA) and [2-(methacryloyloxy) ethyl]dimethyl-(3-sulfopropyl) ammonium hydroxide (SBMA) (P(AA-SBMA)), followed by in-situ polymerization of polypyrrole (PPy) in the hydrogel network using Fe-TA@SWNT, CMC, and P(AA-SBMA) as the skeletons. Through the synergistic interactions of chemical cross-linking bonds and various dynamic bonds (hydrogen bonds, ion

coordination bonds, cation-π interactions, and electrostatic interactions), the prepared hydrogel exhibited significant stretchability, toughness, self-recovery, and repeatable self-adhesive properties. Moreover, the NIR photothermal effect exhibited by Fe-TA@SWNT and PPy, in conjunction with the interconnected conductive channels formed, enabled the integration of sensing and actuation functionalities within the hydrogel.

## References


1. Y. S. Zhang and A. Khademhosseini, *Science*, 2017, **356**, eaaf3627.
2. X. Zhao, X. Chen, H. Yuk, S. Lin, X. Liu and G. Parada, *Chem. Rev.*, 2021, **121**, 4309-4372.
3. W. Hu, Z. Wang, Y. Xiao, S. Zhang and J. Wang, *Biomater. Sci.*, 2019, **7**, 843-855.
4. B.-X. Wang, W. Xu, Z. Yang, Y. Wu and F. Pi, *Macromol. Rapid Commun.*, 2022, **43**, 2100785.
5. H. Yang, X. Chen, B. Sun, J. Tang and J. J. Vlassak, *J. Mech. Phys. Solids*, 2022, **169**, 105083.
6. X. Dou, Q. Cao, F. Sun, Y. Wang, H. Wang, H. Shen, F. Yang, X. Wang and D. Wu, *Sci. China Chem.*, 2020, **63**, 1793-1798.
7. M. Ma, J. Yang, Z. Ye, A. Dong, J. Zhang and J. Zhang, *Macromol. Mater. Eng.*, 2021, **306**, 2000577.
8. X. Le, W. Lu, J. Zheng, D. Tong, N. Zhao, C. Ma, H. Xiao, J. Zhang, Y. Huang and T. Chen, *Chem. Sci.*, 2016, **7**, 6715-6720.
9. H. Li, F. Liu, Z. Li, S. Wang, R. Jin, C. Liu and Y. Chen, *ACS Appl. Mater. Interfaces*, 2019, **11**, 17925-17930.
10. J. Kumankuma-Sarpong, C. Chang, J. Hao, T. Li, X. Deng, C. Han and B. Li, *Adv. Mater.*, 2024, **n/a**, 2403214.
11. G. Deng, C. Tang, F. Li, H. Jiang and Y. Chen, *Macromolecules*, 2010, **43**, 1191-1194.
12. Z. Li, F. Zhou, Z. Li, S. Lin, L. Chen, L. Liu and Y. Chen, *ACS Appl. Mater. Interfaces*, 2018, **10**, 25194-25202.
13. J. Zheng, P. Xiao, W. Liu, J. Zhang, Y. Huang and T. Chen, *Macromol. Rapid Commun.*, 2016, **37**, 265-270.
14. R. Du, J. Wu, L. Chen, H. Huang, X. Zhang and J. Zhang, *Small*, 2014, **10**, 1387-1393.
15. S. Das, F. Irin, L. Ma, S. K. Bhattacharia, R. C. Hedden and M. J. Green, *ACS Appl. Mater. Interfaces*, 2013, **5**, 8633-8640.
16. J. Liu, G. Song, C. He and H. Wang, *Macromol. Rapid Commun.*, 2013, **34**, 1002-1007.
17. J. R. McKee, E. A. Appel, J. Seitsonen, E. Kontturi, O. A. Scherman and O. Ikkala, *Adv. Funct. Mater.*, 2014, **24**, 2706-2713.
18. K. Haraguchi, K. Uyama and H. Tanimoto, *Macromol. Rapid Commun.*, 2011, **32**, 1253-1258.
19. H. Sun, Y. He, Z. Wang and Q. Liang, *Adv. Funct. Mater.*, 2022, **32**, 2108489.
20. Y. Liu, Z. Zhang, Z. Liang, Y. Yong, C. Yang and Z. Li, *J. Mater. Chem. A*, 2022, **10**, 16928-16940.
21. Z. Hao, X. Li, R. Zhang and L. Zhang, *Adv. Healthcare Mater.*, 2024, **n/a**, 2400513.
22. H. Li, Y. Liang, G. Gao, S. Wei, Y. Jian, X. Le, W. Lu, Q. Liu, J. Zhang and T. Chen, *Chem. Eng. J.*, 2021, **415**, 128988.
23. P. Li, D. Zhang, Y. Zhang, W. Lu, J. Zhang, W. Wang, Q. He, P. Théato and T. Chen, *ACS Macro Lett.*, 2019, **8**, 937-942.
24. Y. Jiang, A. A. Trotsyuk, S. Niu, D. Henn, K. Chen, C.-C. Shih, M. R. Larson, A. M. Mermin-Bunnell, S. Mittal, J.-C. Lai, A. Saberi, E. Beard, S. Jing, D. Zhong, S. R. Steele, K.

Sun, T. Jain, E. Zhao, C. R. Neimeth, W. G. Viana, J. Tang, D. Sivaraj, J. Padmanabhan, M. Rodrigues, D. P. Perrault, A. Chattopadhyay, Z. N. Maan, M. C. Leeolou, C. A. Bonham, S. H. Kwon, H. C. Kussie, K. S. Fischer, G. Gurusankar, K. Liang, K. Zhang, R. Nag, M. P. Snyder, M. Januszyk, G. C. Gurtner and Z. Bao, *Nat. Biotechnol.*, 2023, **41**, 652-662.
25. Z. Qin, G. Zhao, Y. Zhang, Z. Gu, Y. Tang, J. T. Aladejana, J. Ren, Y. Jiang, Z. Guo, X. Peng, X. Zhang, B. B. Xu and T. Chen, *Small*, 2023, **19**, 2303038.
26. C. Wang, H. Wang, B. Wang, H. Miyata, Y. Wang, M. O. G. Nayeem, J. J. Kim, S. Lee, T. Yokota, H. Onodera and T. Someya, *Sci. Adv.*, **8**, eabo1396.
27. P. Li, W. Sun, J. Li, J.-P. Chen, X. Wang, Z. Mei, G. Jin, Y. Lei, R. Xin, M. Yang, J. Xu, X. Pan, C. Song, X.-Y. Deng, X. Lei, K. Liu, X. Wang, Y. Zheng, J. Zhu, S. Lv, Z. Zhang, X. Dai and T. Lei, *Science*, 2024, **384**, 557-563.
28. F. Fu, J. Wang, H. Zeng and J. Yu, *ACS Mater. Lett.*, 2020, **2**, 1287-1301.
29. X. Zhou, X. Zhao, Y. Wang, P. Wang, X. Jiang, Z. Song, J. Ding, G. Liu, X. Li, W. Sun and W. Xu, *Composites, Part B*, 2023, **255**, 110631.
30. C. Yang and Z. Suo, *Nat. Rev. Mater.*, 2018, **3**, 125-142.
31. J. Chung, A. Khot, B. M. Savoie and B. W. Boudouris, *ACS Macro Lett.*, 2020, **9**, 646-655.
32. L. V. Kayser and D. J. Lipomi, *Adv. Mater.*, 2019, **31**, 1806133.
33. Z. Wang, H. Wei, Y. Huang, Y. Wei and J. Chen, *Chem. Soc. Rev.*, 2023, **52**, 2992-3034.
34. K. J. De France, T. Hoare and E. D. Cranston, *Chem. Mater.*, 2017, **29**, 4609-4631.
35. S. H. Zainal, N. H. Mohd, N. Suhaili, F. H. Anuar, A. M. Lazim and R. Othaman, *J. Mater. Res. Technol.*, 2021, **10**, 935-952.
36. H. Zhang, J. Wu, J. Zhang and J. He, *Macromolecules*, 2005, **38**, 8272-8277.
37. J. Cai and L. Zhang, *Biomacromolecules*, 2006, **7**, 183-189.
38. S. Liang, L. Zhang, Y. Li and J. Xu, *Macromol. Chem. Phys.*, 2007, **208**, 594-602.
39. S. Suenaga and M. Osada, *ACS Appl. Polym. Mater.*, 2019, **1**, 1045-1053.
40. C. Demitri, R. Del Sole, F. Scalera, A. Sannino, G. Vasapollo, A. Maffezzoli, L. Ambrosio and L. Nicolais, *J. Appl. Polym. Sci.*, 2008, **110**, 2453-2460.
41. J. Zhou, C. Chang, R. Zhang and L. Zhang, *Macromol. Biosci.*, 2007, **7**, 804-809.
42. D. Klemm, D. Schumann, U. Udhardt and S. Marsch, *Prog. Polym. Sci.*, 2001, **26**, 1561-1603.
43. A. Bodin, S. Concaro, M. Brittberg and P. Gatenholm, *J. Tissue Eng. Regener. Med.*, 2007, **1**, 406-408.
44. C. Chang and L. Zhang, *Carbohydr. Polym.*, 2011, **84**, 40-53.
45. M. He, H. Chen, X. Zhang, C. Wang, C. Xu, Y. Xue, J. Wang, P. Zhou and Q. Zhao, *Cellulose*, 2018, **25**, 1987-1996.
46. C. Chang, K. Han and L. Zhang, *Polym. Adv. Technol.*, 2011, **22**, 1329-1334.
47. C. Cui, C. Shao, L. Meng and J. Yang, *ACS Appl. Mater. Interfaces*, 2019, **11**, 39228-39237.
48. C. Shao, H. Chang, M. Wang, F. Xu and J. Yang, *ACS Appl. Mater. Interfaces*, 2017, **9**, 28305-28318.

# Chapter 1.

# Cellulose Luminescent Hydrogels Loaded with Stable Carbon Dots for Duplicable Information Encryption and Anti-counterfeiting

## 1.1 Introduction

The rapid development of information techniques greatly improves the convenience of human life, but leads to endless counterfeit products and information leakage.[1-3] This trend is contrary to the principles of sustainable development and has resulted in huge waste of the earth's resources. It is an inevitable topic that development of information storage materials with protection and encryption ability.[4] Although considerable research on information encryption materials, including fluorescent ink,[5, 6] self-erasing materials,[7, 8] and luminescent patterns[9] has been conducted in recent years, flexible smart gels based on discoloration behavior have been scarce. Sustainable and cost-effective hydrogels exhibit unique fluorescent properties and biocompatibility, which are generally exploited in the fields of pharmaceutical industries, imaging, biosensing, therapeutics, and so on. [3, 10-12]

It is clear that smart hydrogels are promising candidates for information storage due to their unique responsiveness to specific stimuli, which can load and decrypt hidden information under specific conditions.[13, 14] Chen *et al.*[15] designed a multi-responsive nanofiber-reinforced poly (*N*-isopropyl acrylamide) hydrogel inspired by a paper structure. This hydrogel exhibited solvent-induced high-resolution reversible information recording, self-encryption, and multiple-decryption functions. Lou *et al.*[16] prepared a polymer hydrogel based on lower critical solution temperature (LCST) and upper critical solution temperature (UCST), which can

perform “double locking” from the time and temperature dimensions and can be used for information camouflage and multilevel encryption. Liu *et al.*[17] innovatively combined the transparency of ion-conducting hydrogels with anti-swelling and macroscopic changes induced by hydrophobic polymer chains in organic hydrogels and prepared ionic organic hydrogels with excellent mechanical properties and unique behaviors (information recognition and encryption) in various environments. These hydrogels can be used as dynamic information storage devices for recording and encrypting information. Owing to attracting great attention, they have been proven to be eminent candidates for flexible anti-counterfeiting in high-level information security.

However, the expensive price, lack of eco-friendliness and incompatibility with hydrogel matrix of fluorescent monomers limit the further development of fluorescent smart hydrogels in this field.[18, 19] Recently, carbon dots (CDs) has been widely known as a promising luminescent nanomaterial with abundant low-cost sources, facile synthetic methods, excellent biocompatibility, high chemical stability, significant water solubility, low cytotoxicity, and excellent optoelectronic properties, attracting great attention in many fields including biomedicine, catalysis, optoelectronic devices and especially anticounterfeiting.[20-22] Many scholars demonstrated that integrating CDs into desirable polymer matrix is a cost-effective and environment friendly method to develop flexible materials for information encryption. For instance, Xiong *et al*. reported a flexible right-hand chiral fluorescent film with potential applications in sensing and anti-counterfeiting.[23] The self-assembled film by CDs-modified cellulose nanocrystals could generate specific fluorescent patterns by two-dimensional chemical printing technology. Wu *et al.* fabricated double-layer fluorescent hydrogel-organogel with adjustable amphiphilic imidazolium-type ionic liquid (IL)-based CDs, and the gel exhibited a light and force dual-stimuli response and could provide more secure information encryption than traditional single-layer encryption materials.[24] Nevertheless, few reports

concerned the heterogeneous distribution and even leaching behavior of CDs inside the polymer network due to their weak supramolecular interactions.[25]

The hydrophilic polymer chain in hydrogel is beneficial for the homogeneous dispersion of high-water soluble CDs. Further, the abundant functional groups, such as carboxyl, amino, hydroxyl, *etc*. on CDs surface provide the possibility of chemical fixation inside the hydrogel matrix. On the one hand, three-dimensional (3D) networks of hydrogel can provide the CDs with chemical stability, also contribute to inhibit the aggregation-caused-quenching (ACQ) effect of high concentration CDs.[26] On the other hand, the introduced CDs improves the mechanical properties of the hydrogel as well as confers the material additional functionality such as information storage and anti-counterfeiting.[27]

Based on the concepts of a green economy and sustainable development, the utilization of natural renewable resources as CDs carriers is a reasonable choice.[11, 28] Cellulose, a plant-based renewable fiber, has been chosen as an environmentally friendly hydrogel material because of its distinguishable mechanical properties, multi-hydroxy functionality, biodegradability, and abundant availability.[29, 30] The presence of massive functional groups and charges in cellulose backbone provides the opportunity of modification reactions. Lv *et al.*[31] used the physical electrostatic interaction between carboxymethyl cellulose and CDs to uniformly disperse CDs into a hydrogel matrix to obtain fluorescent hydrogels with excellent mechanical properties that can be used to store information and anti-counterfeiting. Hence, it not only provides a backbone for the assembly of 3D structure, but also serve as a natural holder to introduce CDs uniformly into the hydrogel matrix.

In this research, the author reports a facile fabrication of chemistry bonding fluorescent nanocomposite hydrogel based on green-synthesized CDs and fibrillated citric acid-modified cellulose (F-CAC). Through the stupendous chemical interaction between the CDs and F-CAC, CDs/F-CAC was incorporated into a biocompatible, flexible hydrogel matrix of acrylamide and

the hydroxyethyl methyl acrylate copolymer, P(AAm-*co*-HEMA). Thus, the CDs/F-CAC chains enabled the composite gel to overcome the shortcomings of nanoparticle leaching, avoiding the migration of CDs outside the gel when swollen. The CDs/F-CAC not only significantly improved the mechanical properties and anti-fatigue performance of P(AAm-*co*-HEMA), but also endowed the hydrogels with excellent fluorescence properties. Satisfyingly, the fluorescence of the CDs/F-CAC hydrogels was quenched by $Fe^{3+}$ ions and recovered in an ascorbic acid/EDTA-2Na mixture solution. Thus, the as-prepared display platform of fluorescent hydrogel *via* ionoprinting technique could be used repeatedly. This novel strategy broadens the applications of natural resources hydrogels as storage modules for information encryption and anti-counterfeiting.

## 1.2 Experimental Section

### Materials

Citric acid, urea, acrylamide (AAm), ascorbic acid, ammonium persulfate (APS) and iron chloride hexahydrate ($FeCl_3 \cdot 6H_2O$) were purchased from Wako Pure Chemical Industries, Ltd. (Wako, Osaka, Japan). Cellulose (microcrystalline powder, particle size of 51 μm, pH of 5-7 (11 wt %), bulk density of 0.6 g/mL (25°C)) was purchased from Sigma Co., Ltd. (Aldrich, USA). 1-(3-dimethylaminopropyl)-3-ethylcarbodiimide hydrochloride (EDC) and *N*-hydroxysuccinimide (NHS), were obtained from Tokyo Chemical Industry Co., Ltd. (TCI, Tokyo, Japan). Methanol, acetone, 0.1mol/L acetate buffer solution (pH=5), 2-hydroxyethyl methacrylate (HEMA) and *N*, *N*′-methylenebisacrylamide (MBAA) were purchased from Nacalai Tesque, Inc. (Kyoto, Japan). Ethylenediaminetetraacetic acid disodium salt was purchased from Dojindo Laboratories Co., Ltd. (Kumamoto, Japan). All chemicals were used without further purification. Deionized (DI) water purified using a Milli-Q system (Millipore Inc., Milford, MA), was used in all experiments.

**Synthesis of fluorescent CDs**

Luminescent CDs were synthesized via a one-step microwave pyrolysis.[32] Briefly, citric acid (3 g) and urea (3 g) were dissolved in DI water (10 mL), and the clarified solution was obtained under ultrasonic vibration. Next, the transparent solution was placed in a domestic microwave oven (Panasonic, Japan) and heated using a middle-high fire (600 W) for approximately 7 min. The obtained brown-black solid was dissolved in an appropriate amount of water and centrifuged (10000 rpm, 20 min) to remove large insoluble solid particles. Furthermore, the CDs solution was dialyzed using a dialysis membrane (MWCO = 1000) in DI water for 48 h to remove unreacted starting materials and small-molecular-weight reaction products. Finally, the CDs were obtained as a dark brown solid after rotary evaporation and dried under vacuum.

**Modification and fibrillation of cellulose**

Citric acid-modified cellulose (CAC) was prepared using a method similar to that reported in our previous work.[33] Briefly, microcrystalline cellulose powder (30 g) was dispersed in DI water (300 mL), and citric acid (90 g) was added to the cellulose solution under strong stirring. After the citric acid was completely dissolved, the mixture was transferred into an oven at 130 °C for 15 h, and the esterification reaction occurred with the evaporation of water under high temperatures. After the reaction, the modified cellulose was processed with filtration and washed with DI water to remove residual citric acid until the filtrate was neutral. The product was washed with methanol and acetone. CAC was obtained after 1 day of vacuum drying. To obtain a fibrillated and homogeneous suspension of CAC nanofibers, an aqueous suspension of CAC (1.5 wt %) was prepared and then pulverized using a Star Burst Mini wet pulverizing and dispersing device (Sugino Machine Co., Ltd., Japan). Under an ejection pressure of 245 MPa, the CAC mechanically disintegrated into cellulose nanofibers 30 times, and the prepared aqueous suspension was named F-CAC (1.5 wt %).

The carboxylic-group content of the F-CAC was measured by conductometric titration using a conductivity meter (LAQUA F-74; HORIBA Ltd., Kyoto, Japan). The average carboxyl content was 0.48 mmol/g, calculated according to a previously reported test method.[34]

**Preparation of citric acid-modified cellulose nanocomposite decorated with carbon dots (CDs/F-CAC)**

The F-CAC was further decorated with CDs based on common EDC/NHS coupling chemistry, according to previous reports.[28] First, the F-CAC aqueous solution (40 mL, 1.5 wt %) was added to 20 mL acetate buffer solution (0.1 M, pH = 5) with ultrasonic vibration for 30 min. Next, EDC (119 mg) was added, and the admixture was vigorously stirred for 15 min. Subsequently, NHS (460 mg) was added, and the admixture was continuously stirred for 15 min. Then, 100 mg of the CDs was added to the reaction mixture. The reaction proceeded overnight under magnetic stirring at room temperature (RT) in the dark. The resulting suspension was dialyzed (MWCO = 1000) in DI water for 48 h. After freeze-drying, a light-brown powder was obtained and named CDs/F-CAC.

**Preparation of fluorescent hydrogels**

Fluorescent hydrogels were prepared via one-pot free-radical polymerization of the precursor aqueous solution within HEMA, AAm, CDs/F-CAC, and MBAA, using APS as the initiator. The procedure was as follows: initially, a certain amount of CDs/F-CAC was dissolved in 5 mL DI water and sonicated it until uniformly dispersed. Subsequently, 2 g HEMA monomer, 1 g AAm monomer, 30 mg APS (1.0 wt % against HEMA and AAm), and 15 mg MBAA (0.5 wt % against HEMA and AAm) were added to the solution, sonicated, and stirred until a homogeneous solution was obtained. After degassing by bubbling with nitrogen for 10 min, the mixture was injected into a self-made mold consisting of two glass plates and one silica plate (2 mm). In situ free-radical polymerization of the hydrogel was performed in a water bath at

60 °C for 6 h. The hydrogels were named CDs/F-CAC-0.1, CDs/F-CAC-0.5, CDs/F-CAC-1.0, and CDs/F-CAC-1.5 with the CDs/F-CAC content varying from 0.1 wt % to 0.5 wt %, 1.0 wt % and 1.5 wt %, respectively (based on the total weight of HEMA and AAm). At the same time, the same method was used to prepare hydrogel without CDs/F-CAC and named CDs/F-CAC-0. The hydrogels containing only CDs, which have the same quality as the CDs with the CDs/F-CAC-1.0 hydrogel according to the loading content of CDs, were synthesized via the same procedure and named CDs-1.0.

**Information loading and erasing**

Information was loaded into hydrogels using ionoprinting, as reported by Le *et al.*[35] Briefly, the filter papers were soaked in $FeCl_3$ solution (125 mM) for 2 h, then removed and dried in an oven (60 °C). After drying, the filter papers containing $Fe^{3+}$ were cut into the desired shapes and then placed on the surface of the fluorescent hydrogels for 2 min. After peeling off the filter paper, the desired information loading was obtained and visualized under specific UV light. The information-loaded hydrogels were soaked in a mixed solution of ascorbic acid/EDTA-2Na (0.1 M) for 2 h, and the information was erased.

**Characterization**

Attenuated total reflection Fourier transform infrared (ATR-FTIR) spectroscopy (Thermo Scientific Nicolet iS5, USA), UV-vis absorption spectroscopy (J-820 AC, JASCO Corporation, Japan), X-ray diffraction (XRD, Rigaku Corporation, Tokyo, Japan), and X-ray photoelectron spectroscopy (XPS, JEOL JPS-9010MC) were used to confirm the chemical compositions and structures of the CDs, CAC, and CDs/F-CAC. The light transmittance measurement of the hydrogels was conducted in quartz cells through UV–vis spectrophotometer. The heights and morphologies of the CDs and F-CAC were characterized using Atomic Force Microscope (AFM, SPI3800N/SPA-400, Seiko Instruments Inc., Tokyo, Japan). The microstructures and

morphologies of the cellulose, F-CAC, and hydrogels were observed using scanning electron microscopy (SEM, Hitachi SU-3500, Japan). The photoluminescence (PL) spectra of the CDs and hydrogels were recorded using a microplate reader (SH-9000Lab, Yamato Scientific Co., Ltd., Tokyo, Japan). The thermal stability of the CDs, CAC, and CDs/F-CAC was investigated using a thermogravimetric analyzer (TGA, Hitachi STA7200RV, Japan) by heating from 30 to 800 °C under nitrogen protection.

**Swelling measurements**

The swelling behavior of the as-prepared gels was measured in a large amount of DI water at room temperature until swelling equilibrium was reached. At certain times, the gels were removed from the DI and surface water and quickly weighed. The swelling ratio *SR* was calculated as, $SR = (W_s - W_d) \times 100\% / W_d$, where $W_s$ and $W_d$ are the weights of the swollen hydrogels and the corresponding dried hydrogels, respectively.

**Mechanical tests**

The samples for the compression and cyclic compression tests were prepared in cylindrical shapes with lengths of 8–10 mm, and a diameter of 13 mm. The stress at the respective compression strains on the hydrogels was characterized using an EZ Graph universal material testing machine (Shimadzu, Japan) equipped with a 500 N load and a speed of 3.0 mm/min at room temperature. The compressive modulus was determined from the slope of the nominal compression curve in the strain range of 10%–20%. The compressive toughness $U_{CT}$ was estimated from the area under the stress–strain curve, using the following **Equation 1.1**:

$$U_{CT} = \frac{\int_0^{0.7} F\, ds}{\pi R^2} \tag{1.1}$$

where $F$ is the compressive load and $s$ is the compressive displacement of the corresponding strain. For the self-recovery experiment, successive loading–unloading compression tests were performed 10 times under different strains (10, 30, and 50%) at a rate

of 0.5 mm/min and tested again with a resting time (1 min). The hysteresis energies were calculated from the loop area between the loading and unloading curves.

**Rheological properties**

Rheological tests were performed using a Haake Rheostress 6000 (Thermo Fisher Scientific, Waltham, MA, USA) instrument equipped with 20-mm-diameter parallel plates to analyze the gels at room temperature. The angular frequency was swept from 1 to 100 rad/s at a fixed strain of 0.1%.

## 1.3 Results and discussion

**Synthesis of materials**

The CDs were prepared by heating citric acid and urea in DI water via a one-step microwave method, as shown in **Figure 1-1a**. Microwave irradiation technology is an efficient option because of its advantages of in-situ, instantaneous heating, and large-scale synthesis of homogeneous CDs.[36] It is demonstrated that the resulting CDs could be homogeneously dispersed in DI water, producing a dark brown solution. The CDs exhibited significant dispersibility when a one-step microwave method was used.

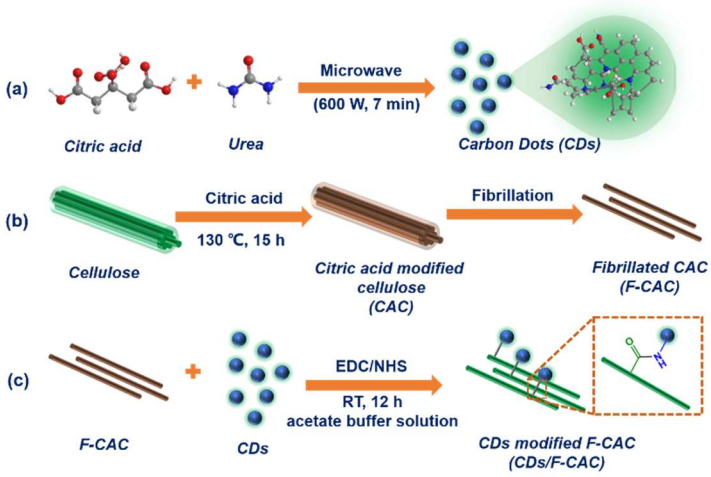


**Figure 1-1.** Schematic illustration of the preparation of (a) CDs, (b) F-CAC, and (c) CDs/F-CAC.

To enhance the functionality and hydrophilicity, citric-acid-modified cellulose was prepared to endow the surface with carboxylic acid groups, which can serve as reactive sites

for CDs, as shown in **Figure 1-1b**. The modification was achieved through esterification between the hydroxyl groups of cellulose and carboxyl groups of citric acid. Because the modification reaction was carried out in the solid state, it allowed the mass production of modified cellulose without using organic solvents. To prepare nanocellulose, a fibrillation method that uses aqueous counter collision (ACC) without any chemical modification was used to increase the surface area of CAC for the next reaction.[37] **Figure 1-1c** displays amino-carrying CDs grafted onto F-CAC using common EDC/NHS coupling chemistry.

**Micro-morphology of CDs**

In general, AFM was used to confirm the morphologies and heights of the prepared CDs, as shown in **Figure 1-2a**. The CDs were uniformly sized spheres with a height of approximately 2–3 nm. The surface morphologies of the cellulose and fibrillated cellulose were compared using SEM. It can be seen from **Figure 1-2b** that the cellulose is coarse and intertwined. Comparatively, after treatment with ACC for 30 passes, cellulose was crushed into nanoscale fragments, as shown in **Figure 1-2c**.

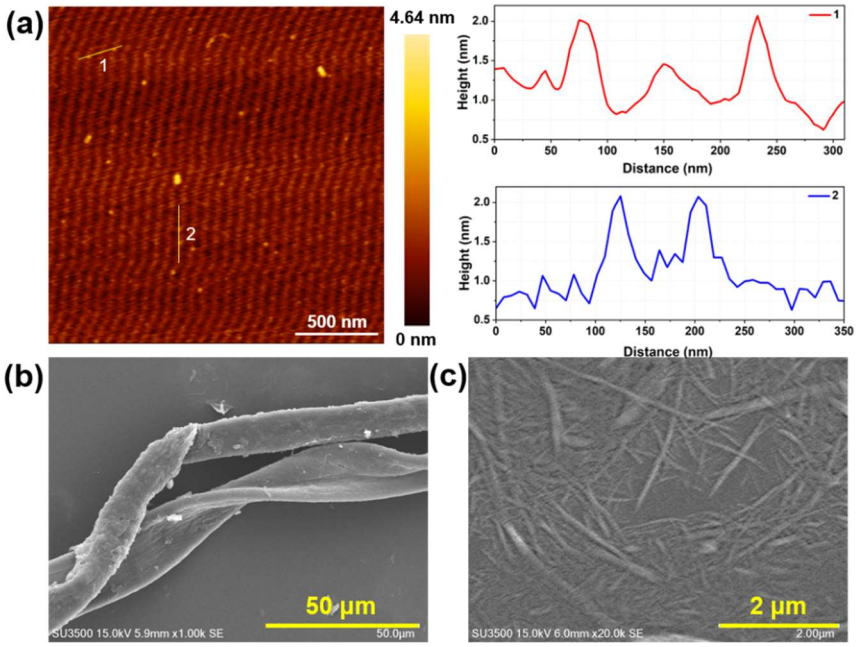


**Figure 1-2.** (a) AFM (on mica) image and topography of CDs. SEM image of (b) cellulose and (c) F-CAC.

**Characterization of materials**

FTIR spectroscopy was used to detect the occurrence of the reaction (**Figure 1-3a**).

Compared to the characteristic spectra of cellulose, esterification by citric acid was determined by the presence of new carboxylic acid and ester carbonyl peaks at approximately 1730 $cm^{-1}$. The CDs exhibited stretching vibrations of C–OH at 3204 $cm^{-1}$, C–H at 3057 $cm^{-1}$, and C–N or C–O–C at 1281 $cm^{-1}$. The peaks centered at 1584 and 1694 $cm^{-1}$ are attributed to the N–H and C=O bonds, respectively. The existence of these broad absorption bands demonstrates the presence of functional groups, such as carboxyl and amide, on the surface of CDs.[31] Compared to the spectrum of F-CAC, the characteristic bands at 1580 (corresponding to the $–NH_2$ stretching vibration of excess CDs) and 1704 $cm^{-1}$ (corresponding to the –CO–NH– stretching vibration) were observed in the spectrum of CDs/F-CAC. This verifies the occurrence of carboxyamine condensation between F-CAC and CDs.

The aqueous solutions of CDs and CDs/F-CAC emit green light with excitation occurring at $\lambda_{ex}$ = 365 nm (under UV lamp), indicating obvious fluorescence, as shown in the inset of **Figure 1-3b**. **In Figure 1-3b**, the UV-vis spectra of CDs and CDs/F-CAC show nearly the same characteristic absorption peaks, including distinct absorption shoulders at ≤250 nm, clear peaks at 340 nm, and shoulders located at 440 nm. Based on the literature, absorption bands at approximately 250 nm are attributed to a $\pi$–$\pi$* transition of the C=C and C=N bonds of the $sp^2$ C domain in polymetric carbon nitrides, and the peaks at 340 nm are assigned to the $n$–$\pi$* transition of the C═O and C=N bonds in g-$C_3N_4$, corresponding to a typical absorption pattern of carbon nitride (335 nm).[38] The extended absorption shoulders located at 440 nm may result from the complex ligand shell at the CDs surface and which is known as surface state transition.[39, 40]

In the fluorescence spectra, the CDs exhibited an emission intensity maximum at 510 nm when excited at 420 nm. Similar to previous reports,[36, 41, 42] the CDs showed an obvious dependence of the photoluminescence wavelength and intensity on the excitation wavelength (**Figure 1-3c**), which is a typical characteristic of fluorescent carbon materials and may be due

to the presence of core carbon, diverse surface states (hybridization between the core carbon and functional groups), and molecular states owing to the presence of phosphors.

The wide (002) peak at around 27° of the XRD diffraction pattern of the CDs demonstrates that carbonized citric acid and urea can produce the graphite structure, as shown in **Figure 1-3d.**[43] In **Figure 1-3e**, the XRD diffraction patterns of F-CAC and CDs/F-CAC demonstrate the unique diffraction regions of **cellulose I**. The main peaks at 14.9, 16.4, and 22.5 were attributed to the typical (1-10), (110), and (200) reflections of the **cellulose I** pattern, respectively.[44] Compared to that of F-CAC, the XRD pattern of CDs/F-CAC did not change significantly, implying that the typical structure of **cellulose I** was maintained even though CDs were attached to the surface of F-CAC via an acylation reaction.[45]

Thermogravimetric analysis was utilized to verify the thermal stability of the CDs, F-CAC, and CDs/F-CAC and to determine the loading content of the CDs. **Figure 1-3f** shows TGA curves of the test samples. The weight loss rate during the test can be calculated using the following **Equation 1.2**:

$$W = \frac{W_{initial} - W_{end}}{W_{initial}} \times 100\% \quad (1.2)$$

where $W_{initial}$ is the initial quality of the test, and $W_{end}$ is the final amount.

The initial small weight loss was caused by the evaporation of low-molecular-weight compounds or adsorbed water from the curves. At first, the CDs began to decompose with increasing temperature, which could be attributed to the decomposition caused by unsteady oxygenous groups on the loose surface of the CDs and CO, $CO_2$, and other oxygenated carbides that were simultaneously generated. This is why CDs/F-CAC decomposes earlier than F-CAC. It is clear that at 800 °C, the mass loss of the CDs/F-CAC composite was lower than that of F-CAC. This may be because the stable CDs did not participate in combustion; only the macromolecules were involved in combustion, indicating the successful loading of CDs on the

F-CAC. Moreover, the loading of CDs had little effect on the thermal degradation behavior of cellulose, which further confirms the successful synthesis of CDs/F-CAC nanocomposites.[46] Based on the weight loss rate calculations, the loading content of CDs was approximately 34%.

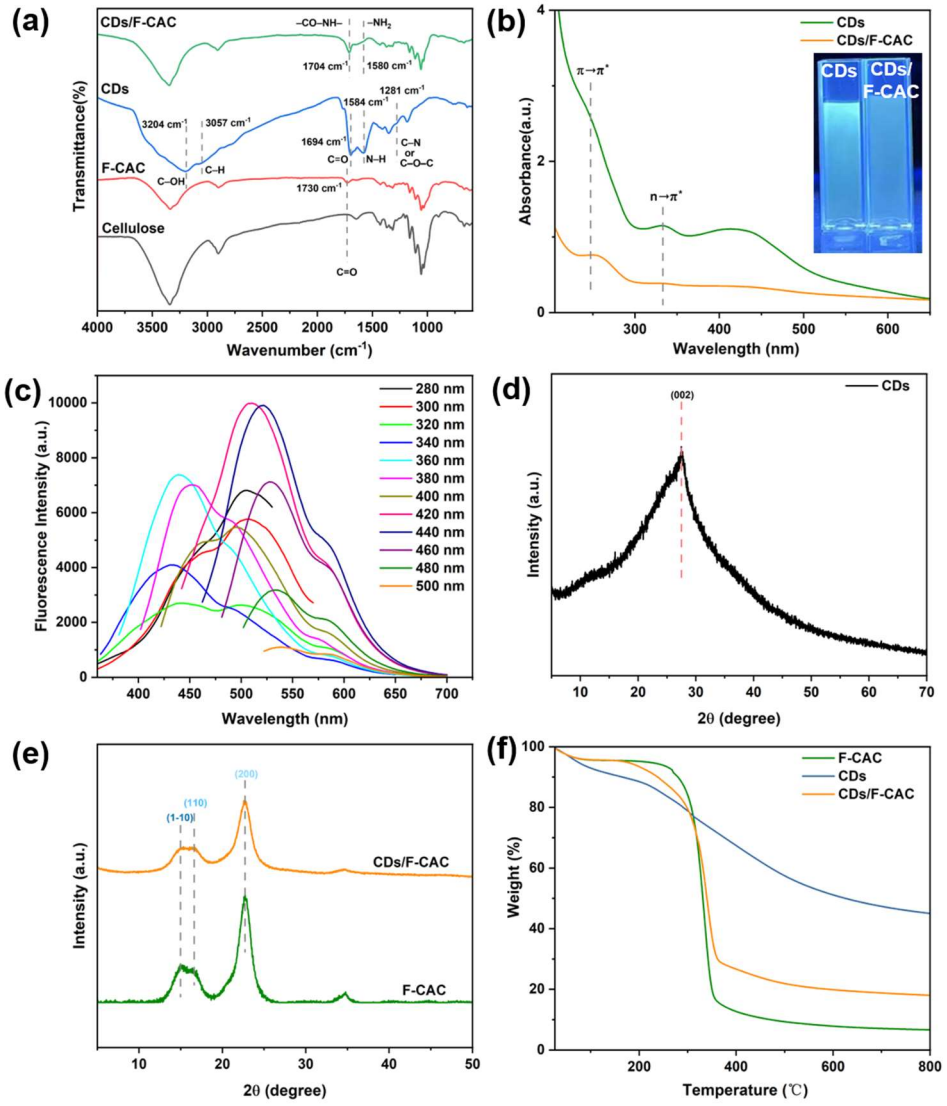


**Figure 1-3.** (a) ATR-FTIR spectra of cellulose, F-CAC, CDs, and CDs/F-CAC. (b) UV-vis absorption spectra of CDs and CDs/F-CAC. Insets show photographs of CDs and CDs/F-CAC solutions under 365 nm UV lamp. (c) Photoluminescence spectra of the CDs under different excitation wavelengths. XRD patterns of (d) N-CDs, (e) F-CAC, and CDs/F-CAC. (f) TGA thermogram of F-CAC, CDs, and CDs/F-CAC.

X-ray photoelectron spectroscopy (XPS) was used to analyze the surface chemical compositions, structures, and bonds of the prepared hybrid materials. The full XPS profiles of F-CAC, CDs, and CDs/F-CAC, as well as their corresponding elemental contents, are shown

in **Figure 1-4a** and **Table 1-1**. The C 1s, O 1s, and N 1s fine spectra of the samples were analyzed in detail (**Figures 1-4b–i**). The compositions of the elements and their corresponding contents were shown in **Figure 1-4a** and listed in **Table 1-1**. The XPS spectra show that F-CAC is composed of C and O elements with binding energies of 286.2 and 533.2 eV attributed to C 1s and O 1s, respectively. For the CDs and CDs/F-CAC, in addition to C and O, the full-scan XPS spectra presents distinct N 1s peaks at 399.3 eV. **Table 1-1** shows that the CDs present a higher N and C atomic ratios (11.759% and 59.795%, respectively) and lower O/C ratio (0.48) than those of F-CAC, indicating that a high fraction of N atoms were successfully doped into the CDs.[47] The N atomic ratio decreases to 6.76% after conjugating the CDs with F-CAC (to form CDs/F-CAC hybrids). Moreover, comparing F-CAC with CDs/F-CAC, the O/C ratio decreases from 0.73 to 0.66, which can be taken as a further indication of a successful coupling reaction. Furthermore, a detailed analysis of the C 1s, O 1s, and N 1s peaks of F-CAC, CDs, and CDs/F-CAC was performed. As expected, combined with the detailed XPS spectra of F-CAC and CDs (**Figures**

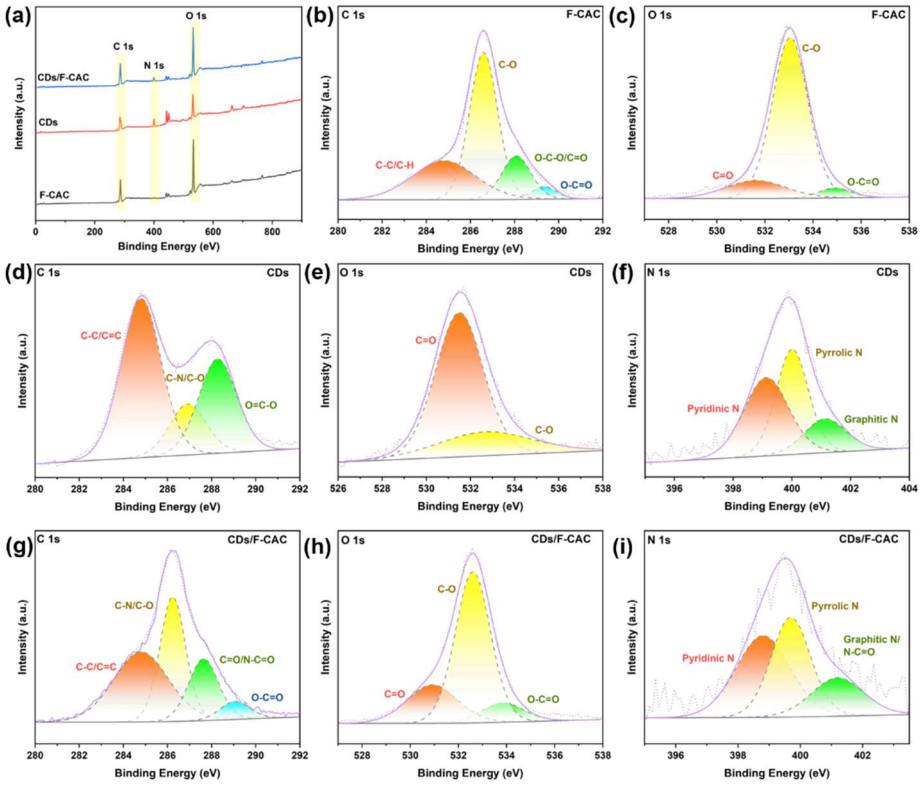


**Figure 1-4.** (a) XPS survey spectra of F-CAC, CDs, and CDs/F-CAC. (b–c) High-resolution XPS fitting results for C 1s and O 1s of F-CAC. (d–f) High-resolution XPS fitting results for the C 1s, O 1s, and N 1s spectra of CDs. (g-i) High-resolution XPS fitting results for the C 1s, O 1s, and N 1s spectra of CDs/F-CAC.

**1-4b–f**), the C 1s, N 1s, and O 1s spectra of CDs/F-CAC verify the occurrence of an acylation reaction.[45] The C 1s spectra (Figure 4g) suggest the presence of C–C/C=C (284.8 eV), C–N/C–O (286.2 eV), C=O/N–C=O (287.6 eV), and O–C=O (289.1 eV). The O 1s spectra (**Figure 1-4h**) are deconvoluted into three peaks at 530.9, 532.6, and 533.8 eV corresponding to C=O, C–O, and O–C=O, respectively. The N 1s spectra (**Figure 1-4i**) can be divided into three peaks at 398.8, 399.7, and 401.2 eV, which can be assigned to pyridinic N, pyrrolic N, and graphitic N/N–C=O, respectively. Therefore, it can be concluded that CDs/F-CAC is mainly composed of carbon atoms and oxygen- and nitrogen-containing functional groups.[48, 49]

**Table 1-1.** Surface chemical composition of F-CAC, CDs and CDs/F-CAC.

| | **Surface composition (%)** | | | |
|---|---|---|---|---|
| | **O 1s** | **C 1s** | **N 1s** | **O/C** |
| **F-CAC** | 42.033 | 57.967 | — | 0.73 |
| **CDs** | 28.646 | 59.595 | 11.759 | 0.48 |
| **CDs/F-CAC** | 37.897 | 57.104 | 4.999 | 0.66 |

**Synthesis and morphologies of CDs/F-CAC hydrogels**

The preparation of the hydrogels with fluorescent properties is illustrated in **Figure 1-5a**. F-CAC provided the natural skeleton that connected with the fluorescent CDs based on a carboxyamine condensation reaction, and hydrogels were then prepared through the one-pot free radical copolymerization method. Rigid F-CAC enhances the mechanical properties of the hydrogels, whereas CDs impart fluorescence properties to them. The as-prepared hydrogels with a thickness of 2 mm (**Figure 1-5b**) displayed increasing bright green fluorescence under UV light as the CDs/F-CAC content increased. The cross-sectional morphologies of the freeze-dried hydrogels with different CDs/F-CAC contents are shown in **Figures 1-5c–e**. Compared

to the hydrogel without the addition of CDs/F-CAC (**Figure 1-5c**), the CDs/F-CAC-0.1 (**Figure 1-5d**) and CDs/F-CAC-0.5 (**Figure 1-5e**) hydrogel cross-sections have more regular pore channels and homogeneous structures with tighter networks, which may lead to outstanding mechanical properties of the CDs/F-CAC hydrogels. Interestingly, numerous filamentous structures were observed in the CDs/F-CAC hydrogels, which contributed to denser porous structures. Therefore, it can be assumed from the SEM results that massive micropores in the hydrogel network prevent the propagation of cracks, and the homogeneous pore size enables the even distribution of stress to resist force centralization.[50, 51]

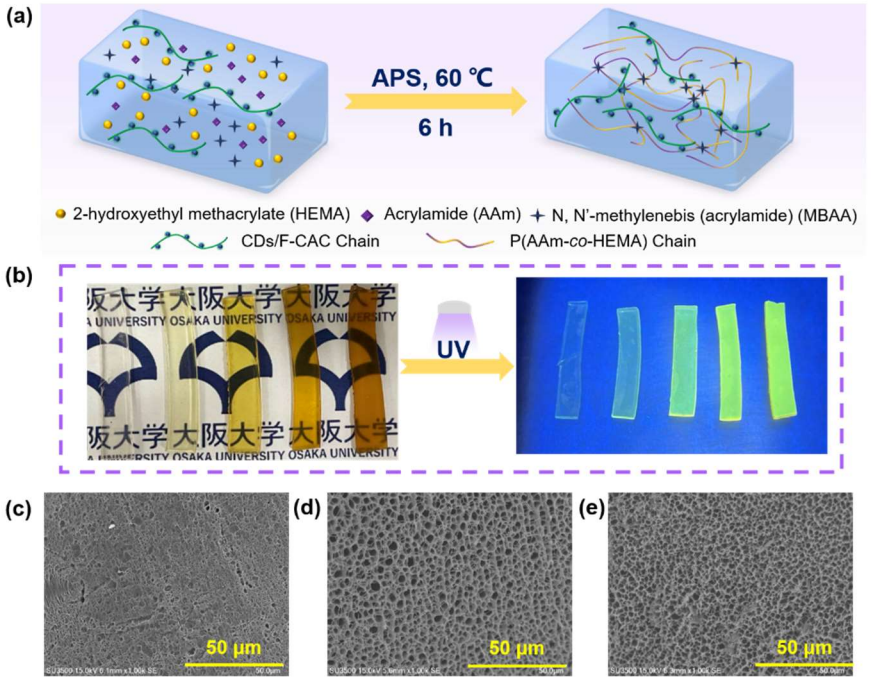


**Figure 1-5.** (a) Schematic illustration of the synthetic process of CDs/F-CAC hydrogels. (b) Appearance of CDs/F-CAC hydrogels with different concentrations under visible and UV light (from left to right: CDs/F-CAC-0, CDs/F-CAC-0.1, CDs/F-CAC-0.5, CDs/F-CAC-1.0, and CDs/F-CAC-1.5). Cross-sectional SEM images of the freeze-dried CDs/F-CAC hydrogels: (c) CDs/F-CAC-0, (d) CDs/F-CAC-0.1, and (e) CDs/F-CAC-0.5.

**Mechanical properties and rheological behavior**

The mechanical properties of the hydrogels were evaluated using uniaxial compression tests. As shown in **Figure 1-6a**, the hydrogels do not exhibit remarkable fractures upon compression tests at up to 70% strain according to the nominal compressive strain–stress curves; they quickly recover their original state after stress unloading during the compression test, indicating that the gels have extraordinary anti-fatigue properties (**Figure 1-6d**). The results

demonstrate that incorporating CDs/F-CAC significantly improves the compressibility of the P(AAm-*co*-HEMA) hydrogels, and with an increase in the CDs/F-CAC concentration, the compressive performance of the hydrogels gradually improves.

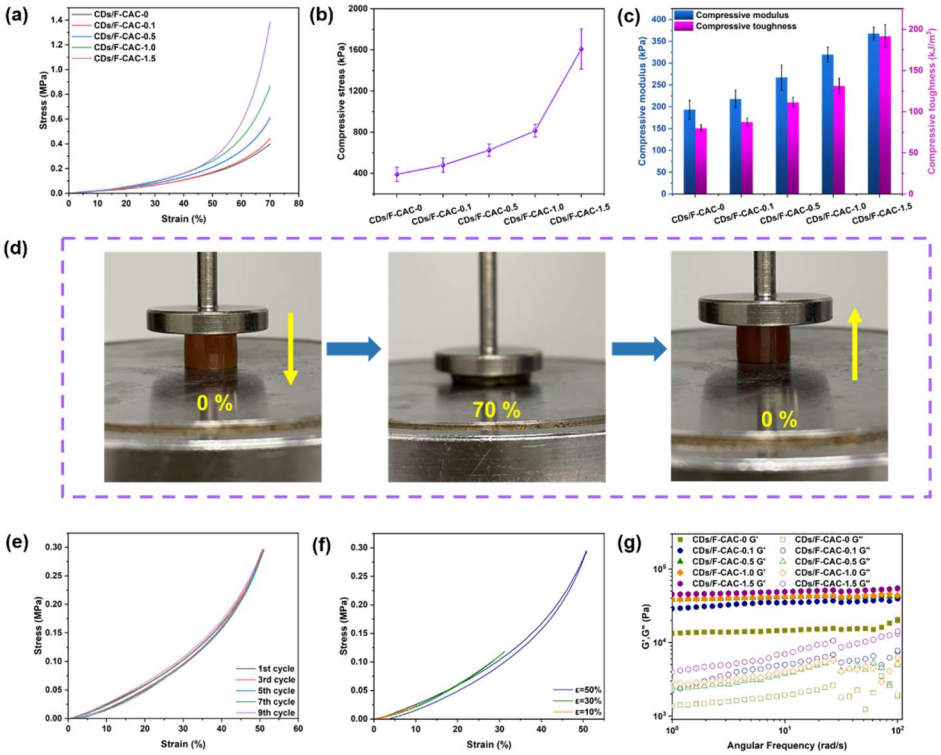


**Figure 1-6.** (a) Compressive curves of hydrogels with different CDs/F-CAC contents. (b) Compressive stress of hydrogels. (c) Compressive modulus and toughness of hydrogels. (d) Images of the compression and release processes of CDs/F-CAC-1.5 under 70% deformation. (e) Stress–strain curves of the CDs/F-CAC-1.5 hydrogel under cyclic compression with a peak strain of 50% without resting time. (f) Cyclic compressive loading–unloading curves under different strains (10%, 30%, and 50%). (g) Dynamic oscillatory frequency sweeps of hydrogels conducted at 25 °C.

Specifically, as shown in **Figures 1-6b–c**, the compressive performance of the CDs/F-CAC-0 hydrogels is the worst at 70% compressive strain, with stress, compressive modulus, and compressive toughness values of 389.87 kPa, 193.33 kPa, and 79.85 kJ/m$^3$, respectively. The CDs/F-CAC-1.5 hydrogels exhibited the highest strength and toughness; the stress, compressive modulus, and compressive toughness increased to 1607.30 kPa, 368.33 kPa, and 191.54 kJ/m$^3$, respectively. Cyclic compressive loading–unloading tests at 50% strain without any interruption were used to further investigate the fatigue resistance, resilience, and self-recovery capabilities of the CDs/F-CAC-1.5 hydrogels. From **Figure 1-6e**, the hydrogel can

completely recover from 10 consecutive compression cycles and exhibit overlapping hysteresis loops, thus proving that nanocomposite hydrogels have excellent self-recovery and anti-fatigue properties.[52] This stabilized hysteresis energy upon cyclic loading confirms the excellent fatigue resistance of the gels.[53] Furthermore, consecutive loading–unloading tests with gradually increasing compressive strains from 10% to 30% and 50% were performed on the same hydrogel. As shown in **Figure 1-6f**, with the increased strain, the hysteresis loop and hysteresis energy increases sharply, which is due to the rupture of noncovalent interactions between CDs/F-CAC and the polymer matrix to dissipate more energy.[50, 54] The excellent mechanical properties of CDs/F-CAC hydrogels can cope with various high degrees of deformation and continuous deformation with good fatigue resistance, which is beneficial for gels utilized as flexible materials to withstand repeatable deformation.[50] To illustrate the effect of CDs/F-CAC nanomaterials on the dynamic mechanical properties of P(AAm-*co*-HEMA) hydrogels, the viscoelastic properties of these hydrogels were investigated via the oscillatory rheological test. **Figure 1-6g** shows the tendencies of the storage ($G'$) and loss ($G''$) moduli at various frequencies under a constant low strain (0.1%). All hydrogels exhibit elastic-solid-like behavior over the entire frequency sweeping range because $G'$ is invariably larger than $G''$.[31] Moreover, both $G'$ and $G''$ increase with increasing CDs/F-CAC content and slightly increase with increasing oscillation frequency. The results indicate that the addition of CDs/F-CAC effectively improves the mechanical strength of hydrogels, further supporting the mechanical test results.[55, 56]

**Fluorescence properties of CDs/F-CAC hydrogels**

To verify the immobilization effect of F-CAC on the CDs in the hydrogel matrix, a soaking experiment was designed and performed; it compared the CDs/F-CAC-1.0 hydrogels with CDs-1.0 hydrogels containing the same CDs mass, which was calculated based on the previous loading rate. The CDs/F-CAC-1.0 and CDs-1.0 hydrogels with the same thickness, shape, and

quality were immersed in DI water of the same quality. Subsequently, the same quality of the hydrogel leaching solution was tested using UV-vis and fluorescence spectroscopy within a certain interval. As shown in

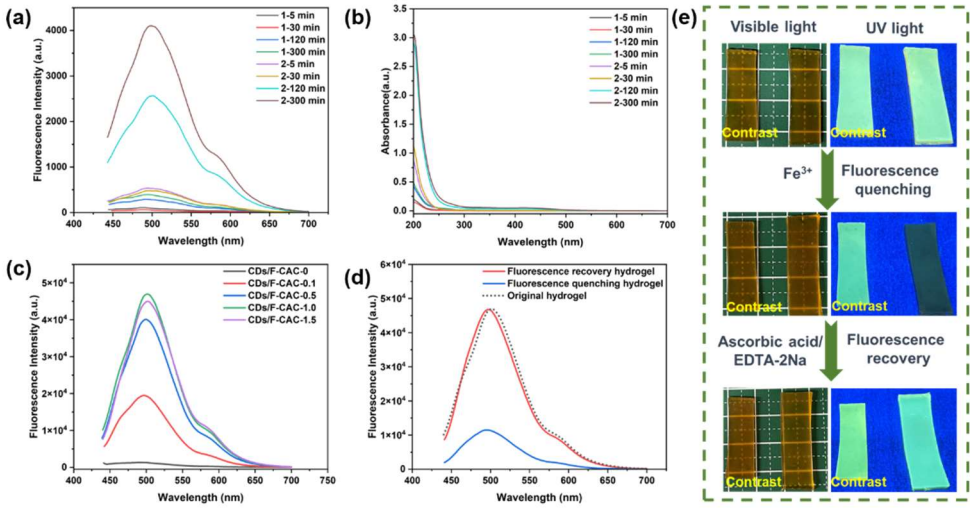


**Figure 1-7.** Characterizations of the hydrogel soaking solutions (1 represents CDs/F-CAC-1.0 hydrogel, and 2 represents CDs-1.0 hydrogel). (a) Fluorescence spectra excited at 420 nm. (b) UV-vis spectra. Fluorescent properties of hydrogels. (c) Fluorescence spectra of hydrogels with different concentrations of CDs/F-CAC excited at 420 nm. (d) Fluorescence spectra of fluorescence-quenched CDs/F-CAC-1.0 after soaking in a 125 mM $FeCl_3$ solution for 2 h and the fluorescence-recovery CDs/F-CAC-1.0 after soaking in a 0.1 M ascorbic acid/EDTA-2Na mixture (molar ratio 1:1) for 2 h, excited at 420 nm. (e) Images of fluorescence-quenched CDs/F-CAC-1.0 after soaking in a 125 mM $FeCl_3$ solution for 2 h and the fluorescence-recovery CDs/F-CAC-1.0 hydrogel after soaking in a 0.1 M ascorbic acid/EDTA-2Na mixture for 2 h under visible and UV light.

**Figures 1-7a-b**, CDs-1.0 hydrogels without F-CAC are more likely to lose CDs, and the fluorescence intensity reflecting the concentration of 2 h soaking solution increases with an increase in soaking time. Even after the hydrogel reaches the swelling equilibrium state after 20 h, CDs are still leaching from CDs-1.0 hydrogels. However, the fluorescence intensity of the hydrogel swollen solution (10 d) involved in chemical immobilization reaction was not significantly enhanced, which further confirmed that the addition of F-CAC can not only improve the mechanical properties of hydrogels, but also immobilize and stabilize CDs in the matrix of hydrogels effectively.

The fluorescence properties of CDs/F-CAC hydrogels were further investigated and are

shown in **Figure 1-7c**. Pure P(AAm-*co*-HEMA) hydrogels, which were CDs/F-CAC-0 hydrogels, exhibit no fluorescence, and the fluorescence intensity gradually increased as the CDs/F-CAC content changes from 0.1 to 1.0 wt %. However, compared with CDs/F-CAC-1.0, the fluorescence intensity of the CDs/F-CAC-1.5 hydrogel did not increase and slightly decreases. This may be attributed to the inhomogeneous dispersion of the CDs/F-CAC in the hydrogel matrix resulting from its excessive content, leading to fluorescence quenching. To verify this speculation, the fluorescence phenomenon of CDs/F-CAC dispersion solution with 0, 0.1, 0.5, 1, 1.5 wt % was tested (**Figure 1-8**). The fluorescence intensity in solution declined from 1.0 wt %, yet the hydrogel exhibited similar fluorescence variation from 1.5 wt %. In view of the similar trends, the concentration of CDs had a significant impact on fluorescence intensity, consistent with the aggregation-caused quenching (ACQ) effect.[26, 57] The differences between hydrogels and solutions lie in that the ACQ effect can be suppressed via CDs dispersion into polymer crosslinked network (solid matrix).[58] According to a previous report,[59] the molecular fluorophore of green fluorescing CDs based on citric acid and urea was 4-hydroxy-1*H*-pyrrolo[3,4-*c*]pyridine-1,3,6(2*H*,5*H*)-trione. Therefore, $Fe^{3+}$ ion could interact with the aromatic hydroxyl groups and further coordinate with the amino groups,[60] causing the nonradiative electron–hole annihilation. The photoluminescence quenching can be ascribed to the transfer of electrons from the excited state to the half-filled 3d orbitals in $Fe^{3+}$.[61, 62] Therefore, CDs-based materials can be applied to information storage, fluorescent probes, and intelligent

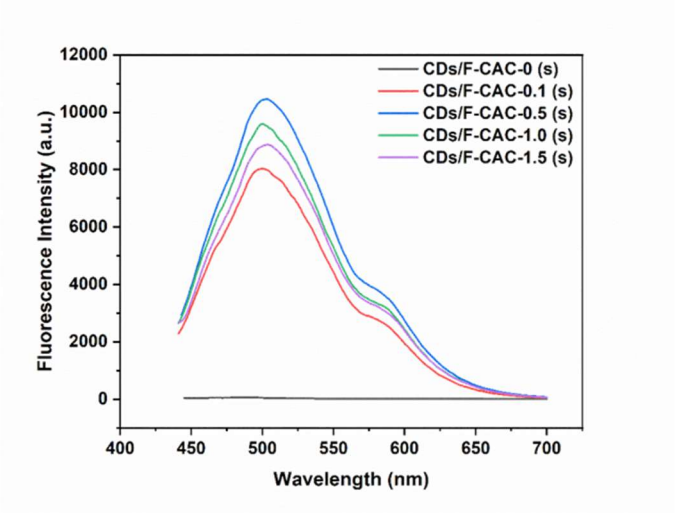


**Figure 1-8.** Fluorescence spectra of the solutions with different concentrations of CDs/F-CAC excited at 420 nm.

sensing.[63] The author examined the fluorescence quenching effect of $Fe^{3+}$ on the as-prepared CDs/F-CAC luminescent hydrogels and the fluorescence recovery effect of the ascorbic acid/EDTA-2Na mixture (molar ratio 1:1) on the fluorescence-quenched hydrogels. Considering the swelling of hydrogel, the CDs/F-CAC-1.0 hydrogel was soaked in a 125 mM $FeCl_3$ solution for 2 h, and the fluorescence intensity was lower than the original hydrogel as shown in **Figure 1-7d**. Accordingly, when the hydrogel quenched with $Fe^{3+}$ was immersed in a 0.1 M ascorbic acid/EDTA-2Na mixed solution for 2 h, the fluorescence intensity restored to near its original value (dots line, **Figure 1-7d**). This is because ascorbic acid and EDTA-2Na have better binding capabilities with $Fe^{3+}$, separating it from the hydrogel system.[64] In **Figure 1-7e**, these processes and changes are recorded by optical images of the CDs/F-CAC-1.0 hydrogel strips under visible and ultraviolet light and compared with the original strips.

**Fluorescence-quenching-based repeatable information loading and anti-counterfeiting**

It was verified that the fluorescence of the CDs/F-CAC hydrogels could be quenched by $Fe^{3+}$, and this fluorescence quenching could be eliminated using ascorbic acid/EDTA-2Na, as discussed previously. This encouraged us to explore fluorescence-quenching-based information loading and anti-counterfeiting. As shown in **Figure 1-9a**, filter papers with special shapes containing $Fe^{3+}$ are placed on the surface of the CDs/F-CAC hydrogels for 2 min. In the process of ionoprinting, $Fe^{3+}$ ions spontaneously diffused from the filter papers to the hydrophilic hydrogels, the fluorescence of the contact surface was quenched, and desirable patterns were remained on the surface of the CDs/F-CAC hydrogels.[35] Based on this principle, complex pattern combined with animal symbol and text was attempted to be written into the gel. Specially, information loading and erasing experiments were conducted applying the CDs/F-CAC-1.0 and CDs/F-CAC-1.5 hydrogels with near-fluorescence intensity in **Figure 1-9b**. Particular patterns could be easily transferred to the surface of fluorescent hydrogels, and these

printed patterns could only be observed under UV light, which can achieve the purpose of information loading and prevent information leakage.[65] Notably, the abovementioned loading information could be wiped by simply immersing the quenched hydrogels in an ascorbic acid/EDTA-2Na mixed solution, during which ascorbic acid and EDTA-2Na would bind to $Fe^{3+}$ ions, restoring the quenched fluorescence. Correspondingly, the new patterns could be imprinted and erased circularly onto the hydrogel after treatment with both $FeCl_3$ and ascorbic acid/EDTA-2Na solution. It is worth noting that the pattern is gradually difficult to be erased due to the chemical product accumulation, leading to a pattern residue caused by decreasing color-changing capacity. Moreover, compared with the CDs/F-CAC-1.0 hydrogels, the information loaded on the CDs/F-CAC-1.5 hydrogels were not easily erased without leaving traces. This may be due to the addition of excess CDs/F-CAC, which is consistent with the fluorescence properties.

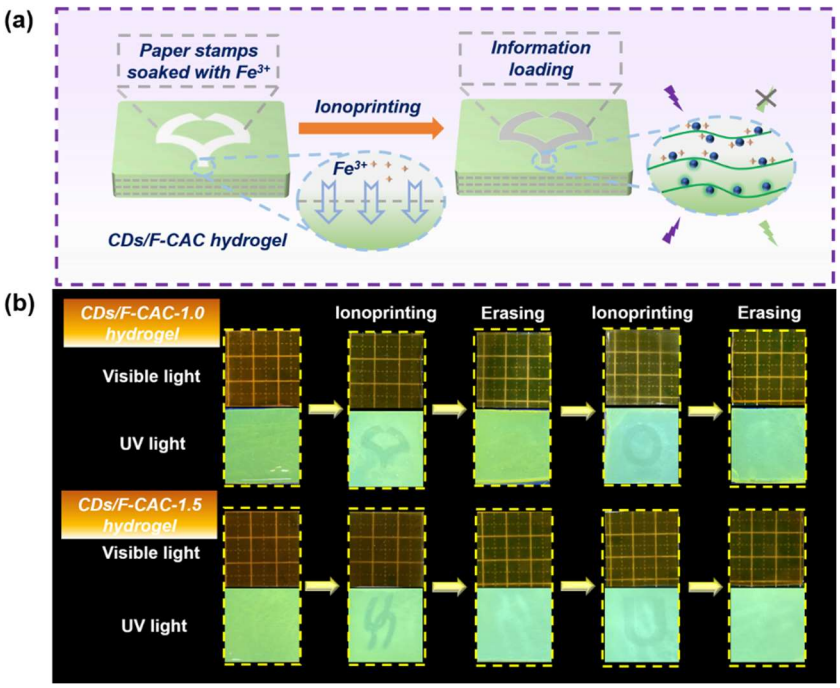


**Figure 1-9.** (a) Schematic illustration of the ionoprinting process. (b) Photos of a repeatable cycle between the ionoprinting and erasing processes of CDs/F-CAC-1.0 and CDs/F-CAC-1.5 hydrogels under visible and UV light.

## 1.4 Conclusion

In summary, a novel photoluminescent cellulose-based CDs/F-CAC nanomaterial functionalized with non-toxic carbon dots was prepared via an acylation reaction. Successful

preparation was confirmed by Fourier transform infrared spectroscopy, UV-vis absorption spectroscopy, X-ray photoelectron spectroscopy, and thermal analysis. The biomass originated CDs/F-CAC hydrogels with excellent fluorescence performance were further fabricated via a one-pot in-situ free-radical polymerization. On the one hand, the addition of CDs/F-CAC enhanced the mechanical properties of the hydrogels. With the increase in the CDs/F-CAC content from 0 to 1.5 wt %, at 70% compressive strain, the stress, compressive modulus, and compressive toughness increased from 389.87 kPa, 193.33 kPa and 79.85 kJ/$m^3$ to 1607.30 kPa, 368.33 kPa and 191.54 kJ/$m^3$, respectively. The CDs/F-CAC-1.5 hydrogels exhibited excellent recovery performance after the compressive loading–unloading cycling test. On the other hand, CDs/F-CAC-endowed hydrogels with exceptional fluorescent performance exhibited green fluorescence under UV light (365 nm) irradiation, and the fluorescence could be quenched or recovered via treatment with $Fe^{3+}$ ions or ascorbic acid/EDTA-2Na, respectively. Thus, the CDs/F-CAC hydrogels enabled repeatable information loading and erasing through the ionoprinting method based on the fluorescence properties. The stored information could only be observed under UV light; therefore, an anti-counterfeiting effect was achieved. The excellent properties of this fluorescent hydrogel make it a promising candidate for sustainable information storage devices.

## 1.5 References


1. K. Lou, Z. Hu, H. Zhang, Q. Li and X. Ji, *Adv. Funct. Mater.*, 2022, **32**, 2113274.
2. M. Li, H. Lu, X. Wang, Z. Wang, M. Pi, W. Cui and R. Ran, *Small*, 2022, **18**, 2205359.
3. X. Le, H. Shang, H. Yan, J. Zhang, W. Lu, M. Liu, L. Wang, G. Lu, Q. Xue and T. Chen, *Angew. Chem. Int. Ed.*, 2021, **60**, 3640-3646.
4. Q. Wang, Z. Qi, Q.-M. Wang, M. Chen, B. Lin and D.-H. Qu, *Adv. Funct. Mater.*, 2022, **32**, 2208865.
5. H. Wu, Y. Chen and Y. Liu, *Adv. Mater.*, 2017, **29**, 1605271.
6. P. Kumar, S. Singh and B. K. Gupta, *Nanoscale*, 2016, **8**, 14297-14340.
7. X. Le, H. Shang, S. Wu, J. Zhang, M. Liu, Y. Zheng and T. Chen, *Adv. Funct. Mater.*, 2021, **31**, 2108365.

8. S. Khlifi, N. Fournier Le Ray, S. Paofai, M. Amela-Cortes, H. Akdas-Kiliç, G. Taupier, S. Derien, S. Cordier, M. Achard and Y. Molard, *Mater. Today*, 2020, **35**, 34-41.
9. Y. Liu, K. Zhao, Y. Ren, S. Wan, C. Yang, J. Li, F. Wang, C. Chen, J. Su, D. Chen, Y. Zhao, K. Liu and H. Zhang, *Adv. Sci.*, 2022, **9**, 2105108.
10. G. Pan, J. Yan, Z. Tang, J. Zhang, X. Lin, D. Yang, J. Wu, W. Lin and G. Yi, *J. Mater. Chem. C*, 2022, **10**, 3959-3970.
11. W. Zhao, H. Li, Y. Chen and D. Yang, *ACS Sustainable Chem. Eng.*, 2023, DOI: 10.1021/acssuschemeng.3c00107.
12. G. Su, Z. Li, J. Gong, R. Zhang, R. Dai, Y. Deng and B. Z. Tang, *Adv. Mater.*, 2022, **34**, 2207212.
13. J. Wang, M. Zhang, S. Han, L. Zhu and X. Jia, *J. Mater. Chem. C*, 2022, **10**, 15565-15572.
14. P. Li, D. Zhang, Y. Zhang, W. Lu, J. Zhang, W. Wang, Q. He, P. Théato and T. Chen, *ACS Macro Lett.*, 2019, **8**, 937-942.
15. Z. Chen, Y. Chen, Y. Guo, Z. Yang, H. Li and H. Liu, *Adv. Funct. Mater.*, 2022, **32**, 2201009.
16. D. Lou, Y. Sun, J. Li, Y. Zheng, Z. Zhou, J. Yang, C. Pan, Z. Zheng, X. Chen and W. Liu, *Angew. Chem. Int. Ed.*, 2022, **61**, e202117066.
17. J. Liu, Z. Chen, Y. Chen, H. U. Rehman, Y. Guo, H. Li and H. Liu, *Adv. Funct. Mater.*, 2021, **31**, 2101464.
18. T. C. Bicak, M. Garnier, M. Sabbah and N. Griffete, *Chem. Commun.*, 2022, **58**, 9614-9617.
19. J. Wang, J. Nan, M. Li, G. Yuan, Y. Zhao, J. Dai and K. Zhang, *Environ. Sci. Technol. Lett.*, 2022, **9**, 739-746.
20. A. S. Rasal, S. Yadav, A. Yadav, A. A. Kashale, S. T. Manjunatha, A. Altaee and J.-Y. Chang, *ACS Appl. Nano Mater.*, 2021, **4**, 6515-6541.
21. V. Manikandan and N. Y. Lee, *Environ. Res.*, 2022, **212**, 113283.
22. J. Qiu, W. Ye, X. Xu, C. Congcong, Z. Xu, B. Lei, C. Hu, J. Zhuang, H. Dong, H. Guangqi and Y. Liu, *ACS Sustainable Chem. Eng.*, 2022, **10**, 11958-11968.
23. R. Xiong, S. Yu, M. J. Smith, J. Zhou, M. Krecker, L. Zhang, D. Nepal, T. J. Bunning and V. V. Tsukruk, *ACS Nano*, 2019, **13**, 9074-9081.
24. Y. Wu, Y. Ren, J. Guo, Z. Liu, L. Liu and F. Yan, *Nanoscale*, 2020, **12**, 20965-20972.
25. B. Sui, Y. Li and B. Yang, *Chin. Chem. Lett.*, 2020, **31**, 1443-1447.
26. Y. Wang, T. Lv, K. Yin, N. Feng, X. Sun, J. Zhou and H. Li, *Small*, 2023, **19**, 2207048.
27. J. Zhang, J. Jin, J. Wan, S. Jiang, Y. Wu, W. Wang, X. Gong and H. Wang, *Chem. Eng. J.*, 2021, **408**, 127351.
28. X. Guo, D. Xu, H. Yuan, Q. Luo, S. Tang, L. Liu and Y. Wu, *J. Mater. Chem. A*, 2019, **7**, 27081-27088.
29. J. Liu, H. Wang, T. Liu, Q. Wu, Y. Ding, R. Ou, C. Guo, Z. Liu and Q. Wang, *Adv. Funct. Mater.*, 2022, **32**, 2204686.
30. X. Yao, S. Zhang, L. Qian, N. Wei, V. Nica, S. Coseri and F. Han, *Adv. Funct. Mater.*, 2022, **32**, 2204565.
31. H. Lv, S. Wang, Z. Wang, W. Meng, X. Han and J. Pu, *Cellulose*, 2022, **29**, 6193-6204.
32. K. Zhang, Y. Shi, Y. Jia, P. Li, X. Zhang, X. Feng, L. Zhu, Y. Sun, W. Hu and G. Zhao, *J. Photochem. Photobiol., A*, 2020, **397**, 112548.

33. X. Cui, T. Honda, T.-A. Asoh and H. Uyama, *Carbohydr. Polym.*, 2020, **230**, 115662.
34. R. Soni, T.-A. Asoh, Y.-I. Hsu and H. Uyama, *Cellulose*, 2022, **29**, 1667-1678.
35. X.-X. Le, W. Lu, J. He, M. J. Serpe, J.-W. Zhang and T. Chen, *Sci. China Mater.*, 2019, **62**, 831-839.
36. X. Zhang, J. Lu, X. Zhou, C. Guo and C. Wang, *Opt. Mater.*, 2017, **64**, 1-8.
37. T. Kondo, R. Kose, H. Naito and W. Kasai, *Carbohydr. Polym.*, 2014, **112**, 284-290.
38. P. Zhao, B. Jin, Q. Zhang and R. Peng, *Langmuir*, 2021, **37**, 1760-1767.
39. F. Meierhofer, F. Dissinger, F. Weigert, J. Jungclaus, K. Müller-Caspary, S. R. Waldvogel, U. Resch-Genger and T. Voss, *The Journal of Physical Chemistry C*, 2020, **124**, 8894-8904.
40. K. Cui, Y. Chang, P. Liu, L. Yang, T. Liu, Z. Zheng, Y. Guo and X. Ma, *ACS Sustainable Chem. Eng.*, 2020, **8**, 17439-17446.
41. K. P. Shejale, A. Jaiswal, A. Kumar, S. Saxena and S. Shukla, *Carbon*, 2021, **183**, 169-175.
42. L. Wang, X. Zhang, K. Yang, L. Wang and C.-S. Lee, *Carbon*, 2020, **160**, 298-306.
43. J. Shen, Y. Zhu, X. Yang, J. Zong, J. Zhang and C. Li, *New J. Chem.*, 2012, **36**, 97-101.
44. W. Zou, X. Ma and P. Zheng, *Cellulose*, 2020, **27**, 2099-2113.
45. B. Xue, Y. Yang, R. Tang, Y. Sun, S. Sun, X. Cao, P. Li, Z. Zhang and X. Li, *Cellulose*, 2020, **27**, 729-742.
46. X. Li and Y. Hu, *Carbohydr. Polym.*, 2019, **203**, 167-175.
47. J. Guo, D. Liu, I. Filpponen, L.-S. Johansson, J.-M. Malho, S. Quraishi, F. Liebner, H. A. Santos and O. J. Rojas, *Biomacromolecules*, 2017, **18**, 2045-2055.
48. J. Huang, X. Liu, L. Li, S. Chen, J. Yang, J. Yan, F. Xu and X. Zhang, *ACS Sustainable Chem. Eng.*, 2021, **9**, 15190-15201.
49. X. Chen, Z. Song, B. Yuan, X. Li, S. Li, T. Thang Nguyen, M. Guo and Z. Guo, *Chem. Eng. J.*, 2022, **430**, 133154.
50. C. Shao, M. Wang, H. Chang, F. Xu and J. Yang, *ACS Sustainable Chem. Eng.*, 2017, **5**, 6167-6174.
51. S. Hao, C. Shao, L. Meng, C. Cui, F. Xu and J. Yang, *ACS Appl. Mater. Interfaces*, 2020, **12**, 56509-56521.
52. M. Wu, M. Pan, C. Qiao, Y. Ma, B. Yan, W. Yang, Q. Peng, L. Han and H. Zeng, *Chem. Eng. J.*, 2022, **450**, 138212.
53. G. Du, G. Gao, R. Hou, Y. Cheng, T. Chen, J. Fu and B. Fei, *Chem. Mater.*, 2014, **26**, 3522-3529.
54. L. Meng, C. Shao, C. Cui, F. Xu, J. Lei and J. Yang, *ACS Appl. Mater. Interfaces*, 2020, **12**, 1628-1639.
55. G. Nian, J. Kim, X. Bao and Z. Suo, *Adv. Mater.*, 2022, **34**, 2206577.
56. P. Du, J. Wang, Y.-I. Hsu and H. Uyama, *ACS Appl. Mater. Interfaces*, 2023, **15**, 23711-23724.
57. B. Chen and F. Wang, *Acc. Chem. Res.*, 2020, **53**, 358-367.
58. Y.-f. QU, D. LI and S.-n. QU, *Chinese Journal of Luminescence*, 2021, **42**, 1141-1154.
59. W. Kasprzyk, T. Świergosz, S. Bednarz, K. Walas, N. V. Bashmakova and D. Bogdał, *Nanoscale*, 2018, **10**, 13889-13894.
60. K. M. Omer, D. I. Tofiq and A. Q. Hassan, *Microchim. Acta*, 2018, **185**, 466.
61. Y. Song, C. Zhu, J. Song, H. Li, D. Du and Y. Lin, *ACS Appl. Mater. Interfaces*, 2017, **9**,

7399-7405.
62. S. Zhu, Q. Meng, L. Wang, J. Zhang, Y. Song, H. Jin, K. Zhang, H. Sun, H. Wang and B. Yang, *Angew. Chem. Int. Ed.*, 2013, **52**, 3953-3957.
63. Z. Qiu, X. Wang, T. Wang, X. Zhao, J. Zhang, C. Xu, J. Xu and H. Yin, *J. Mol. Liq.*, 2022, **351**, 118626.
64. Y. Liu, Z. Zhang, Z. Liang, Y. Yong, C. Yang and Z. Li, *J. Mater. Chem. A*, 2022, **10**, 16928-16940.
65. B.-Y. Wu, X.-X. Le, Y.-K. Jian, W. Lu, Z.-Y. Yang, Z.-K. Zheng, P. Théato, J.-W. Zhang, A. Zhang and T. Chen, *Macromol. Rapid Commun.*, 2019, **40**, 1800648.

# Chapter 2.

# Rapid Preparation of Dynamic-Crosslinked Cellulose Nanocomposite Hydrogel Sensors with Efficient Self-healing and Adhesion Properties

## 2.1 Introduction

Wearable electronic devices have received tremendous attention in the last few decades with potential applications in physiological signal monitoring,[1] healthcare management,[2] human-machine interaction systems,[3] soft-robotics[4] and so forth.[5] Conductive hydrogels, widely used as soft electronic materials, are formed by three-dimensional (3D) network structures containing tunable content of water and can imitate human epidermis to perceive signals from external stimuli.[6-8] Unlike conventional inorganic fillers (such as metal, metal oxide and carbon fillers etc.) embedded hydrogels, ion-conductive hydrogels are capable of meeting the requirements for preparing high performance flexible hydrogel due to their biocompatibility, structure stability and reliable ion transmission.[9-11] Therefore, it is attractive to develop ionically hydrogel-based strain sensors with combination of significant mechanical strength, fatigue resistance and high sensing stability under deformations.[12]

Until now, incorporating abundant ionic compounds into chemical cross-linking hydrogels are most commonly used methods to construct multifunctional ions-doping hydrogels.[13, 14] Although ions impart conductivity to insulating polymers, they fail in integrating superior mechanical properties because of the weak noncovalent interactions for these types of hydrogels.[15] Moreover, it is noted that the process of chemical cross-linking consumes energy and time, which is not in line with the sustainable principles.[16, 17] To address the issues, it is

essential to fabricate hydrogels using the ions through a cost-effective, time-saving, and simple process. In the latest studies, polyphenol-metal ions chemistry for rapid preparation of hydrogels are greatly explored.[18] Based on mussel-inspired chemistry, Jia et al. proposed a dual self-catalytic system composed of transition metal ions and catechol molecules, that a hydrogel with toughness, conductivity, transparency, and self-healing properties was prepared.[19] Wang *et al*. employed a dynamic oxidation and coordination system composed of sulfonated lignin and $Fe^{3+}$ to rapidly prepare a multifunctional hydrogel/coating under mild conditions. This material exhibited high transparency, conductivity, adhesion, and UV resistance.[20] Notably, lignin is a cross-linked phenolic aromatic polymer, providing important structures in the supporting tissues of vascular plants and some algae.[21] The phenolic hydroxyl and methoxy groups on lignin can be converted into quinones/catechols/semiquinones, which generate polyphenolic structures in an oxidation-reduction system.[22, 23] Hence, it is crucial but of challenge to achieve rapid preparation of multifunctional hydrogel sensors using lignin and its derivatives. Among them, sodium lignosulfonate (LS) is a great choice owing to its excellent water solubility which assist in the formation of a homogeneous polymer network in dynamic reduction system.[24] On the one hand, the catechol groups on LS enable adhesive properties that are not irritating to human skin but are easy to peel off.[25] On the other hand, they are also favored for improving the mechanical properties of the material owing to their rigid benzene structure.[26]

In addition, hydrogel sensors inevitably have to be used for a long duration, that the physical damage caused will lead to inferior mechanical properties and monitoring malfunction. Therefore, it is highly desirable to endow the conductive hydrogels with fast self-healing capabilities.[27, 28] In general, a variety of reversible molecular interactions, such as ionic interactions, hydrogen bonding and metal-ligand coordination, enable the realization of autonomous repairing.[27, 29, 30] In addition, host-guest interactions, hydrophobic association and reversible covalent bonding induced self-healing process are also attracting wide attention for

the construction of the rapid and robust self-healing hydrogels.[31-34] Among them, boronic ester bond self-healing gains significant interest in materials science and engineering due to its controllability, biocompatibility, high efficiency. and environmental adaptability.[35, 36] For instance, Yang *et al* fabricated an injectable, self-healing, and antioxidant collagen-grafted gallic acid, hyaluronic acid-grafted dopamine and γ-poly(glutamic acid) coupled with 3-aminophenylboric acid via the dynamic boronic ester bonds for wound repair.[37] Given the significant self-healing performance of boronic ester bonds, integrating promising adhesiveness and mechanical robust for rapid preparation of muti-functional hydrogel sensors in the presence of LS is of vital significance.[38, 39] Although the intermediate catechol groups in LS facilitates the formation of two reversible boronate ester bonds, more LS means an excess contents of redox catalytic system, which can lead to implosion. In view of the high demand for mechanical properties of hydrogel sensor, appropriate amounts of LS and cutting-edge material for constructing boronic ester bonds are needed to be further explored. Cellulose nanocrystals (CNC), a natural polymer found in plant cell walls, show great attention in reinforcement in composites because of the distinguishable mechanical properties and chemical reactivity.[40] Hence, CNC have been considered as suitable materials for fabricating mechanically stable self-healing hydrogels.[41]

Herein, a multi-functional hydrogel-based flexible sensor was developed through an "one-pot" strategy benefiting from LS-metal ions ($Fe^{3+}$) dynamic redox system and reversible non-covalent cross-linking formed between 3-acrylamidophenyboronic acid (APBA) and CNC. In detail, the LS-$Fe^{3+}$ dynamic catalytic system resulted in rapid copolymerization of acrylamide (AM), sodium acrylate (AAS) and APBA at room temperature in the presence of ammonium persulfate (APS) as the initiator. The synergistic interactions of massive hydrogen bonding, the boronic ester bond between APBA and CNC as well as the metal-ligand complexation of $Fe^{3+}$ and polymer chain endowed the hydrogel with reliable and efficient self-healing properties

(91.76%, 2 h). The AAS not only adjusted the pH value for formation of borate bond but also offered physical crosslinking sites, contributing to the significant toughness (699.74 kJ/$m^3$) and anti-fatigue performance. Apart from facilitating the rapid preparation system, an appropriate amount of LS avoided implosion as a dispersant and enhance mechanical strength (126.7 kPa of elongation stress). Furthermore, the intermediate catechol groups generated by LS enabled the hydrogel with repeatable self-adhesive behavior. Based on the reliable conductive traits of abundant ions ($Fe^{3+}$ and $Na^{+}$ etc.), the multifunctional hydrogel was employed as a real-time monitoring device for elderly healthcare and sleeping management, ensuring the stable transmission of movement signals. This work paved a novel avenue for efficiently developing long-lasting conductive hydrogels for wearable electronics and communicators.

## 2.2 Experimental Section

### Materials

The 3-aminophenylboronic acid monohydrate (PBA) was obtained from Tokyo Chemical Industry Co., Ltd. (TCI, Tokyo, Japan). Acryloyl chloride, sodium bicarbonate, AM, APS, iron chloride hexahydrate ($FeCl_3 \cdot 6H_2O$), tetrahydrofuran (THF), ethyl acetate and sulfuric acid (64%) were purchased from Wako Pure Chemical Industries, Ltd. (Wako, Osaka, Japan). LS was purchased from Sigma Co., Ltd. (Aldrich, USA). Cellulose was obtained from Nacalai Tesque, Inc. (Kyoto, Japan). AAS was purchased from BLD Pharmatech Ltd. (Shanghai, China). All chemicals were used without further purification. Deionized (DI) water purified using a Milli-Q system (Millipore Inc., Milford, MA), was

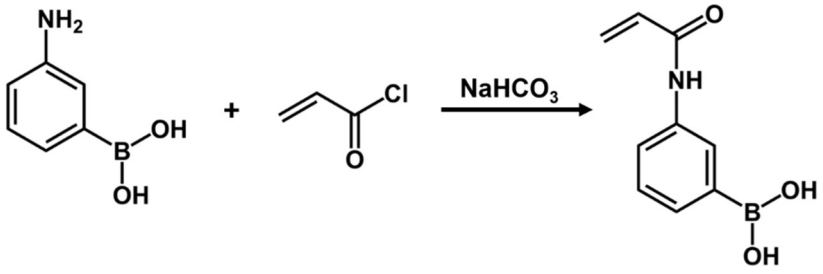


**Scheme 2-1.** The synthetic schematic of APBA.

used in all experiments.

**Synthesis of APBA**

APBA was prepared on the basis of previous reports[42, 43] and the synthetic schematic was illustrated in **Scheme 2-1**. Briefly, PBA and sodium bicarbonate were dissolved in a mixture of $H_2O$ and THF (v/v, 2:1), and the solution was subsequently cooled to 0 °C. Acryloyl chloride was added dropwise with intense stirring and then the reaction was proceeded at room temperature for additional 2 h with stirring. After that, the dry crude product was obtained by extraction of solution with ethyl acetate and rotary evaporation of organic phase. Subsequently, APBA was obtained after recrystallization in hot water (90 °C), filtration, abstersion and drying (yield, 60.5%). The successful synthesis and structure of APBA was verified by an $^1$H NMR ($d_6$-DMSO) spectrum, as shown in **Figure 2-1**.

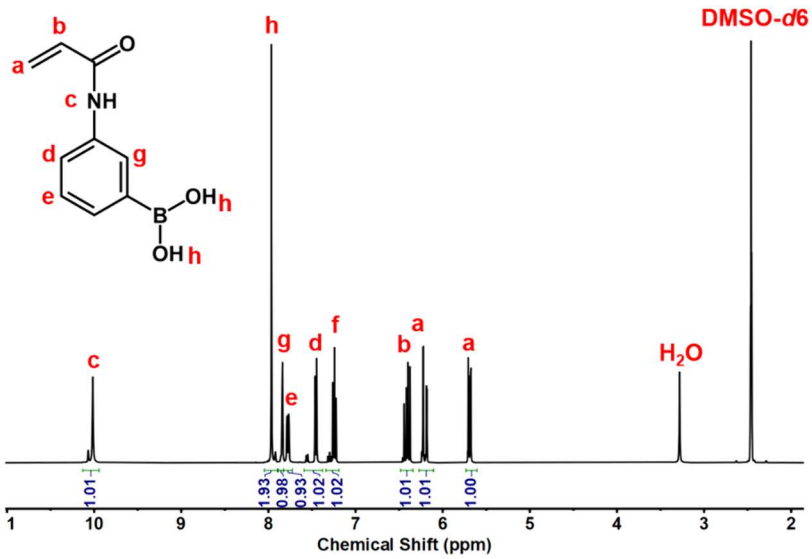


**Figure 2-1.** $^1$H NMR spectrum of APBA in $d_6$-DMSO.

**Preparation of CNC**

The preparation of CNC suspensions was conducted by sulfuric acid hydrolysis according to the modified method.[44] Specifically, a mixture of 4 g of cellulose and 200 mL of 55 wt% sulfuric acid was in a DI water bath at 50°C for 2 h with mechanical stirring (200 rpm). Later, DI water was used to diluted the obtained yellow slurry, ceasing the hydrolysis process. After that, the obtained suspension was washed with DI water and concentrated by centrifugation

repeatedly, and then dialyzed against water until pH neutrality to remove excess aqueous acid. Finally, the CNC suspension (1.46 wt%) was further homogenized through ultrasonic treatment and cryopreserved (4 ℃) before usage.

**Fabrication of LS-$Fe^{3+}$/CNC/P(AM-APBA-AAS) composite hydrogels**

LS-$Fe^{3+}$/CNC/P(AM-APBA-AAS) composite hydrogels were fabricated via a simple one-pot method at room temperature devoid of any external stimuli. First, CNC suspension was added to DI water and stirred until uniformly dispersed. Then, AM, APBA, AAS, APS and LS were added to the solution and homogeneously stirred, followed by degassing with ultrasonic cleaning for 30 min. After that, $FeCl_3$ solution was added into the above mixture solution and stirred for 10 s to obtain a homogeneous mixture. Finally, the mixture was rapidly injected into a self-made mold consisting of two quartz glass plates and one silica plate (2 mm). After 15 min, the prepared hydrogel was collected by demolding and flushed using DI water. The sample for hydrogels were denoted as LS*x*-$Fe^{3+}$/CNC/P(AM-APBA*y*-AAS), where *x*, *y* represents the mass fraction of LS in the total amount of all monomers and the molar percent ratio of APBA to AM, respectively. For example, the LS1.25-$Fe^{3+}$/CNC/P(AM-APBA1.0-AAS) hydrogel referred to a gel that the mass fraction of LS in the total amount of all monomers is 1.25% and the molar percent ratio of APBA to AM is 1.0%. The detailed compositions of the hydrogels were summarized in **Tables 2-1** and **2-2**.

**Table 2-1.** The content of LS of composite hydrogels

| Samples | AM (g) | AAS (mg) | APBA (mg) | CNC (mg) | LS (mg) | $FeCl_3·6H_2O$ (mg) | APS (mg) | $H_2O$ (mL) |
|---|---|---|---|---|---|---|---|---|
| LS0.5-$Fe^{3+}$/CNC/P(AM-APBA1.0-AAS) | 2.8 | 75 | 76 | 20 | 15 | 20 | 30 | 6 |
| LS0.75- | 2.8 | 75 | 76 | 20 | 22 | 20 | 30 | 6 |

| | | | | | | | | |
|---|---|---|---|---|---|---|---|---|
| $Fe^{3+}$/CNC/P(AM-APBA1.0-AAS) | | | | | | | | |
| LS1.0-$Fe^{3+}$/CNC/P(AM-APBA1.0-AAS) | 2.8 | 75 | 76 | 20 | 30 | 20 | 30 | 6 |
| LS1.25-$Fe^{3+}$/CNC/P(AM-APBA1.0-AAS) | 2.8 | 75 | 76 | 20 | 37 | 20 | 30 | 6 |
| LS1.5-$Fe^{3+}$/CNC/P(AM-APBA1.0-AAS) | 2.8 | 75 | 76 | 20 | 44 | 20 | 30 | 6 |

**Table 2-2.** The content of APBA of composite hydrogels

| Samples | AM (g) | AAS (mg) | APBA (mg) | CNC (mg) | LS (mg) | $FeCl_3 \cdot 6H_2O$ (mg) | APS (mg) | $H_2O$ (mL) |
|---|---|---|---|---|---|---|---|---|
| LS1.25-$Fe^{3+}$/CNC/P(AM-APBA0-AAS) | 2.8 | 75 | 0 | 20 | 37 | 20 | 30 | 6 |
| LS1.25-$Fe^{3+}$/CNC/P(AM-APBA0.5-AAS) | 2.8 | 75 | 38 | 20 | 37 | 20 | 30 | 6 |
| LS1.25-$Fe^{3+}$/CNC/P(AM-APBA1.0-AAS) | 2.8 | 75 | 76 | 20 | 37 | 20 | 30 | 6 |
| LS1.25-$Fe^{3+}$/CNC/P(AM-APBA1.5-AAS) | 2.8 | 75 | 114 | 20 | 37 | 20 | 30 | 6 |
| LS1.25- | 2.8 | 75 | 152 | 20 | 37 | 20 | 30 | 6 |

| |
|---|
| $Fe^{3+}$/CNC/P(AM-APBA2.0-AAS) |

**Characterization of the redox reactions between the LS and $Fe^{3+}$**

The redox products of the LS-$Fe^{3+}$ were measured by X-ray photoelectron spectroscopy (XPS, JEOL JPS-9010MC). Before that, the solution of $FeCl_3 \cdot 6H_2O$ mixed with LS solution underwent lyophilization to form the solid pair of LS-$Fe^{3+}$. The UV-vis absorption spectroscopy (J-820 AC, JASCO Corporation, Japan) was used to record the characteristic absorption of LS and LS-$Fe^{3+}$ chelate solutions.

**Morphological observation**

The cross section and surface elemental composition of the fractured freeze-dried hydrogels was measured using scanning electron microscopy (SEM, Hitachi SU3500) with an accelerating voltage of 10 kV and energy-dispersive X-ray spectroscopy (EDX, HITACHI, Miniscope TM 3000 equipped with Swift ED 3000). Prior to morphological observation, the hydrogel samples were immersed in liquid nitrogen for 3 minutes and fractured before freeze-drying. The morphologies of CNC were characterized using atomic force microscope (AFM, SPI3800N/SPA-400, Seiko Instruments Inc., Tokyo, Japan).

**Mechanical tests**

The mechanical properties of the hydrogel samples were carried out using a universal material testing machine (Shimadzu EZ-Graph, Shimadzu Corporation) on strip-shaped hydrogel samples (15 mm in gauge length, 10 mm in width and 2 mm in thickness) with a 100 N load cell at a constant stretching rate of 100 mm/min. The compressive tests were conducted on the same machine equipped with a 500 N load cell and a speed of 3.0 mm/min at room temperature, using the samples with length of 8-11 mm and a diameter of 16 mm. The Young's

modulus was calculated from the slope of the initial linear region in the range 5-15% of the stress-strain curves and the toughness was calculated from the area of stress-strain curves. In loading-unloading tensile tests, the hydrogel specimen was stretched to a predetermined maximum strain and then retracted to its initial length at a consistent deformation rate of 100 mm/min. There was no waiting interval between successive cycle tests. The dissipated energy was calculated as the area enclosed by the loading-unloading curves. The dissipation ratio was computed as follows:

$$Dissipation\ ratio = 100\%((\int_{loading} \sigma\, d\varepsilon - \int_{unloading} \sigma\, d\varepsilon)/\int_{loading} \sigma\, d\varepsilon) \qquad (2.1)$$

where σ and ε represent the stress and strain, respectively.[45]

**Self-healing tests**

The strip-shaped samples were bisected using blades and the two separated halves were promptly brought into contact without applying stress and stimulate, then stored in a sealed vessel to reduce water evaporation. Uniaxial tensile test was used to test and calculate the self-healing efficiency of gels, defined as the ratio of tensile strength between the healed gel and the original gel.[46] The step-strain measurement of the gel was conducted to assess the self-healing performance of hydrogel, using Haake Rheostress 6000 (Thermo Fisher Scientific, Waltham, MA, USA). At a fixed frequency (1.0 Hz), amplitude oscillatory strains were switched from small strain (1.0%) to subsequent large strain (500%) with 100 s for every strain interval.

**Adhesion test**

The adhesive strengths between hydrogel with various substrates were measured by lap shear tests using the Shimadzu EZ-Graph universal test machine equipped with a 10 N load cell and a 30 mm/min loading rate. The specimens were cut into 20 mm × 20 mm and sandwiched between two same substrates attached to the plates. The adhesive strength was determined by dividing the maximum load by the initial adhesion area.[47]

**Electrical assessment**

The relative resistance under different strains and human motions of hydrogel sensors was recorded using a digital LCR meter (TH2830, Changzhou Tonghui Electronic Co. Ltd.) in real time. The relative resistance change was computed as follows:

$$\Delta R/R_0 = \frac{R-R_0}{R_0} \times 100\% \quad (2.2)$$

where $R_0$ is the original resistance and R represent the real-time resistance after deformation. The gauge factor (GF) was defined as the following:

$$GF = \frac{R-R_0}{R_0 \varepsilon} \quad (2.3)$$

where ε represent the corresponding strain change.[47] All the experiments were performed in compliance with the guidelines established by the Osaka University, Osaka, Japan. All relevant ethical regulations were complied with and informed consent was obtained from all participants.

## 2.3 Results and Discussion

**Design route and rapid preparation of the composite hydrogels**

The preparation of traditional hydrogels inevitably requires continuous heating or ultraviolet radiation to initiate free radical polymerization. This not only makes the preparation process complex, time-consuming, and energy-intensive but also involves toxic chemical crosslinking agents (*N, N′*-methylenebisacrylamide) and auxiliary agents (tetramethylethylenediamine) used to form the hydrogel, which can have adverse environmental effects.[20] On the other hand, the comprehensive properties of conventional hydrogels such as adhesiveness, self-healing, conductivity and flexibility are generally insufficient, which limits their practical applications.[48] To address these challenges, the author utilized an LS-$Fe^{3+}$ dynamic catalytic system, three monomers and CNC, without the need for

chemical crosslinking agents. Thus, the initiator APS was rapidly activated at room temperature, thereby initiating dynamic crosslinking of polymer chains, resulting in a multifunctional hydrogel with conductivity, self-healing, and self-adhesive properties. As shown in **Figure 2-2**, specifically, this rapid self-catalytic strategy was based on the dynamic redox reactions between the LS-$Fe^{3+}$ chelates during which the hydroxyl and methoxy groups of LS were oxidized into semiquinone and quinone groups, concomitantly $Fe^{3+}$ was reduced to $Fe^{2+}$. Subsequently, APS was activated to generate hydroxyl radicals, initiating the rapid polymerization of AM, APBA, and AAS monomers in the absence of external stimuli. Given that APS can cyclically re-oxidize $Fe^{2+}$ to $Fe^{3+}$ and quinone groups can be converted into catechol groups, the multiple dynamic redox reactions between LS-$Fe^{3+}$ and APS established a reversible quinone-catechol redox equilibrium environment, enabling the cyclic recurrence of this process. As a result, LS-$Fe^{3+}$/CNC/P(AM-APBA-AAS) composite hydrogels were quickly formed at room temperature, due to multiple dynamic cross-linking interactions, including dynamic boronic ester bonds, ionic coordination bonds, and hydrogen bonds. More precisely, the P(AM-APBA-AAS) polymer chains coordinate with $Fe^{3+}$ to form a primary dynamic cross-linked network, employing self-healing and conductivity to the hydrogel. The phenylboronic acid groups

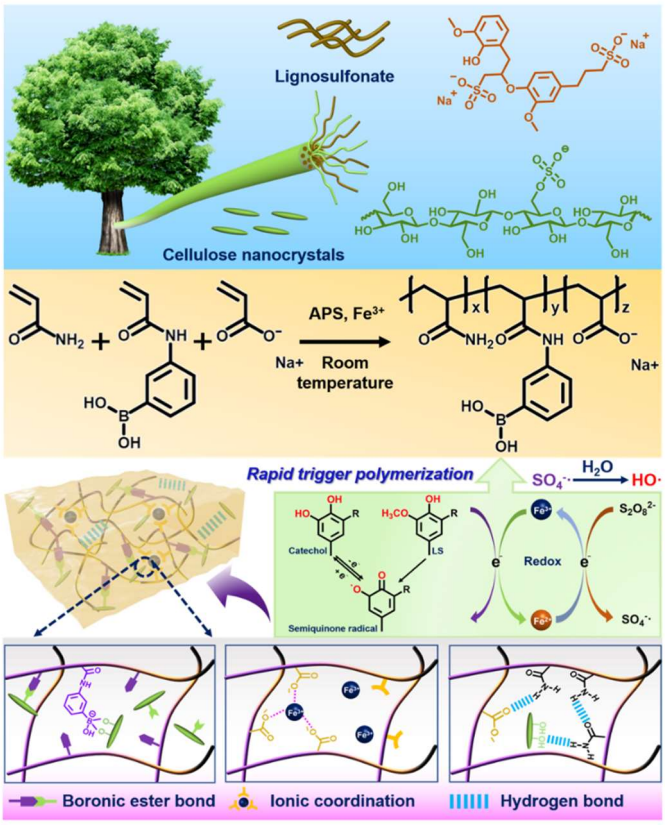


**Figure 2-2.** Designing strategy for LS-$Fe^{3+}$/CNC/P(AM-APBA-AAS) hydrogels based on the dynamic catalytic strategy.

and cis-diols reacting between CNC and polymer chains to form dynamic boronic ester bonds, facilitating rapid aggregation of the hydrogel. In addition, intermolecular and intramolecular hydrogen bonds between polymer chains and CNC contribute to the enhancement of both mechanical strength and self-healing properties. The well-designed multiple dynamic crosslinking networks not only make the hydrogel preparation process more environmentally friendly but also facilitate rapid and effective self-healing of the hydrogel to dynamically reconfigure and autonomously recover after mechanical disruption. Simultaneously, they enhance elasticity and multifunctionality, endowing the hydrogel with significant potential in the field of multifunctional flexible wearable devices.

The XPS and UV-vis measurements were used to analyze the dynamic redox reaction in LS-$Fe^{3+}$ dynamic catalytic system. As shown in **Figure 2-3**, compared with the broad scan of the LS with mainly C 1s (~284 eV) peaks and O 1s peaks (~532 eV), distinct Fe 2p (~703 eV) appeared in the LS-$Fe^{3+}$ chelates. Furthermore, the LS-$Fe^{3+}$ chelates exhibited a higher content of C=O groups and a lower content of C-O groups than LS (**Figure 2-3b-c**). Additionally, both $Fe^{3+}$ and $Fe^{2+}$ were detected in the LS-$Fe^{3+}$ chelates.[26] In the UV-vis spectra of LS and LS-$Fe^{3+}$ solutions (**Figure 2-3d**), the generation of quinone and semiquinone groups can be confirmed in LS-$Fe^{3+}$ chelates solution.[48] The above results proved that the reducing groups of LS can undergo a redox reaction with $Fe^{3+}$, resulting in the substantial generation of quinone intermediates and $Fe^{2+}$. Hence, the reversible redox environment provided by LS-$Fe^{3+}$ dynamic catalytic system was the decisive factor for achieving rapid hydrogel polymerization.[49] The thermal imaging diagrams showed that the temperature of hydrogel precursor solution with LS-$Fe^{3+}$ increased rapidly within 10 min, indicating a substantial release of heat during this period (**Figure 2-3e**). Conversely, the hydrogel precursor solution without $Fe^{3+}$ was unable to be triggered and remained in a flowing liquid state. Additionally, no heat was noted. At the result, the LS-$Fe^{3+}$/CNC/P(AM-APBA-AAS) hydrogel could formed in 15 min at room temperature

without any additional energy introduction. Moreover, the cross-section of the freeze-dried LS-$Fe^{3+}$/CNC/P(AM-APBA-AAS) hydrogel was observed via using SEM and EDX methods. As shown in **Figure 2-3f,** a unique hierarchical porous morphology with filamentous structure within adjacent bundles was observed in the swelling equilibrium hydrogel, indicating CNC associated with polymer chains by multiple noncovalent bonds.[50] This interwoven 3D porous structure facilitates electron transport in the conductive hydrogel under different deformations.[49] Further, **Figure 2-3g** exhibited the homogeneous distribution of C, N, O, B and Fe elements in the matrix.

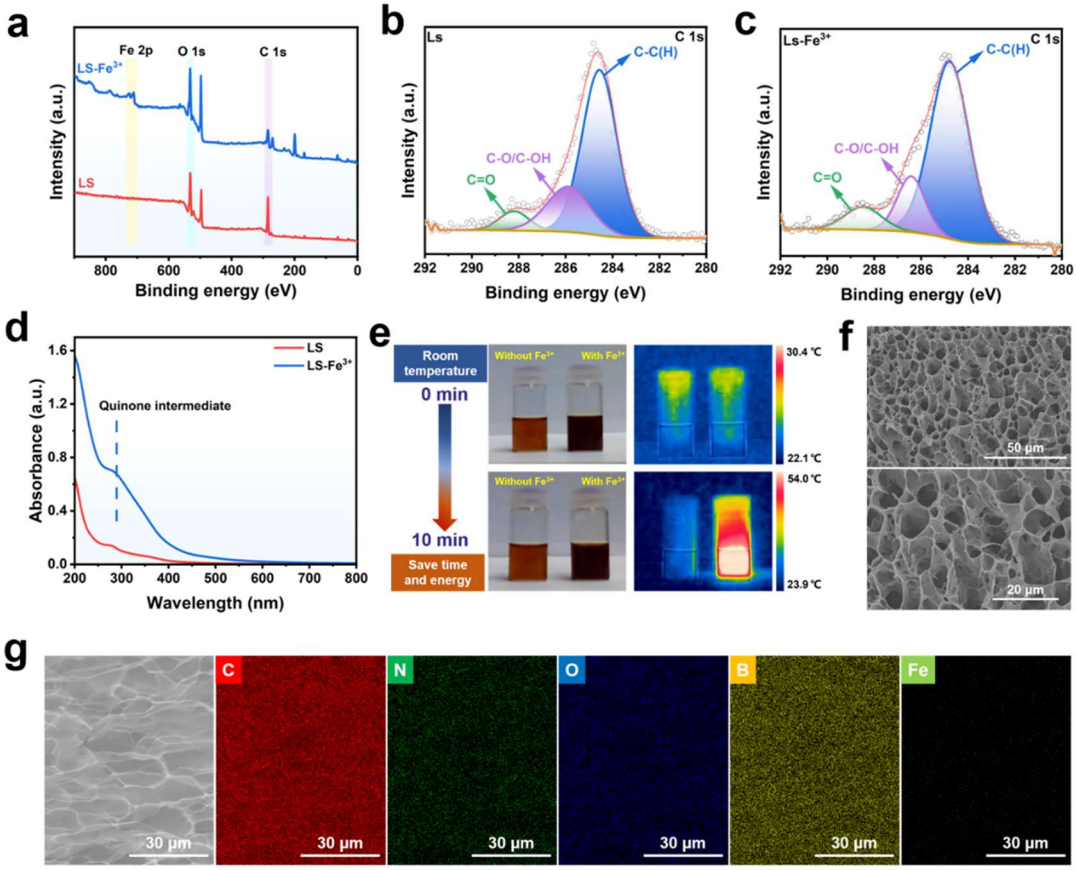


**Figure 2-3**. (a) XPS survey spectra of LS and LS-$Fe^{3+}$ chelates. (b-c) High-resolution XPS fitting results for C 1s of LS and LS-$Fe^{3+}$ chelates. (d) UV-vis spectra of LS and LS-$Fe^{3+}$ suspensions. (e) Photographs of the self-exothermic process of the LS-$Fe^{3+}$/CNC/P(AM-APBA-AAS) hydrogel without $Fe^{3+}$ (left) and with $Fe^{3+}$ (right) at room temperature. (f) SEM images and (g) elemental (C, N, O, B and Fe) mapping of the freeze-fractured cross section of swelling equilibrium LS-$Fe^{3+}$/CNC/P(AM-APBA-AAS) hydrogel.

### Mechanical properties of LS-$Fe^{3+}$/CNC/P(AM-APBA-AAS) hydrogels

The extraordinary stretchability and toughness achieved in conductive hydrogels are pivotal factors in ensuring their structural integrity as flexible sensors under repeated deformation, thereby preventing premature failure during daily usage. Hence, a series of experiments were undertaken to investigate the impact of each component on the mechanical properties of hydrogels employing a universal testing machine. First, the impact of different amounts of LS addition on the mechanical performances was explored through tensile tests. As shown in **Figure 2-4a-b**, as the LS content is increased from 0.5 to 1.5%, the tensile stress of hydrogels increases from 64.99 to 134.08 kPa, the corresponding toughness increases from 296.40 to 672.23 kPa, while the tensile strain and elastic modulus gradually increase until the LS content exceeds 1.25%. On the contrary, the sample without the addition of LS (LS0-$Fe^{3+}$/CNC/P(AM-APBA1.0-AAS)) not only required a catalyst (*N, N, N, N*-Tetramethylethylenediamine) and a longer preparation time (room temperature, 48 h), but also exhibited significantly lower mechanical performance compared to samples with LS added. This is due to the fact that the LS-$Fe^{3+}$ chelates can impact the crosslinking of the hydrogel and intertwine with the P(AM-APBA-AAS) chains through hydrogen bonding, thereby enhancing the rigidity of the hydrogel.[20, 48] Moreover, it is important to mention that that when the LS content exceeded 1.25%, the mechanical properties of the hydrogel deteriorated, leading to significant variations among samples. This may be attributed to an excess of lignin, which can disrupt the covalent cross-linking network within the gel, and the same phenomenon was observed by Li *et al.*[51] In addition, with a fixed LS content of 1.25%, the effect of APBA addition on the mechanical properties of the hydrogel was investigated. When the molar percent ratio of APBA to AM increased from 0 to 1.0%, the corresponding hydrogel exhibited increased fracture elongation, tensile strength, and toughness (**Figure 2-4c-d**). Although the hydrogel without APBA (LS1.25-$Fe^{3+}$/CNC/P(AM-APBA0-AAS) hydrogel) demonstrated a higher elastic modulus, its relatively stiff, fragile and brittle properties limit deformation space,

resulting in a macroscopic appearance of reduced toughness.[49] Furthermore, the rapid gelation process can result in uneven gel network density,[52] leading to brittleness issues, which can be effectively mitigated by the addition of APBA. Compared with LS1.25-$Fe^{3+}$/CNC/P(AM-APBA1.0-AAS), after continuing to increase the amount of APBA, the mechanical properties of hydrogels did not significantly improve, or even slightly decreased, which may be because the water solubility of APBA was limited.[43] Meanwhile, the LS1.25-$Fe^{3+}$/CNC/P(AM-APBA1.0-AAS) hydrogel exhibited a suitable Young's modulus (≈39.50 kPa) and toughness (≈699.74 kJ/$m^3$), which was equivalent to that of the human skin (0.01-1.75 MPa and 0.1-12 MJ/$m^3$, respectively).[26] This ensures the potential mechanical compatibility of the hydrogel with human skin, achieving a dependable and comfortable human-machine interface.[48]

The multiple dynamic crosslinking networks in LS-$Fe^{3+}$/CNC/P(AM-APBA-AAS) provide it with the capacity for rapid reconstruction and recovery once external pressure is released.[53] Hence, the elastic restorability and antifatigue performance of LS1.25-$Fe^{3+}$/CNC/P(AM-APBA1.0-AAS) hydrogel was further investigated by cyclic tensile experiments. As shown in **Figure 2-4e**, the hydrogel was conducted to ten consecutive loading-unloading cycles at 400% strain. The hysteresis loops became narrow after the first cycle and remained relatively stable, which probably related to the damage of the physical network inside the gel during the initial loading-unloading process.[25] Furthermore, the dissipation energy stabilized at 15.48 and 12.13 kJ/$m^3$ during the second to tenth cycles, respectively, while the dissipation ratio maintained at around 10% (**Figure 2-4f**), indicating the excellent fatigue resistance of the hydrogel. Apart from the anti-fatigue capability, the hydrogel exhibited elastic restorability during a cyclic stretching test at 100-600% strain as shown in **Figure 2-4g**. As the strain increased, the hysteresis loop's area expanded, indicating a greater dissipation of energy during deformation due to the dissociation of hydrogen bonds and coordination bonds.[53] From **Figure 2-4h**, the dissipated energy increased from 4.61 to 50.65 kJ/m³, and the calculated

dissipation ratio also increased from 22.61% to 31.28% as the strain increased from 100% to 600%, respectively. The results indicated that the multiple dynamic crosslinking hydrogel can be self-adapting to cyclic stretching within the extremely wide strain range and display high elasticity.[45] Furthermore, the reversible interactions also protect the hydrogel from injuries caused by sharp materials. For example, whether it is a sheet-like hydrogel (2 mm) pierced from bottom to top by the blade of scissors or a cylindrical hydrogel cut from top to bottom by a sharp blade, the hydrogel returned to its initial state upon removal of the blade without leaving any noticeable traces, thereby confirming the effective energy dissipation of the hydrogel (**Figure 2-4i**).

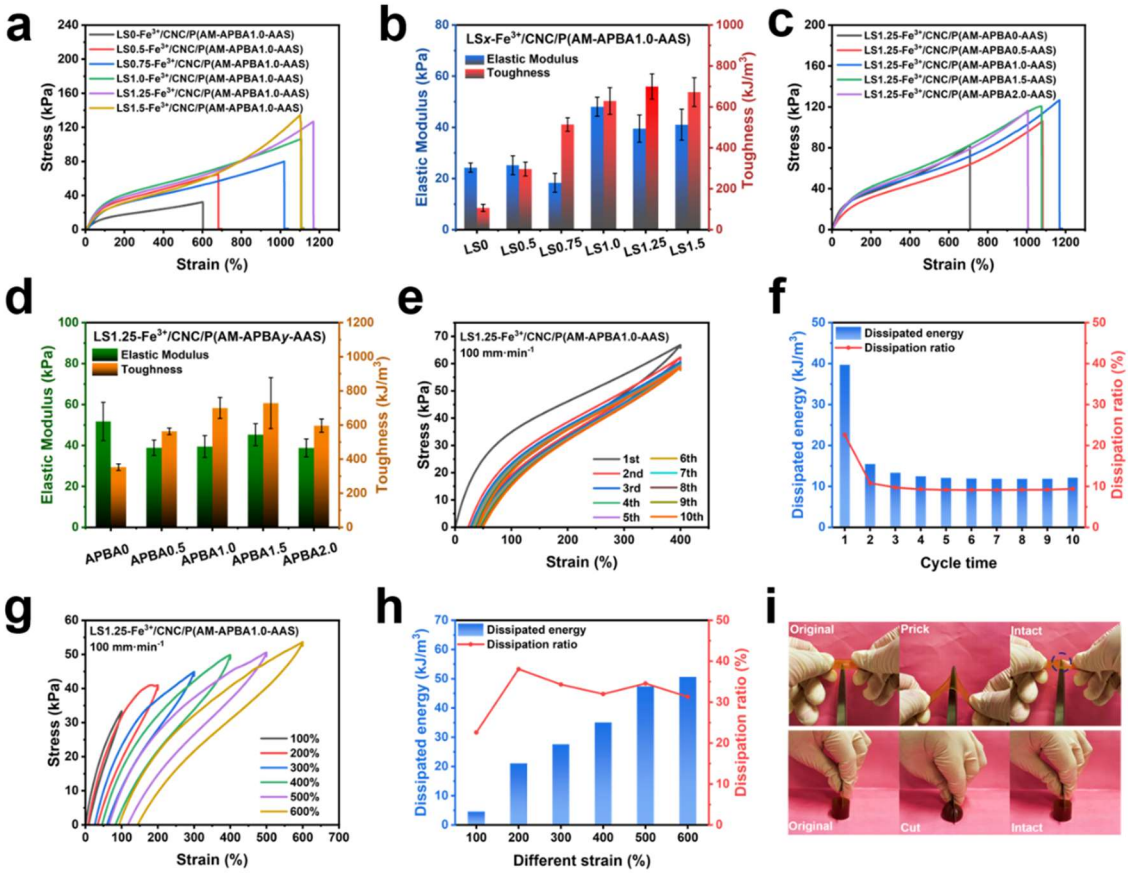


**Figure 2-4.** (a) Tensile stress-strain curves, (b) corresponding elastic modulus and toughness of hydrogels with different amounts of LS addition. (c) Tensile stress-strain curves, (d) corresponding elastic modulus and toughness of hydrogels with different amounts of APBA addition. (e) Cyclic loading-unloading stress-strain curves, (f) corresponding dissipated energy and dissipation ratio of LS1.25-$Fe^{3+}$/CNC/P(AM-APBA1.0-AAS) hydrogel under 400% strain for 10 cycles. (g) Cyclic tensile curves, (h) corresponding dissipated energy and dissipation ratio of LS1.25-$Fe^{3+}$/CNC/P(AM-APBA1.0-AAS) hydrogel under the strain from 100 to 600%.

(i) Photographs indicating the LS1.25-$Fe^{3+}$/CNC/P(AM-APBA1.0-AAS) hydrogel withstanding cut and puncture by a sharp knife and a scissor blade and recovering its original shape.

**Self-Healing performance of LS-$Fe^{3+}$/CNC/P(AM-APBA-AAS) hydrogels**

The self-healing capability can expand the application range of hydrogels as flexible sensors, ensuring a longer service life.[54] The author used LS1.25-$Fe^{3+}$/CNC/P(AM-APBA1.0-AAS) as an example to assess the self-healing capability of the LS-$Fe^{3+}$/CNC/P(AM-APBA-AAS) hydrogel. As shown in **Figure 2-6a**, a disk-shaped sample dyed with methylene blue and original sample were cut in half, and then the incisions of different colored parts were quickly brought into contact. It can be observed that they rapidly integrated due to adhesion and self-healing effects, and were not easily separated. Subsequently, they were sealed and stored at room temperature without any external intervention. After 2 h, the healed hydrogel could stand on its own and even withstand huge stretching perpendicular to the cutting surface without detaching (**Figure 2-5a**), and the healed rectangular strip sample could be stretched freely (**Figure 2-5b**). Moreover, the complete disappearance of the incision was confirmed through optical microscopy after 2 h (**Figure 2-6f**). The above results indicate that the dynamic network and mechanical strength of the hydrogel are restored[36], and this self-healing behavior is not a simple adhesion. The step-strain measurement was then performed to evaluate the self-healing behavior of the LS1.25-$Fe^{3+}$/CNC/P(AM-APBA1.0-AAS) hydrogel (**Figure 2-6c**). At a fixed

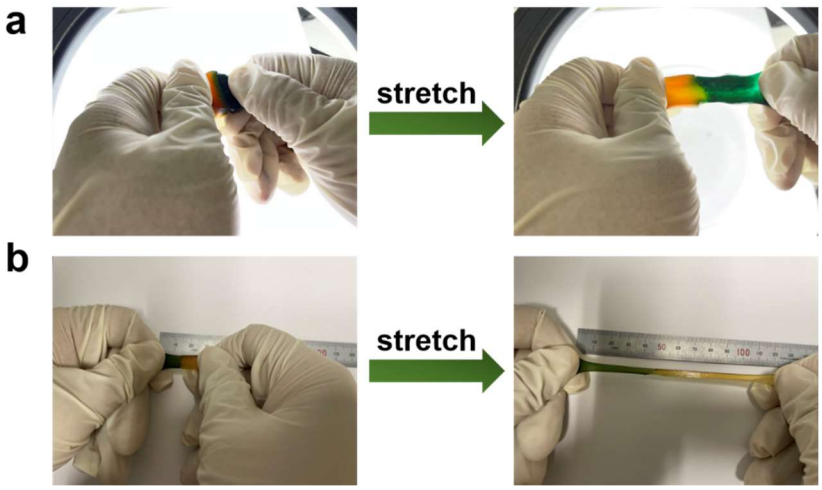


**Figure 2-5.** Stretchable property of (a) disk-shaped and (b) Rod-shaped LS1.25-$Fe^{3+}$/CNC/P(AM-APBA1.0-AAS) hydrogels after self-healing.

frequency of 1.0 Hz, when subjected to small amplitude oscillatory shear (1% strain), the storage modulus (*G*') was greater than the loss modulus (*G*"), showing quasi-solid characteristics. However, when subjected to large amplitude oscillatory shear (500% strain), *G*' immediately dropped below 10 Pa, with *G*' becoming smaller than *G*", suggesting disruption of the gel network. Once the applied strain was switched to 1%, *G*' and *G*" immediately returned to the initial values, indicating the rapid recovery of the gel internal network. Even after five cycles, no significant decrease in modulus was observed, demonstrating the hydrogel has robust good self-healing property. **Figure 2-6b** illustrates that the self-healing process of hydrogels may be attributed to the effective reestablishment of multiple dynamic interactions (dynamic boronic ester bonds, ionic coordination bonds, and hydrogen bonds) within the three-dimensional network. The author further quantitatively evaluated the corresponding healing efficiency of LS1.25-$Fe^{3+}$/CNC/P(AM-APBA1.0-AAS) hydrogel through tensile tests for different periods at room temperature. As shown in **Figure 2-6d**, the breaking strength and strain of the hydrogels gradually recovered to the original values as the healing time extended. After 2 h of self-healing, the tensile strength and strain at the fracture had respectively reached 91.76% and 98.18% of their initial values, exhibiting high self-healing efficiency. This self-healing process was also demonstrated by connecting the hydrogel into a series circuit with green light-emitting diode (LED) to investigate it's electrical repairability and conductive stability (**Figure 2-6g**). The LED bulb lit up when power was applied, but after the gel was cut into two halves, the bulb went out due to the disruption of the conductive path. When the cut parts touched each other, the LED bulb quickly illuminated again. This process could be repeated for many cycles without significant changes in the brightness of the LED bulb. Meanwhile, the resistance changes during cutting-healing cycles were quantitatively measured (**Figure 2-6h**). When the gel was cut, the resistance in the circuit was infinite. Once the gel sections contacted, the resistance quickly returns to its initial value. These results confirm that

multiple dynamic bonding within the LS-$Fe^{3+}$/CNC/P(AM-APBA-AAS) hydrogel gel could endow it with excellent electrical repairability, enabling the rapid reconnection of the conductive network.

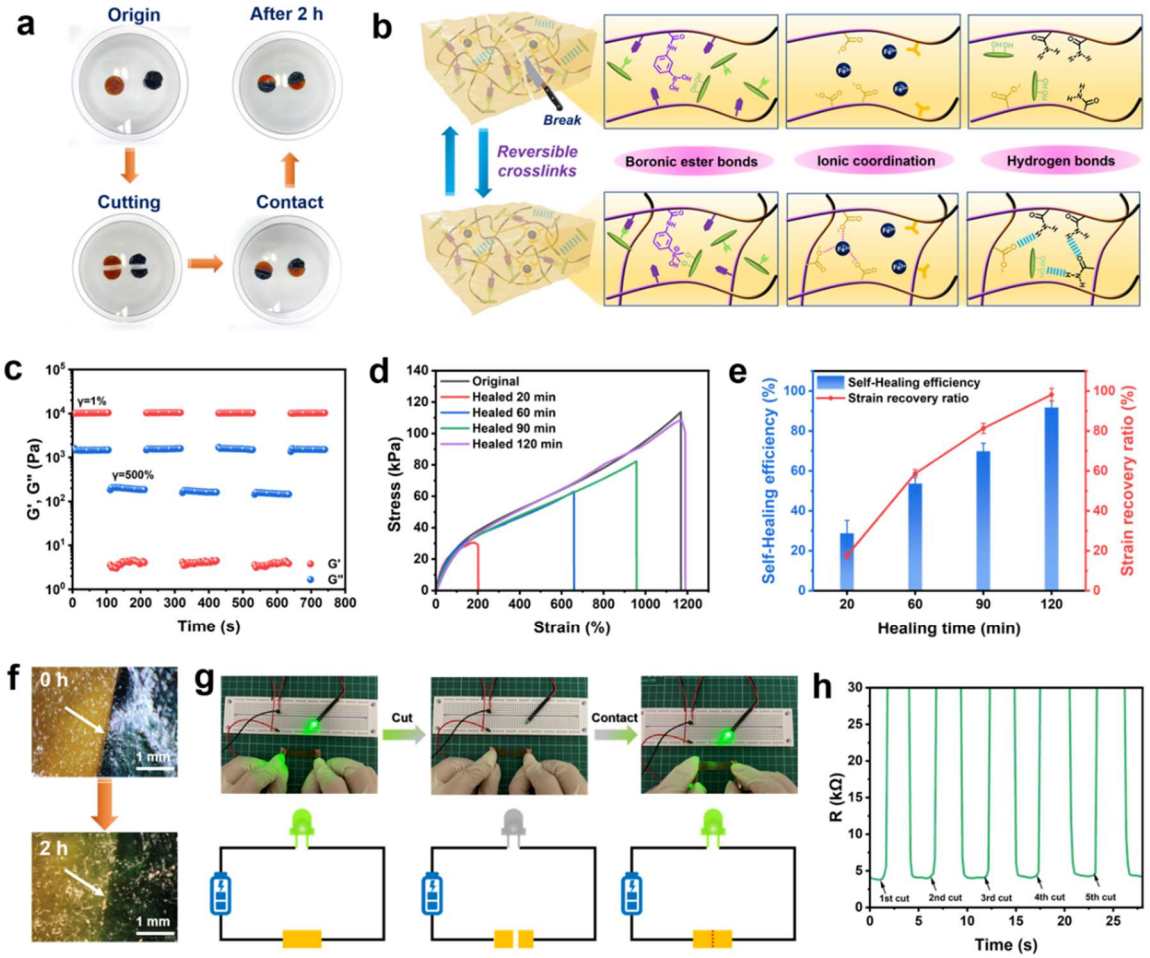


**Figure 2-6.** (a) Images of the two LS1.25-$Fe^{3+}$/CNC/P(AM-APBA1.0-AAS) hydrogels cut into two pieces and healed under ambient conditions (one stained with methylene blue). (b) Schematic diagram of the self-healing mechanism. (c) *G′* and *G″* of the cyclic steps with shear strain switching between small (1%) and large (500%) strains at a fixed frequency (1.0 Hz). (d) Tensile stress-strain curves and (e) stress self-healing efficiency of hydrogel samples healing at varying healing times. (f) Optical microscopy photos of the cut surfaces before and after healing. (g) Schematic diagram and digital photos showing the brightness changes of the LED bulb during the hydrogel cutting/healing process. (h) Electrical resistance changes during the hydrogel cutting/healing process.

### Self-adhesion performance of LS-$Fe^{3+}$/CNC/P(AM-APBA-AAS) hydrogels

Given the abundant catechol and semiquinone groups in oxidized lignin, it becomes feasible to create non-covalent interactions for building adhesive interfaces.[55] As expected, LS-

$Fe^{3+}$/CNC/P(AM-APBA-AAS) hydrogels exhibited excellent adhesion properties to various hydrophilic and hydrophobic surfaces without requiring any surface treatment. It can be seen from **Figure 2-7b** that LS1.25-$Fe^{3+}$/CNC/P(AM-APBA1.0-AAS) hydrogel could easily adhere to a variety of substrates, including plastic, glass, metal, rubber, silicone, porcine skin, ceramic, PTFE, wood and paper. To further quantify the adhesion strength of hydrogels, the lap shear test was conducted **(Figure 2-7a)**. As shown in **Figure 2-7c**, the maximum adhesion strengths in the interface of wood, plastic, glass, porcine skin, metal and PTFE reached 37.7, 18.8, 17.0, 12.8, 7.9, and 6.8 kPa, respectively. In comparison to other substrates, the hydrogel exhibited the highest adhesive strength with wood, primarily due to the rough and porous nature of wood surfaces, which provide a larger contact surface area with the hydrogel. Furthermore, the hydrophilic properties of wood surfaces make them easily wettable by the hydrogel, facilitating a strong bond through hydrogen bonding.[56]

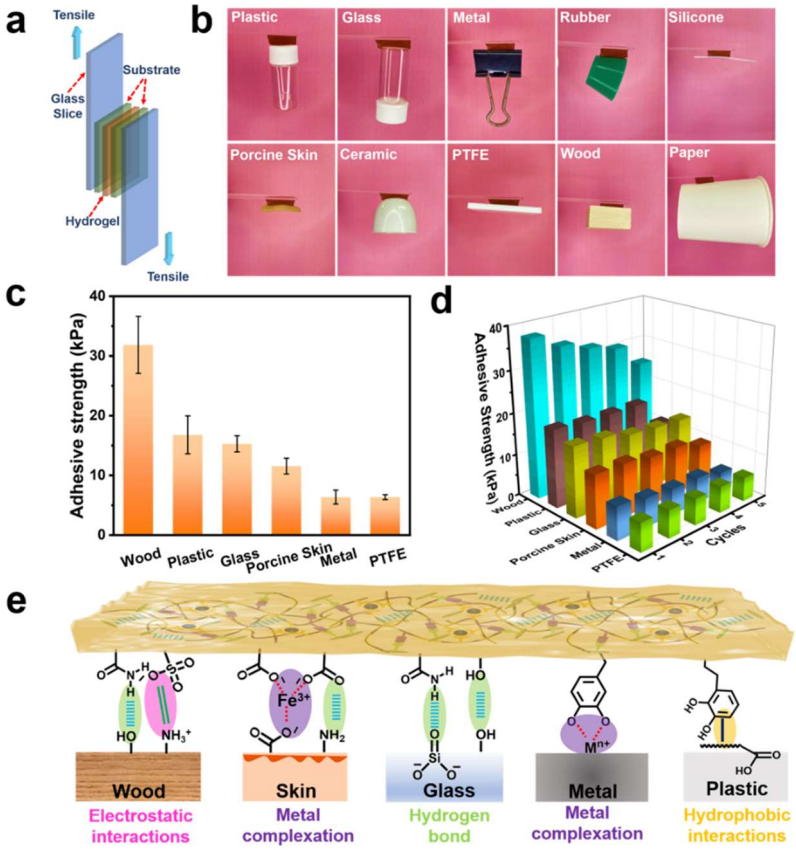


**Figure 2-7.** (a) Schematic diagram of the lap shear tests. (b) Photographs of the adhesion ability to different substrates. (c) Adhesion strength of the LS1.25-$Fe^{3+}$/CNC/P(AM-APBA1.0-AAS) hydrogel on different substances. (d) Successive adherence and separation cycles on different substrates. (e) Possible interactions between the gel and various substrates.

Cyclic lap shear tests were conducted on the same sample to investigate the reusability of the LS1.25-$Fe^{3+}$/CNC/P(AM-APBA1.0-AAS) hydrogel. As depicted in **Figure 2-7d**, the

adhesion strength of the hydrogel to wood, plastic, glass, porcine skin, metal and PTFE reduced to 66.0%, 59.5%, 82.0%, 74.2%, 74.2%, 60.0% and 84.5% of the original value, respectively, after 5 times of consecutive peeling-adhesion, indicating that the hydrogel had remarkable adhesion reusability. The stabilizing and robust adhesion effect of LS-$Fe^{3+}$/CNC/P(AM-APBA-AAS) hydrogels to substrates can be explained by the synergistic effect between the amino, carboxyl and catechol groups within the polymer chains and various substrate materials, such as electrostatic interactions, metal complexation, hydrogen bonding and hydrophobic interaction (**Figure 2-7e**).

**Sensing performance**

The exceptional tensile toughness, self-healing ability, and remarkable adhesion properties of the prepared LS1.25-$Fe^{3+}$/CNC/P(AM-APBA1.0-AAS) hydrogel (conductivity up to 2.14 mS/cm) bestow it with extensive application potential in the field of strain sensing. As shown in **Figure 2-8a**, when the hydrogel was connected in series to the circuit, the brightness of the LED bulb gradually dimmed as the strain increases from 0% to 600%, and then, as the strain decreased, the brightness of the LED bulb gradually recovered. This phenomenon could be attributed to the stretching, which caused the elongation and narrowing of the ionic transport path, implying the excellent strain sensitivity of the hydrogel. Subsequently, the sensing performance of the hydrogel was further evaluated through a tensile test with a maximum strain of 500%. Typically, the slope of the relative resistance change versus strain is employed to calculate the gauge factor (GF), enabling a quantitative assessment of the strain sensitivity of the hydrogel. As depicted in **Figure 2-8b**, within the strain range of 0-500%, the relative resistance change exhibited a linear increase as the strain increased. Linear regression analysis was applied to four segments of the GF curve, yielding values of 2.20 (0-100%), 4.40 (100-200%), 6.73 (200-350%), and 8.98 (350-500%), respectively. It is noteworthy that at a strain of

500%, the gauge factor (GF) reached an impressive value (8.98), surpassing the GF values reported for previously developed conductive hydrogel sensors. This extraordinary sensitivity underscores the hydrogel's potential for use as a strain sensor across a wide operating range while maintaining stable electrical signal responses. **Figure 2-8c** illustrated the trend in relative resistance change for the hydrogel during the step-by-step loading-unloading process, displaying a distinct stair-stepping curve. Notably, there was no observable resistance hysteresis, whether the hydrogel sensor was loaded or unloaded to a specific strain. Meanwhile, 5 cycles of tensile tests were conducted on the hydrogel sensor under different strains. As depicted in **Figure 2-8d-e**, whether subjected to a small strain (1%-50%) or a large strain (100%-500%), the electrical signals produced by the hydrogel sensor during 5 stretch-release cycles at the same strain remained consistent, indicating remarkable sensitivity and reversibility. Moreover, the sensitivity of the hydrogel sensor remained unaffected by the stretching speed. In **Figure 2-8f**, there were no significant detectable

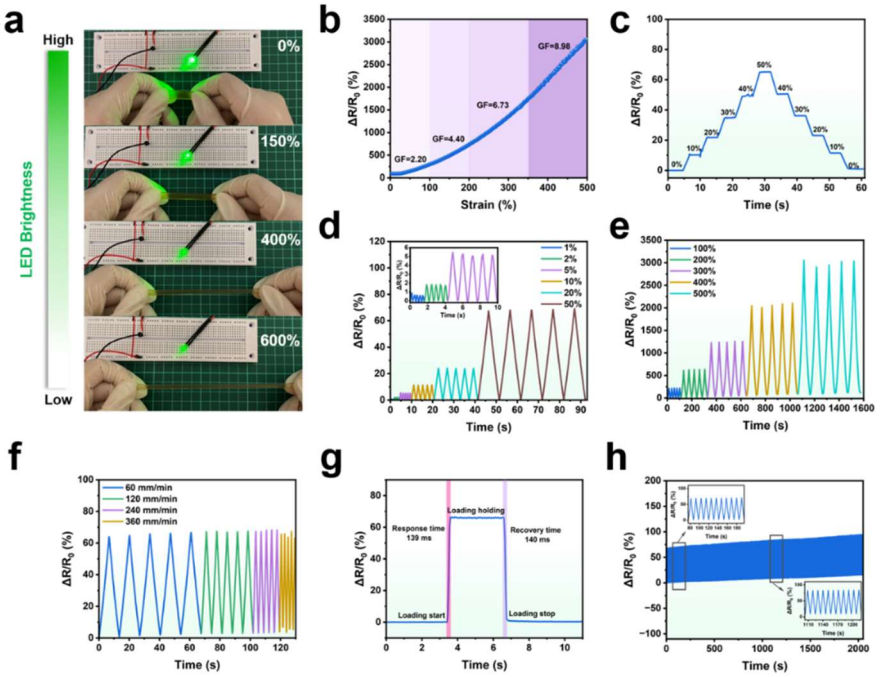


**Figure 2-8.** (a) Images of brightness variation of an LED bulb under different elongations of the hydrogel. (b) GF of LS1.25-$Fe^{3+}$/CNC/P(AM-APBA1.0-AAS) hydrogel within the applied strains. (c) Relative resistance changes of the hydrogel strain sensor during stepwise stretching and releasing. Relative resistance changes of the sensor under different strain levels, (d) for small strain (1-50%) and (e) for large strain (100-500%). (f) Impact of varying tensile speeds on the relative resistance change. (g) Response and recovery time of the hydrogel sensor. (h) Sensing stability of the hydrogel sensor over a period of more than 2000 s (0-50%).

differences in relative resistance changes when the same strain was applied at various stretching speeds (60-360 mm/min). In addition, the hydrogel sensor exhibited response and recovery times of 139 ms and 140 ms, respectively, during the stretching and release processes (**Figure 2-8g**). This impressive response speed is well-suited to meet the demands of practical applications. Except the rapid electromechanical response capability, the fatigue resistance and long-term stability of the hydrogel sensor were also evaluated through approximately 200 cycles of successive tensile testing at a 50% strain over a period of 2000 s. In **Figure 2-8h**, the hydrogel sensor exhibited a stable and consistent electrical signal response with no noticeable deviations, exhibiting excellent response stability, which is attributed to the rich multiple dynamic cross-linked networks in the hydrogel network, ensuring the repeatability and reliability of the sensing signal.

**LS-$Fe^{3+}$/CNC/P(AM-APBA-AAS) strain sensor applied to elderly health monitoring**

Due to extraordinary strain sensitivity and response stability, the LS-$Fe^{3+}$/CNC/P(AM-APBA-AAS) hydrogel can be used as a strain sensor in creating a smart care system for real-time monitoring of the health status of elderly (**Figure 2-9a**). As physical functions decline and functional impairments emerge, the elderly are at risk of experiencing a decline or even loss of abilities such as language and mobility.[57] When the hydrogel sensor was adhered to the volunteer's throat, signals from swallowing and coughing could be easily distinguished (**Figure 2-9a**), which can be potentially utilized for the care of severely ill patients. Furthermore, in **Figure 2-9b**, distinguishable and repeatable electrical signals could be easily obtained when volunteer silently spoke this words, "help", "medicine" and "water". This capability can aid caregivers in promptly identifying the needs of the elderly, including those who have lost their ability to speak. With aging, the physiological structure and functions of the human body undergo changes, including the decrease in muscle strength, joint disorders, loss of neurons,

etc., all of which can restrict the movement functions of the elderly, such as fingers and joints. As shown in **Figure 2-9c**, hydrogel sensors could detect the stretching and bending movements of fingers and wrists. Similarly, it can be well detected the electrical signals resulting from the extension and flexion movements of the elbow and shoulder (**Figure 2-9d**). Therefore, the hydrogel sensor has significant potential applications in assisting the elderly in detecting injuries to fingers, joints, and bones, as well as in the field of rehabilitation exercises. These results demonstrate that LS-$Fe^{3+}$/CNC/P(AM-APBA-AAS) hydrogel sensor was beneficial for real-time monitoring of the health status of the elderly, conveying their needs, thereby aiding them in rehabilitation exercises and enhancing their quality of life.

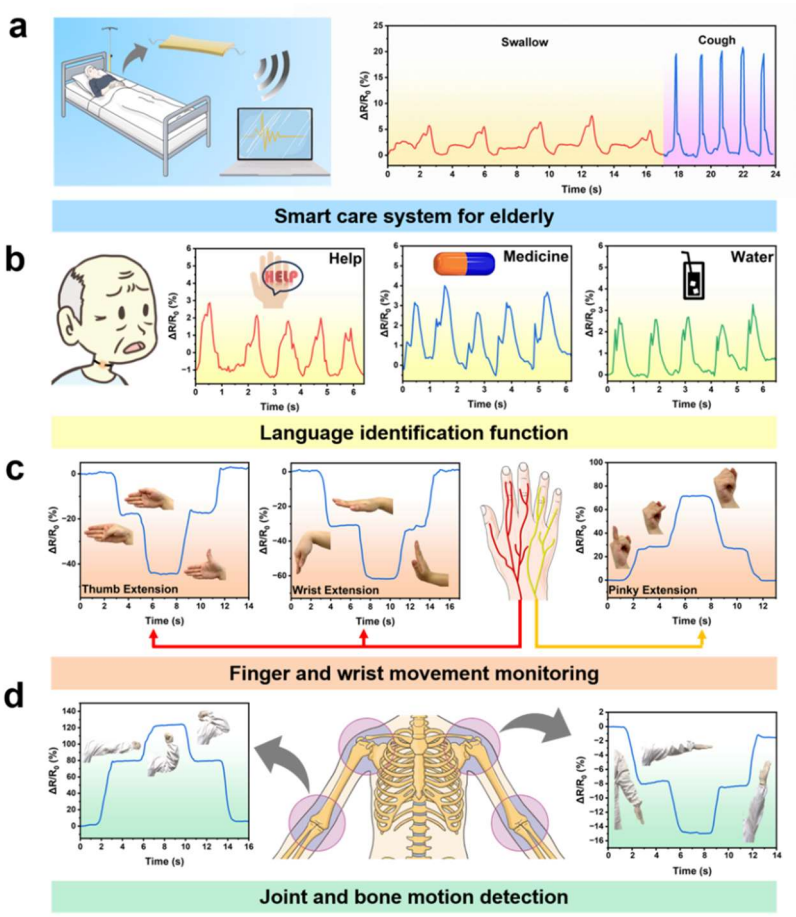


**Figure 2-9.** (a) The electronic sensor based on LS-$Fe^{3+}$/CNC/P(AM-APBA-AAS) hydrogel used for elderly health monitoring (left); and the sensors can monitor and identify swallowing and coughing signals (right). Applications of the hydrogel sensor to (b) language identification, (c) finger and wrist movement monitoring and (d) joint and bone motion detection.

**LS-$Fe^{3+}$/CNC/P(AM-APBA-AAS) strain sensor applied to real-time monitoring of human sleep**

Furthermore, the LS-$Fe^{3+}$/CNC/P(AM-APBA-AAS) strain sensor can accurately identify

and detect subtle human physiological signals, making it a versatile multi-purpose sensor with potential real-life applications. The sleep process was divided into three stages: light sleep, deep sleep, and Rapid Eye Movement (REM) sleep.[53] During this process, two main types of eye movements are involved. One is slow and involves large rolling or swinging eye movements, occurring during deep sleep. The other is rapid, characterized by small and unstable rotational eye movements, which occur during the REM sleep stage.[58] As depicted in **Figure 2-10a**, to enhance comfort and minimize the loss of moisture from the hydrogel, the hydrogel sensor was further assembled into a smart eye mask device for simulating these two types of eye movements during the sleep process. As shown in **Figure 2-10b**, the relative resistance change signals of these two types of eye movements were easily distinguishable, confirming the potential of the hydrogel sensor for monitoring human sleep. Additionally, the hydrogel sensor was attached to the volunteers' throat to simulate the possibility of snoring during the sleep process. As expected, there were significant differences in the electrical signals between snoring and normal breathing. This can assist in monitoring a human's sleep status, as snoring behavior may lead to breathing pauses and potential harm to organs. The results confirmed that due to remarkable sensing performance, the hydrogel exhibited significant potential in practical applications such as healthcare, disease diagnosis, and smart wearable

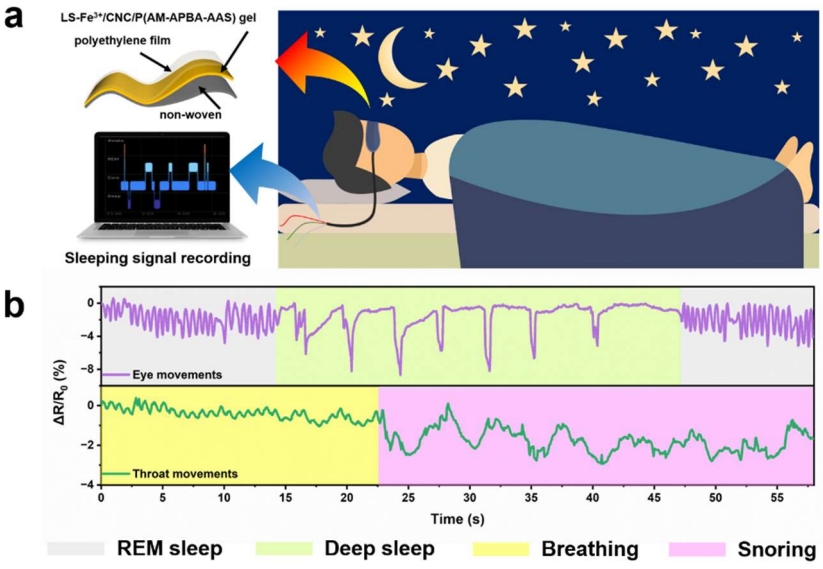


**Figure 2-10.** (a) Schematics illustrating the experimental setup of the simulated sleep monitoring. (b) Relative resistance changes of simulated eye and throat movements during sleep.

devices.

## 2.4 Conclusions

In summary, a multifunctional hydrogel with multiple dynamic cross-linking networks was rapidly prepared at room temperature by using LS-$Fe^{3+}$ dynamic catalytic system to trigger radical self-polymerization strategy. Due to the synergistic interactions of reversible boronic ester bonds, ionic coordination bonds, and hydrogen bonds, the LS-$Fe^{3+}$/CNC/P(AM-APBA-AAS) hydrogel exhibited high stretchability (1170%), skin-like modulus (39.50 kPa), exceptional fatigue resistance, and excellent self-healing properties. At the same time, the catechol groups resulting from dynamic redox reactions between the LS-$Fe^{3+}$ endowed the hydrogel the durable and repeatable self-adhesion properties with various substrates. Furthermore, based on ions conduction, the hydrogel exhibited extraordinary sensitivity (GF up to 8.98 within 500% strain) and rapid response capability (139 ms). Benefiting from these advantages, the hydrogel can be assembled into multifunctional wearable sensors for smart elderly care system, accurately monitoring and identifying the movements of the human body, including fingers, wrists, elbows, shoulders, and even faint physiological signals (sound, swallowing, and coughing). Additionally, this hydrogel wearable sensors can also be assembled into a “smart eye mask” for sleep monitoring, demonstrating a sensitive capability to distinguish rapid eye movement sleep and deep sleep. The author believe that this environmentally friendly, time-efficient, and cost-effective hydrogel holds significant potential for applications in flexible electronics, health monitoring, and disease diagnosis.

## 2.5 References

1. D. Son, J. Kang, O. Vardoulis, Y. Kim, N. Matsuhisa, J. Y. Oh, J. W. F. To, J. Mun, T. Katsumata, Y. Liu, A. F. McGuire, M. Krason, F. Molina-Lopez, J. Ham, U. Kraft, Y. Lee, Y. Yun, J. B. H. Tok and Z. Bao, *Nat. Nanotechnol.*, 2018, **13**, 1057-1065.

2. S. Shi, Y. Si, Z. Li, S. Meng, S. Zhang, H. Wu, C. Zhi, W.-F. Io, Y. Ming, D. Wang, B. Fei, H. Huang, J. Hao and J. Hu, *ACS Nano*, 2023, **17**, 7035-7046.
3. H. Yuk, J. Wu and X. Zhao, *Nat. Rev. Mater.*, 2022, **7**, 935-952.
4. Y. Lee, W. J. Song and J. Y. Sun, *Mater. Today Phys.*, 2020, **15**, 100258.
5. Y. Luo, M. R. Abidian, J.-H. Ahn, D. Akinwande, A. M. Andrews, M. Antonietti, Z. Bao, M. Berggren, C. A. Berkey, C. J. Bettinger, J. Chen, P. Chen, W. Cheng, X. Cheng, S.-J. Choi, A. Chortos, C. Dagdeviren, R. H. Dauskardt, C.-a. Di, M. D. Dickey, X. Duan, A. Facchetti, Z. Fan, Y. Fang, J. Feng, X. Feng, H. Gao, W. Gao, X. Gong, C. F. Guo, X. Guo, M. C. Hartel, Z. He, J. S. Ho, Y. Hu, Q. Huang, Y. Huang, F. Huo, M. M. Hussain, A. Javey, U. Jeong, C. Jiang, X. Jiang, J. Kang, D. Karnaushenko, A. Khademhosseini, D.-H. Kim, I.-D. Kim, D. Kireev, L. Kong, C. Lee, N.-E. Lee, P. S. Lee, T.-W. Lee, F. Li, J. Li, C. Liang, C. T. Lim, Y. Lin, D. J. Lipomi, J. Liu, K. Liu, N. Liu, R. Liu, Y. Liu, Y. Liu, Z. Liu, Z. Liu, X. J. Loh, N. Lu, Z. Lv, S. Magdassi, G. G. Malliaras, N. Matsuhisa, A. Nathan, S. Niu, J. Pan, C. Pang, Q. Pei, H. Peng, D. Qi, H. Ren, J. A. Rogers, A. Rowe, O. G. Schmidt, T. Sekitani, D.-G. Seo, G. Shen, X. Sheng, Q. Shi, T. Someya, Y. Song, E. Stavrinidou, M. Su, X. Sun, K. Takei, X.-M. Tao, B. C. K. Tee, A. V.-Y. Thean, T. Q. Trung, C. Wan, H. Wang, J. Wang, M. Wang, S. Wang, T. Wang, Z. L. Wang, P. S. Weiss, H. Wen, S. Xu, T. Xu, H. Yan, X. Yan, H. Yang, L. Yang, S. Yang, L. Yin, C. Yu, G. Yu, J. Yu, S.-H. Yu, X. Yu, E. Zamburg, H. Zhang, X. Zhang, X. Zhang, X. Zhang, Y. Zhang, Y. Zhang, S. Zhao, X. Zhao, Y. Zheng, Y.-Q. Zheng, Z. Zheng, T. Zhou, B. Zhu, M. Zhu, R. Zhu, Y. Zhu, Y. Zhu, G. Zou and X. Chen, *ACS Nano*, 2023, **17**, 5211-5295.
6. Y. Zhang, Z. Xu, Y. Yuan, C. Liu, M. Zhang, L. Zhang and P. Wan, *Adv. Funct. Mater.*, 2023, **33**, 2300299.
7. Y.-Z. Zhang, K. H. Lee, D. H. Anjum, R. Sougrat, Q. Jiang, H. Kim and H. N. Alshareef, *Sci. Adv.*, **4**, eaat0098.
8. X. Sun, F. Yao and J. Li, *J. Mater. Chem. A*, 2020, **8**, 18605-18623.
9. S. Kim, A. U. Regitsky, J. Song, J. Ilavsky, G. H. McKinley and N. Holten-Andersen, *Nat. Commun.*, 2021, **12**, 667.
10. L. Zhou, Y. Li, J. Xiao, S.-W. Chen, Q. Tu, M.-S. Yuan and J. Wang, *Anal. Chem.*, 2023, **95**, 3811-3820.
11. J. Park, N. Jeon, S. Lee, G. Choe, E. Lee and J. Y. Lee, *Chem. Eng. J.*, 2022, **446**, 137344.
12. H. Xu, Z. Shen and G. Gu, *Sci. China Technol. Sci.*, 2020, **63**, 923-930.
13. D. Hardman, T. George Thuruthel and F. Iida, *NPG Asia Mater.*, 2022, **14**, 11.
14. J. Qu, Q. Yuan, Z. Li, Z. Wang, F. Xu, Q. Fan, M. Zhang, X. Qian, X. Wang, X. Wang and M. Xu, *Nano Energy*, 2023, **111**, 108387.
15. X. Sun, F. Yao, C. Wang, Z. Qin, H. Zhang, Q. Yu, H. Zhang, X. Dong, Y. Wei and J. Li, *Macromol. Rapid Commun.*, 2020, **41**, 2000185.
16. Z. Wang, J. Chen, Y. Cong, H. Zhang, T. Xu, L. Nie and J. Fu, *Chem. Mater.*, 2018, **30**, 8062-8069.
17. T. R. Ray, J. Choi, A. J. Bandodkar, S. Krishnan, P. Gutruf, L. Tian, R. Ghaffari and J. A. Rogers, *Chem. Rev.*, 2019, **119**, 5461-5533.
18. D. Gan, W. Xing, L. Jiang, J. Fang, C. Zhao, F. Ren, L. Fang, K. Wang and X. Lu, *Nat. Commun.*, 2019, **10**, 1487.
19. Z. Jia, Y. Zeng, P. Tang, D. Gan, W. Xing, Y. Hou, K. Wang, C. Xie and X. Lu, *Chem. Mater.*, 2019, **31**, 5625-5632.

20. Q. Wang, X. Pan, C. Lin, X. Ma, S. Cao and Y. Ni, *Chem. Eng. J.*, 2020, **396**, 125341.
21. F. G. Calvo-Flores and J. A. Dobado, *ChemSusChem*, 2010, **3**, 1227-1235.
22. S. V. Patil and D. S. Argyropoulos, *ChemSusChem*, 2017, **10**, 3284-3303.
23. M. Davaritouchaee, W. C. Hiscox, E. Terrell, R. J. Mancini and S. Chen, *Green Chem.*, 2020, **22**, 1182-1197.
24. A. K. Mondal, D. Xu, S. Wu, Q. Zou, W. Lin, F. Huang and Y. Ni, *Int. J. Biol. Macromol.*, 2022, **207**, 48-61.
25. D. Sun, Y. Feng, S. Sun, J. Yu, S. Jia, C. Dang, X. Hao, J. Yang, W. Ren, R. Sun, C. Shao and F. Peng, *Adv. Funct. Mater.*, 2022, **32**, 2201335.
26. Y. Song, L. Niu, P. Ma, X. Li, J. Feng and Z. Liu, *ACS Appl. Mater. Interfaces*, 2023, **15**, 10006-10017.
27. X. Liu, Q. Zhang, F. Jia and G. Gao, *Sci. China Mater.*, 2021, **64**, 3069-3078.
28. T. L. Sun, F. Luo, W. Hong, K. Cui, Y. Huang, H. J. Zhang, D. R. King, T. Kurokawa, T. Nakajima and J. P. Gong, *Macromolecules*, 2017, **50**, 2923-2931.
29. D. L. Taylor and M. in het Panhuis, *Adv. Mater.*, 2016, **28**, 9060-9093.
30. A. Phadke, C. Zhang, B. Arman, C.-C. Hsu, R. A. Mashelkar, A. K. Lele, M. J. Tauber, G. Arya and S. Varghese, *Proceedings of the National Academy of Sciences*, 2012, **109**, 4383-4388.
31. K. Miyamae, M. Nakahata, Y. Takashima and A. Harada, *Angew. Chem. Int. Ed.*, 2015, **54**, 8984-8987.
32. D. C. Tuncaboylu, M. Sari, W. Oppermann and O. Okay, *Macromolecules*, 2011, **44**, 4997-5005.
33. M. C. Roberts, M. C. Hanson, A. P. Massey, E. A. Karren and P. F. Kiser, *Adv. Mater.*, 2007, **19**, 2503-2507.
34. Q. Ling, W. Liu, J. Liu, L. Zhao, Z. Ren and H. Gu, *ACS Appl. Mater. Interfaces*, 2022, **14**, 24741-24754.
35. R. Guo, Q. Su, J. Zhang, A. Dong, C. Lin and J. Zhang, *Biomacromolecules*, 2017, **18**, 1356-1364.
36. X. Yao, S. Zhang, L. Qian, N. Wei, V. Nica, S. Coseri and F. Han, *Adv. Funct. Mater.*, 2022, **32**, 2204565.
37. C. Yang, Y. Zhang, X. Zhang, P. Tang, T. Zheng, R. Ran and G. Li, *Carbohydr. Polym.*, 2023, **320**, 121231.
38. X. Zhao, D. Pei, Y. Yang, K. Xu, J. Yu, Y. Zhang, Q. Zhang, G. He, Y. Zhang, A. Li, Y. Cheng and X. Chen, *Adv. Funct. Mater.*, 2021, **31**, 2009442.
39. L. Zhao, Z. Ren, X. Liu, Q. Ling, Z. Li and H. Gu, *ACS Appl. Mater. Interfaces*, 2021, **13**, 11344-11355.
40. Y. Habibi, L. A. Lucia and O. J. Rojas, *Chem. Rev.*, 2010, **110**, 3479-3500.
41. F. Lin, Z. Wang, Y. Shen, L. Tang, P. Zhang, Y. Wang, Y. Chen, B. Huang and B. Lu, *J. Mater. Chem. A*, 2019, **7**, 26442-26455.
42. X. Le, W. Lu, H. Xiao, L. Wang, C. Ma, J. Zhang, Y. Huang and T. Chen, *ACS Appl. Mater. Interfaces*, 2017, **9**, 9038-9044.
43. K. Xu, K. Shen, J. Yu, Y. Yang, Y. Wei, P. Lin, Q. Zhang, C. Xiao, Y. Zhang and Y. Cheng, *Chem. Mater.*, 2022, **34**, 3311-3322.
44. J. Yang, J.-J. Zhao, F. Xu and R.-C. Sun, *ACS Appl. Mater. Interfaces*, 2013, **5**, 12960-12967.

45. M. H. Lan, X. Guan, D. Y. Zhu, Z. P. Chen, T. Liu and Z. Tang, *ACS Appl. Mater. Interfaces*, 2023, **15**, 19447-19458.
46. C. Shao, L. Meng, M. Wang, C. Cui, B. Wang, C.-R. Han, F. Xu and J. Yang, *ACS Appl. Mater. Interfaces*, 2019, **11**, 5885-5895.
47. P. Du, J. Wang, Y.-I. Hsu and H. Uyama, *ACS Appl. Mater. Interfaces*, 2023, **15**, 23711-23724.
48. H. Zhao, S. Hao, Q. Fu, X. Zhang, L. Meng, F. Xu and J. Yang, *Chem. Mater.*, 2022, **34**, 5258-5272.
49. S. Zong, H. Lv, C. Liu, L. Zhu, J. Duan and J. Jiang, *Chem. Eng. J.*, 2023, **465**, 142831.
50. S. Hao, C. Shao, L. Meng, C. Cui, F. Xu and J. Yang, *ACS Appl. Mater. Interfaces*, 2020, **12**, 56509-56521.
51. T. Li, S. Wang, Y. Huang, H. Zhou, L. Zhang and Z. Wang, *Chem. Eng. J.*, 2023, **472**, 144864.
52. D. Sun, N. Li, J. Rao, S. Jia, Z. Su, X. Hao and F. Peng, *J. Mater. Chem. A*, 2021, **9**, 14381-14391.
53. K. Shen, K. Xu, M. Zhang, J. Yu, Y. Yang, X. Zhao, Q. Zhang, Y. Wu, Y. Zhang and Y. Cheng, *Chem. Eng. J.*, 2023, **451**, 138525.
54. Y. Zhao, F. Wang, J. Liu, D. Gan, B. Lei, J. Shao, W. Wang, Q. Wang and X. Dong, *ACS Appl. Mater. Interfaces*, 2023, **15**, 28664-28674.
55. J. Zhang, J. Zhuang, L. Lei and Y. Hou, *J. Mater. Chem. A*, 2023, **11**, 3546-3555.
56. Y. Li, Y. Jin, W. Zeng, H. Jin, X. Shang and R. Zhou, *ACS Appl. Mater. Interfaces*, 2023, **15**, 35469-35482.
57. S. Tian, Y. Xing, Y. Long, H. Guo, S. Xu, Y. Ma, C. Wen, Q. Li, X. Liu, L. Zhang and J. Yang, *ACS Appl. Mater. Interfaces*, 2022, **14**, 5122-5133.
58. M. Wu, J. Chen, Y. Ma, B. Yan, M. Pan, Q. Peng, W. Wang, L. Han, J. Liu and H. Zeng, *J. Mater. Chem. A*, 2020, **8**, 24718-24733.

# Chapter 3.

# Smart versatile hydrogels tailored by metal-phenolic coordinating carbon and polypyrrole for soft actuation, strain sensing and writing recognition

## 3.1 Introduction

In the last few decades, hydrogels with three-dimensional (3D) network structures have emerged as promising candidate materials in various fields such as electronic skins[1, 2], wearable sensors[3, 4], human-machine interaction systems[5, 6], bioengineering[7], and soft robotics[8] due to their highly tunable physicochemical properties (water content, mechanical, electrical, etc.), excellent flexibility, and good compatibility.[9, 10] Among them, conductive hydrogels and stimuli-responsive smart hydrogels are the two research directions that have developed the fastest and received the most attention. Conductive hydrogels can convert mechanical stimuli into electrical signals and accurately collect them, making them commonly used as flexible strain sensors.[11-13] Stimuli-responsive hydrogels can respond reversibly to external stimuli (temperature, pH, light, magnetic fields, etc.), undergoing changes in morphology, structure, or properties, and are widely used in the development of bio-inspired actuators, drug delivery systems, and soft robots.[14] Despite tremendous progress has been made in both types of hydrogels, it remains challenging to develop multifunctional hydrogels that integrate conductivity for sensing and stimuli-responsive properties in a cost-effective method.[15]

Stimuli-responsive hydrogels, capable of responding to external stimuli and undergoing flexible, complex, and reversible shape deformations, have been extensively developed as actuators to enable the locomotion of soft robots.[16-18] Compared to external stimuli (pH,

magnetic fields, electric fields, etc.), near-infrared light (NIR) possess advantages such as safety, strong penetration, and remote controllability.[19] It can provide non-contact, immediate, precise, and manipulable stimulation for responsive hydrogels.[20] In contemporary study, various photothermal were incorporated into agents into hydrogel matrix to fabricate NIR-responsive actuators, bestowing them with light-responsive behaviors and programmable shape deformations. For instance, Zhang *et al.* incorporated $Fe^{3+}$/tannic acid (TA) complexes as the photothermal conversion agent into thermosensitive hydrogel and designed a novel hydrogel actuator with excellent NIR-triggered driving behavior.[21] Ge *et al*. rapidly prepared a self-healing hydrogel using $Ti_3C_3T_x$ MXene nanosheets as a multifunctional cross-linker. Ma *et al*. combined amino-functionalized MXene-encapsulated liquid metal nanodroplets with a hydrogel network to prepare a self-sensing hydrogel actuator that integrates conductivity and NIR light responsiveness.[22] These nanosheets not only endowed the hydrogel with excellent mechanical properties and self-healing capability but also enabled the hydrogel to exhibit repeatable thermal sensing performance under NIR irradiation.[23] These photothermal agents including MXene nanosheets,[19] carbon nanotubes,[24, 25] graphene/graphene oxide,[26, 27] gold nanorods,[28] conductive polymers,[29, 30] metal oxides nanoparticles,[20] and metal-phenolic coordination complexes,[21] etc. Particularly, compared to other photothermal agents, carbon nanotubes (CNT) and other carbon-based materials exhibit heat generation across a wider range of spectral wavelengths, making CNT a particularly promising choice for photothermal conversion.[31] However, it is critically noted that hydrogels exhibiting photothermal effects often rely on the incorporation of thermosensitive monomers or bilayer configurations, leading to challenges like limited functionality, slow response times, and weak interfacial bonding. Therefore, it is necessary to identify a feasible strategy to develop a photothermally efficient, multifunctional hydrogel actuator using a simple method to meet the needs of practical applications.

When CNT are directly dispersed in a hydrogel matrix, their insufficient interactions can result in aggregation and phase separation.[32] This compromises both mechanical strength and conductivity, falling short of the rapid response and conductivity required for strain sensors. Therefore, it is necessary to consider incorporating other conductive agents to enhance the effective interaction between CNT and the hydrogel matrix. Polypyrrole (PPy), a commonly utilized conductive polymer, is frequently chosen for flexible electronic sensors due to its wide conductivity range, considerable mechanical strength and flexibility, as well as excellent chemical stability.[11, 33] While ensuring mechanical performance, PPy should be one of the optimal choices to impart both photothermal and conductive properties to the hydrogel when combined with CNT.[34] However, directly incorporating PPy into a hydrogel matrix to produce conductive hydrogels often results in poor dispersion and phase separation between the hydrogel and PPy.[35] This leads to compromised mechanical strength of the hydrogel, which in turn limits the sensitivity and cyclic stability of the hydrogel sensors. To address this issue, Lu *et al*. employed the natural polymer chitosan framework as a molecular template to guide the in-situ polymerization of PPy within the hydrogel, leading to the formation of highly interconnected conductive pathways.[36] Meanwhile, Zhang *et al.* utilized sodium alginate as the template for synthesizing PPy nanoparticles within the hydrogel matrix, establishing a 3D conductive network and achieving a strain sensor with excellent sensing capabilities.[37] Drawing inspiration from the aforementioned studies, the author innovatively selected the natural polymer carboxymethylcellulose (CMC) and $Fe^{3+}$-tannic acid-coated CNT as template for the in-situ polymerization of PPy within the hydrogel. This approach capitalized on the synergistic interaction between PPy and carbon nanotubes, granting the hydrogel outstanding photothermal properties, thereby achieving dual advantages with a single method.

Inspired by the aligned structures of natural bio-tissues, the author proposed a versatile conductive composite hydrogel with integrated NIR light-driven deformation and strain sensing

behaviors by combining a synthetic process of incorporation of metal-organic coordination bond into carbon nanotubes with a post in-situ polymerization. Specifically, the $Fe^{3+}$-tannic acid (TA) complex- modified single-walled nanotubes (Fe-TA@SWNT) was introduced into a hydrogel network composed of CMC, copolymer of acrylic acid (AA) and [2-(methacryloyloxy) ethyl]dimethyl-(3-sulfopropyl) ammonium hydroxide (SBMA) (P(AA-SBMA)), followed by in-situ polymerization of PPy in the hydrogel network using Fe-TA@SWNT, CMC, and P(AA-SBMA) as the skeletons. Through the synergistic interactions of chemical cross-linking bonds and various dynamic bonds (hydrogen bonds, ion coordination bonds, cation-π interactions, and electrostatic interactions), the prepared hydrogel exhibited significant stretchability (1283.42% elongation), toughness (1.11 $MJ/m^3$), self-recovery, and repeatable self-adhesive properties. Moreover, the NIR photothermal effect exhibited by Fe-TA@SWNT and PPy, in conjunction with the interconnected conductive channels formed, enabled the integration of sensing and actuation functionalities within the hydrogel. Under NIR light irradiation, the hydrogel exhibited macroscopic shape deformation due to anisotropic volume shrinkage. The fabricated hydrogel strain sensor also demonstrated exceptional strain sensitivity and reliable signal accuracy, suitable for precise monitoring of human joint movements (e.g., fingers, throat, elbows, and knees), facial expressions, and heartbeats. This work paves a new path for the effective development of hydrogels for wearable electronic devices, remote actuators, and biomimetic soft robots.

## 3.2 Materials and methods

### Materials

The SBMA, methylene-bis-acrylamide (MBAA) and pyrrole (Py) was obtained from Tokyo Chemical Industry Co., Ltd. (TCI, Tokyo, Japan). 2,2'-azobis(2-methylpropionamide) dihydrochloride (AIBA), TA, iron chloride hexahydrate ($FeCl_3 \cdot 6H_2O$) and sodium hydroxide

(NaOH) solution were purchased from Wako Pure Chemical Industries, Ltd. (Wako, Osaka, Japan). Carboxymethylcellulose sodium salt (CMC) and SWNT was provided by Sigma Co., Ltd. (Aldrich, USA). AA was purchased from Nacalai Tesque, Inc. (Kyoto, Japan). All chemicals were utilized without additional purification. Deionized (DI) water was used in all experiments unless specified otherwise.

**Preparation of Fe-TA@SWNT**

Fe-TA@SWNT was synthesized according to a previous report.[38] The synthetic procedure is shown in **Scheme 3-1**. In brief, SWNT were added to DI water in a certain amount, then TA and $FeCl_3 \cdot 6H_2O$ were added in a ratio of 1:10:1 (SWNT/TA/$FeCl_3 \cdot 6H_2O$) by weight. And the mixed solution was stirred vigorously at room temperature for 30 min. Subsequently the pH of the solution was adjusted to a range of 7-8 using 0.5M solution of NaOH. Finally, Fe-TA@SWNT was obtained as a black solid after tip sonication, centrifugation, water washing, and drying.

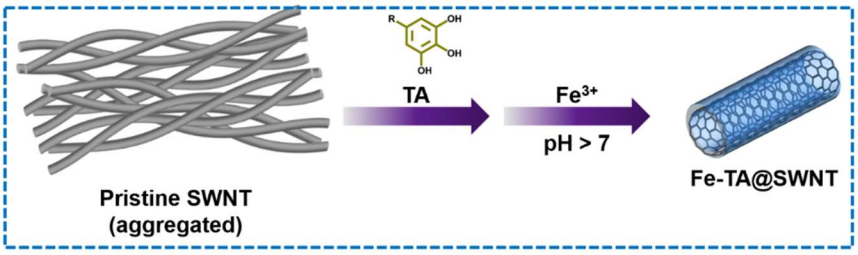


**Scheme 3-1.** The synthetic schematic of Fe-TA@SWNT.

**Fabrication of P(AA-SBMA)/CMC/Fe-TA@SWNT composite hydrogels**

Typically, a certain amount of AA, SBMA, AIBA, MBAA, Fe-TA@SWNT, $FeCl_3.6H_2O$ and CMC suspension (4 wt%) were dissolved in water. The uniformly dispersed suspension was formed after ultrasonic treatment and incubation at 4 °C for 30 min, then injected into homemade glass molds. Next, polymerization was performed at 50 °C for 24 h to obtain the Fe-TA@SWNT based hydrogel network. The collected hydrogels were continuously flushed with water to remove the excessive ions and unreacted monomers. The detailed compositions of the P(AA-SBMA)/CMC/Fe-TA@SWNT hydrogels were summarized in **Table 3-1**.

**Table 3-1.** Varied content of Fe-TA@SWNT in the P(AA-SBMA)/CMC/Fe-TA@SWNT hydrogels.

| Samples | AA (g) | SBMA (g) | CMC (4 wt% solution) (g) | Fe-TA@SWNT (mg) |
|---|---|---|---|---|
| Fe-TA@SWNT0 | 2.0 | 0.5 | 2.5 | 0 |
| Fe-TA@SWNT10 | | | | 10 |
| Fe-TA@SWNT20 | | | | 20 |
| Fe-TA@SWNT30 | | | | 30 |

*All samples were fabricated using 20 mg AIBA, 5 mg MBAA, 3 mL DI water, 20 mg $FeCl_3 \cdot 6H_2O$.

**Fabrication of P(AA-SBMA)/CMC/Fe-TA@SWNT/PPy composite hydrogels**

The PPy composite hydrogels were prepared by the in-situ polymerization on the basis of previous report.[36] The as-prepared P(AA-SBMA)/CMC/Fe-TA@SWNT hydrogels were immersed into a certain amount of pure Py monomer for 24 h under ambient conditions, then stored in a sealed container at 4 °C until the Py monomers had permeated into the P(AA-SBMA)/CMC/Fe-TA@SWNT hydrogels. Subsequently, the hydrogels were immersed in an aqueous solution of $FeCl_3$ (0.5 mol/L) after rinsed off the Py adhered to the surface of the gel, then stored at 4 °C for the corresponding duration to allow Py to polymerize into PPy. The detailed ratios of different Py contents and oxidative polymerization time used for the hydrogels were summarized in in **Table 3-2** and **Table 3-3**.

**Table 3-2.** Varied Py/water volume ratio in the P(AA-SBMA)/CMC/Fe-TA@SWNT/PPy hydrogels

| Samples | AA (g) | SBMA (g) | CMC (4 wt% solution) (g) | Py/water (v/v%) |
|---|---|---|---|---|
| PPy10 | 2.0 | 0.5 | 2.5 | 10 |
| PPy20 | | | | 20 |
| PPy30 | | | | 30 |
| PPy40 | | | | 40 |

*All samples were fabricated using 20 mg AIBA, 5 mg MBAA, 3 mL DI water, 20 mg $FeCl_3 \cdot 6H_2O$ and 20 mg Fe-TA@SWNT. The soaking time in $FeCl_3$ aqueous solution (0.5 mol/L) was 12 h.

**Table 3-3.** Varied soaking time of the P(AA-SBMA)/CMC/Fe-TA@SWNT/PPy hydrogels in $FeCl_3$ aqueous solution (0.5 mol/L).

| Samples | AA (g) | SBMA (g) | CMC (4 wt% solution) (g) | Soaking time in $FeCl_3$ aqueous solution (h) |
|---|---|---|---|---|
| 0 h | 2.0 | 0.5 | 2.5 | 0 |
| 6 h | | | | 6 |
| 12 h | | | | 12 |
| 24 h | | | | 24 |

*All samples were fabricated using 20 mg AIBA, 5 mg MBAA, 3 mL DI water, 20 mg $FeCl_3 \cdot 6H_2O$, 20 mg Fe-TA@SWNT and 20 v/v% of Py to water (step two).

**General characterization**

The morphologies of SWNT and Fe-TA@SWNT were obtained by using transmission

electron microscopy (TEM, Hitachi, H-7650) at an acceleration voltage of 100 kV. X-ray diffraction (XRD, Rigaku Corporation, Tokyo, Japan), Raman spectroscope (Raman, Horiba Scientific LabRAM HR evolution, laser wavelength = 514 nm) and X-ray photoelectron spectroscopy (XPS, ThermoFischer ESCALAB Xi+, $E$ = 1486.6 eV, USA) were applied to confirm the chemical compositions and structures of the SWNT and Fe-TA@SWNT. The cross section the fractured freeze-dried hydrogels was analyzed by using a scanning electron microscopy (SEM, Hitachi SU3500) with accelerating voltage of 10 kV. Before morphological observation, the freeze-dried hydrogels were immersed in liquid nitrogen for 3 min to get the cross section.

**Mechanical tests**

All mechanical properties of gel sample were tested by a universal material testing machine (Shimadzu AGS-X, Shimadzu Corporation, Japan) with a 10 N load cell on strip-shaped hydrogel samples at a constant stretching rate of 100 mm/min. The elastic modulus was calculated from the slope of the initial linear region of the stress-strain curves (at 5-15% strain) and the toughness was estimated from the area under the stress-strain curves up to the fracture point. The loading-unloading tensile tests were conducted at a consistent deformation rate of 100 mm/min without waiting intervals. The dissipated energy was recorded from the area which was enclosed by the cyclic loading-unloading curves. Similarly, the ratio of energy dissipated after each cycle to the initial cycle was defined as dissipating ratio[39]. The gel samples were investigated viscoelastic behaviors using rheological tests by Haake Rheostress 6000 (Thermo Fisher Scientific). The angular frequency was swept from 1 to 100 rad/s at a fixed strain of 1%, and the strain amplitude was swept from 0.1 to 1000% at a fixed oscillation frequency of 1.0 Hz under room temperature. The step-strain measurement was conducted by shifting the amplitude oscillatory strains from a small strain (1.0%) to subsequent large strains

(300%) with 100 s for every strain interval at a constant oscillation frequency (1.0 Hz).

**Adhesion tests**

The P(AA-SBMA)/CMC/Fe-TA@SWNT/PPy composite hydrogel was applied onto the surface of diverse substrates of metal, paper, rubber, silicone, ceramic, porcine skin, wood, glass, plastic and polytetrafluoroethylene (PTFE) to measure the adhesive strengths by typical lap-shear tests between two same substrates at a constant loading rate of 30 mm/min. The adhesion strength was determined by dividing the maximum force by the overlapping contact area.[40]

**Swelling tests**

The swelling capability of the as-prepared gels was tested by the weighing method in an amount of DI water at ambient temperature until reaching swelling equilibrium state. The equilibrium swelling ratio (*SR)* was denoted as:

$$SR = \frac{W_s - W_0}{W_0} \times 100\% \quad (3.1)$$

where $W_s$ and $W_0$ are the weights of the swollen hydrogels and the pristine dried hydrogels, respectively.

**Photothermal effect of the prepared hydrogels**

To evaluate the NIR laser-induced photo response, the hydrogel specimens were irradiated from a distance of 15 cm using a NIR laser (808 nm, 1.5 W/cm$^2$). The real-time temperature variation of the hydrogel was collected through an infrared thermographic camera (FLIR, USA) and a TASI-612C digital thermometer (TASI, China). The repeated irradiation was conducted to evaluate the reversible photothermal effect of the hydrogels. The hydrogels were illuminated by NIR laser for 50 s, followed by turning off the laser to allow the temperature of this gel to decline to room temperature. This cycle was repeated for five times, with real-time temperature record throughout the process.

**NIR triggered deswelling ratio tests**

Briefly, the P(AA-SBMA)/CMC/Fe-TA@SWNT/PPy hydrogels at swelling equilibrium were weighed as $W_1$ after removing the excessive moisture. Then the hydrogels were irradiated by NIR laser for 10 s and weighed again after wiped off the surface water. The weight tests were conducted every 10 s for up to 60 s, and the weight was recorded as $W_t$ at the corresponding time. Consequently, the following equation was used to record the deswelling ratio (*DSR*) of the hydrogels:

$$DSR = \frac{W_1 - W_t}{W_1} \times 100\% \tag{3.2}$$

**NIR triggered actuation of hydrogels**

One end of the rectangular hydrogel (3 cm × 5 mm × 1 mm ) was fixed, and then irradiated continuously with an 808 nm laser at a distance of 15 cm. During this process, the bending behavior of the hydrogel was recorded with a digital camera, and the bending angle at corresponding time points was measured.

**Electromechanical properties of the hydrogel**

The relative resistance variation of hydrogel sensors when subjected to different strains and the corresponding human physiological movements was real time measured by TH2830 digital inductance, capacitance, and resistance (LCR) meter (Changzhou Tonghui Electronic Co. Ltd., China). Therefore, the relative resistance change was computed as the following formula[41]:

$$\Delta R/R_0 = \frac{R - R_0}{R_0} \times 100\% \tag{3.3}$$

where $R$ and $R_0$ represented the real-time resistance and the resistance without any deformation, respectively. Additionally, to reflect the electrical sensitivity, a gauge factor (GF) which was calculated via the following equation:

$$GF = \frac{R - R_0}{R_0 \varepsilon} \tag{3.4}$$

where $\varepsilon$ is the stretching strain.

The above-mentioned electrical experiments were conducted in accordance with the guideline established by Osaka University, Osaka, Japan. Moreover, the author complied with all relevant ethical regulations and obtained informed consent from all volunteers.

## 3.3 Results and Discussion

### Preparation strategy of Fe-TA@SWNT and the hydrogels

In a typical experiment, the SWNT were modified with iron/tannic acid complex (Fe-TA) to enable it to be readily dispersed in aqueous solution due to the hydrophilic functional groups of TA. Briefly, the aggregated SWNT were added to DI water, and then the TA and $Fe^{3+}$ were added to the solution for chelation. Finally, as the pH of the solution increased, the Fe-TA coordination units were adsorbed onto the surface of SWNT through metal-organic coordination interactions. In this process, the tris-TA complex of $Fe^{3+}$ was formed, leading to the generation of metal-phenolic compounds on the surface of SWNT through π-π interactions.[38] The TEM was used to confirm the surface morphologies of SWNT after the Fe-TA coordination reaction, and the Fe-TA@SWNT showed a rougher surface and thickened walls, indicating the Fe-TA coordination units was coated on the outer surface of SWNT effectively (**Figure 3-1b**). To characterize the structural information about Fe-TA@SWNT, X-ray diffraction (XRD) patterns was conducted. As shown in **Figure 3-1c**, compared to SWNT, the coating of Fe-TA coordination units in Fe-TA@SWNT reduced the intensity of characteristic peaks at 25.1° and 43.9° related to the graphite layer of SWNT, but there was no shift in peak positions, implying that the typical structure of SWNT was maintained.[42] Raman spectra of the structural changes among SWNT and Fe-TA@SWNT were collected to coordination of Fe-TA on the SWNT, as shown in **Figure 3-1d**. The peak around 597 $cm^{-1}$ was assigned to the chelated $Fe^{3+}$ by the phenolic oxygen atoms of catechol.[43] The coordination of

Fe-TA on the SWNT was further confirmed by XPS spectra. From **Figure 3-1e**, the XPS spectra showed that SWNT was composed of C and O elements with binding energies of 284.8 and 533.1 eV attributed to C 1s and O 1s, respectively. For the Fe-TA@SWNT, in addition to C and O, the full-scan XPS spectra appeared distinct Fe 2p peaks at 711.3 eV and the amount of Fe reached 1.23%. Moreover, the C/O ratios of SWNT and Fe-TA@SWNT are 10.16 and 1.48, respectively, confirming the coating of Fe-TA chelate layer on the surface of SWNT.[44] Furthermore, the detailed analysis of the C 1s peaks of SWNT and Fe-TA@SWNT was performed (**Figure 3-1f-g**). Compared with pristine SWNT, the abundance of oxygen functional groups (C−O, C=O, and O−C=O) exhibited an obvious rise. This further validated that the successful coating of Fe-TA coordination compounds on SWNT.[42, 45]

The synthesis process of the P(AA-SBMA)/CMC/Fe-TA@SWNT/PPy composite hydrogel was produced by a three-step procedure, as shown in **Figure 3-1a**. First, the P(AA-SBMA)/CMC/Fe-TA@SWNT hydrogels were formed through the one-pot free radical copolymerization method. The physical interactions, including ionic coordination bonding, hydrogen bonding and electrostatic bonding between P(AA-SBMA) polymer chains, as well as chemical cross-linking, supported the formation of the hydrogel network. Second, the hydrogels were swollen to adsorb and disperse Py monomers homogeneously in the hydrogel matrix. In this procession, due to noncovalent interactions, Py monomers were immobilized on the molecular chains of P(AA-SBMA), CMC and Fe-TA@SWNT. Finally, the Py-absorbed P(AA-SBMA)/CMC/Fe-TA@SWNT hydrogels were immersed in a $FeCl_3$ solution, inducing the in-situ polymerization of Py monomers into PPy. At this stage, PPy was formed on the surface of the molecular chains in the hydrogel, which strengthened the hydrogen bonding in the hydrogel system. Meanwhile, the π site on the PPy ring was able to engage in strong cation-π interactions with $Fe^{3+}$ and the positively charged $-R_3N^+$ groups of polymer chain.[46-48] Furthermore, the ion coordination in the hydrogel was also strengthened. This imparted excellent mechanical

properties to the hydrogel.

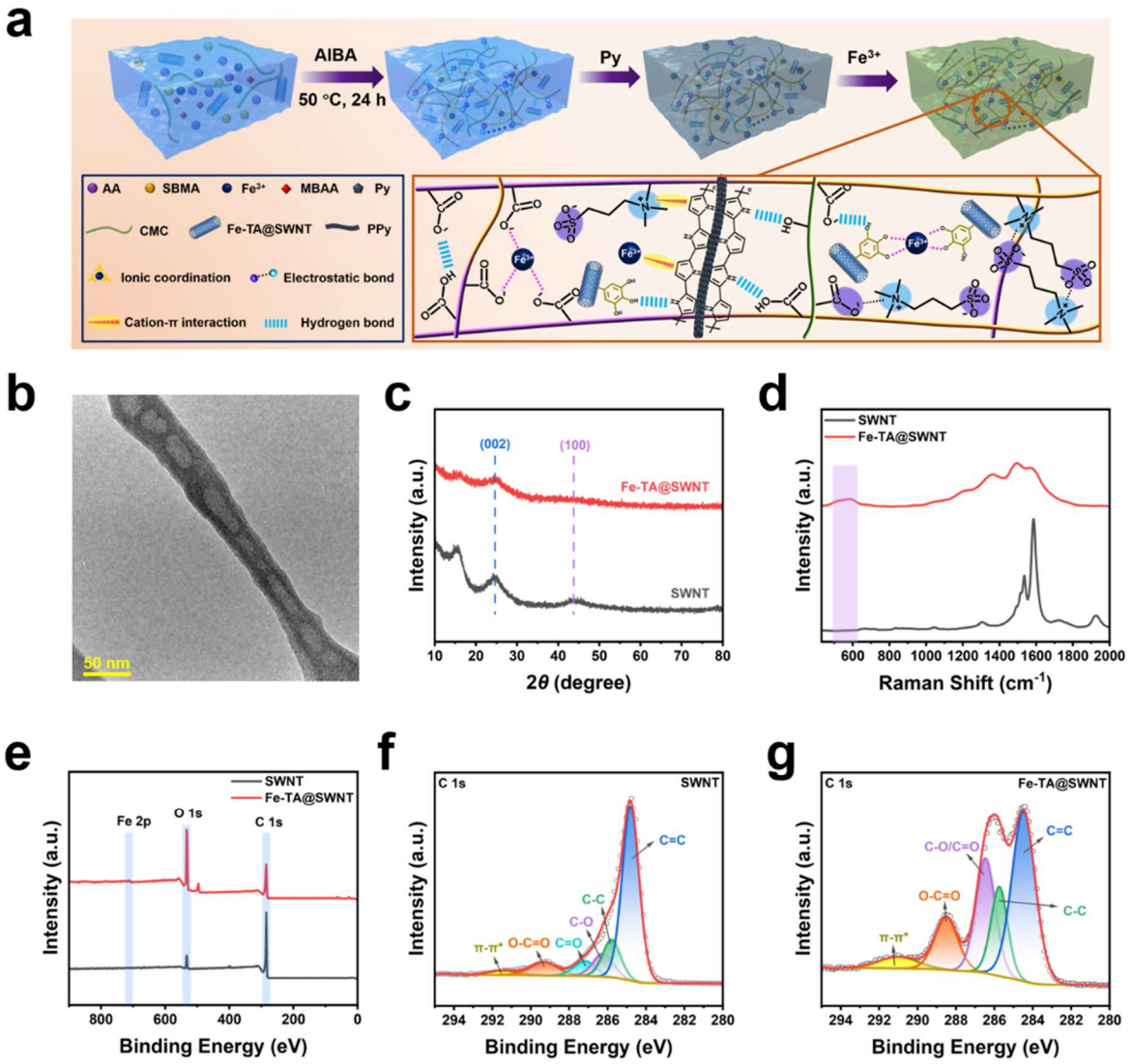


**Figure 3-1.** (a) Designing strategy for P(AA-SBMA)/CMC/Fe-TA@SWNT/PPy hydrogels. (b) TEM images of Fe-TA@SWNT. (c) XRD patterns, (d) Raman spectra, (e) XPS spectra of SWNT and Fe-TA@SWNT. C 1s spectra of (f) SWNT and (g) Fe-TA@SWNT.

### Mechanical and viscoelastic properties

Excellent mechanical properties determine the reliability of conductive hydrogel sensors, and the mechanical performance of hydrogels is largely dependent on their composition and the proportion of components.[49] In **Figures 3-2a** and **3-2b**, the effect of additions of Py on the mechanical stretchability was measured through uniaxial tensile experiment. With the increase

in Py content, the fracture stress and elastic modulus of the hydrogel increased from 144.30 kPa and 14.61 kPa to 231.96 kPa and 78.77 kPa, respectively. The toughness first enhanced with the increase of Py content, but began to decline after the maximum was reached. However, the tensile strain gradually decreased, mainly attributed to the inherent molecular rigidity resulting from the extended π-conjugation of PPy chains and the highly entangled chain structure.[50] The **Figure 3-2c** shows typical stress-strain curves of P(AA-SBMA)/CMC/Fe-TA@SWNT/PPy hydrogels at various oxidation times. The tensile strength increased from 134.98 kPa before oxidation to 152.60 kPa (6 h oxidation), 212.88 kPa (12 h) and 271.58 kPa (24 h), while the elastic modulus increased from 20.80 kPa before oxidation to 68.72 kPa (24 h) (**Figure 3-2d**). Conversely, compared to before oxidation, when the oxidation time reached 6 h, the tensile strain of the hydrogel increased from 979.09% to 1477.59%. As the oxidation time continued to increase, the tensile strain decreased to 1283.42% (12 h) and 831.26% (24 h). The above results indicated that the tensile properties of hydrogels could be controllable by adjusting the Py content and oxidation times. Notably, the P(AA-SBMA)/CMC/Fe-TA@SWNT/PPy hydrogel exhibited optimal tensile properties when the Py/water volume ratio was 20% and the oxidation time was 12 h, with a break strain of 1283.42% and strength of 212.88 kPa, and both values approached the maximum compared to other samples. The presence of well-dispersed Fe-TA@SWNT was also crucial to improving the mechanical performance of the hydrogels due to the incorporation of Fe-TA@SWNT nanomaterials and the interaction between the Fe-TA coordination compounds and the polymer network.

The elasticity and restoration of the P(AA-SBMA)/CMC/Fe-TA@SWNT/PPy hydrogel was characterized by loading-unloading tests. As shown in **Figure 3-2e**, the hydrogel exhibited a significant hysteresis behavior that as the strain increased from 100-1000%, the area of the hysteresis loop expanded, indicating increased energy dissipation during deformation. In addition, the loading-unloading curves of 8 successive cyclic tensile at the constant strain of

500 % were determined to further evaluate the elasticity behavior (**Figure 3-2f**). One can note that all the curves displayed significant hysteresis loops, implying that the P(AA-SBMA)/CMC/Fe-TA@SWNT/PPy gel effectively dissipated energy during cyclic testing, thus imparting exceptional toughness to the hydrogel networks.

Moreover, the author assessed the viscoelastic behavior of the hydrogels via oscillatory rheological tests at 25 °C. **Figure 3-2g** shows that all hydrogels exhibited the typical elastic solid-like behavior in the whole frequency sweeping range because storage modulus ($G'$) were invariably larger than loss modulus ($G''$).[51] In addition, both $G'$ and $G''$ consistently higher with incorporation of Fe-TA@SWNT and PPy, and slightly increased with increasing oscillation frequency. In particular, the P(AA-SBMA)/CMC/Fe-TA@SWNT/PPy gel exhibited a significantly higher elastic modulus than pure P(AA-SBMA)/CMC, indicating the presence of interactions between the rigid Fe-TA@SWNT, PPy and polymeric chains.[52] For the strain amplitude sweep (0.1-1000%) displayed in **Figure 3-2h**, the $G'$ of both gels presented a slight decrease with increasing strain, which may be attributed to the disruption of multiple reversible crosslinks at the CMC, Fe-TA@SWNT and PPy interface and P(AA-SBMA) matrix under high shear strain.[53] Notably, compared to the other two gels, the P(AA-SBMA)/CMC/Fe-TA@SWNT/PPy hydrogel exhibited a more significant decrease in $G'$ and $G''$ with increasing strain, indicating the dissociation of its internally rich non-covalent network. The step-strain measurement was further used to prove the self-recovering behavior of P(AA-SBMA)/CMC/Fe-TA@SWNT/PPy hydrogel. As depicted in **Figure 3-2i**, the hydrogel was cyclically subjected to 1% strain for 100 s followed by 300% strain for 100 s in an alternating manner at a fixed frequency of 1.0 Hz. It's clearly observed that the $G'$ value notably exceeded $G''$ under a low strain of 1%, indicating the stability of the hydrogel network. However, upon increasing the dynamic strain to 300%, $G'$ sharply decreased from 35.20 kPa to 0.71 kPa, falling below $G''$ (1.31 kPa), indicating collapse of the hydrogel network. And when upon reverting the

strain to 1%, both $G'$ and $G''$ quickly recovered to their primary values, demonstrating the rapid reforming of the structure.[54] This behavior can be repeated over multiple cycles without significant modulus decrease, further illustrating the favorable self- recoverability of the hydrogel.

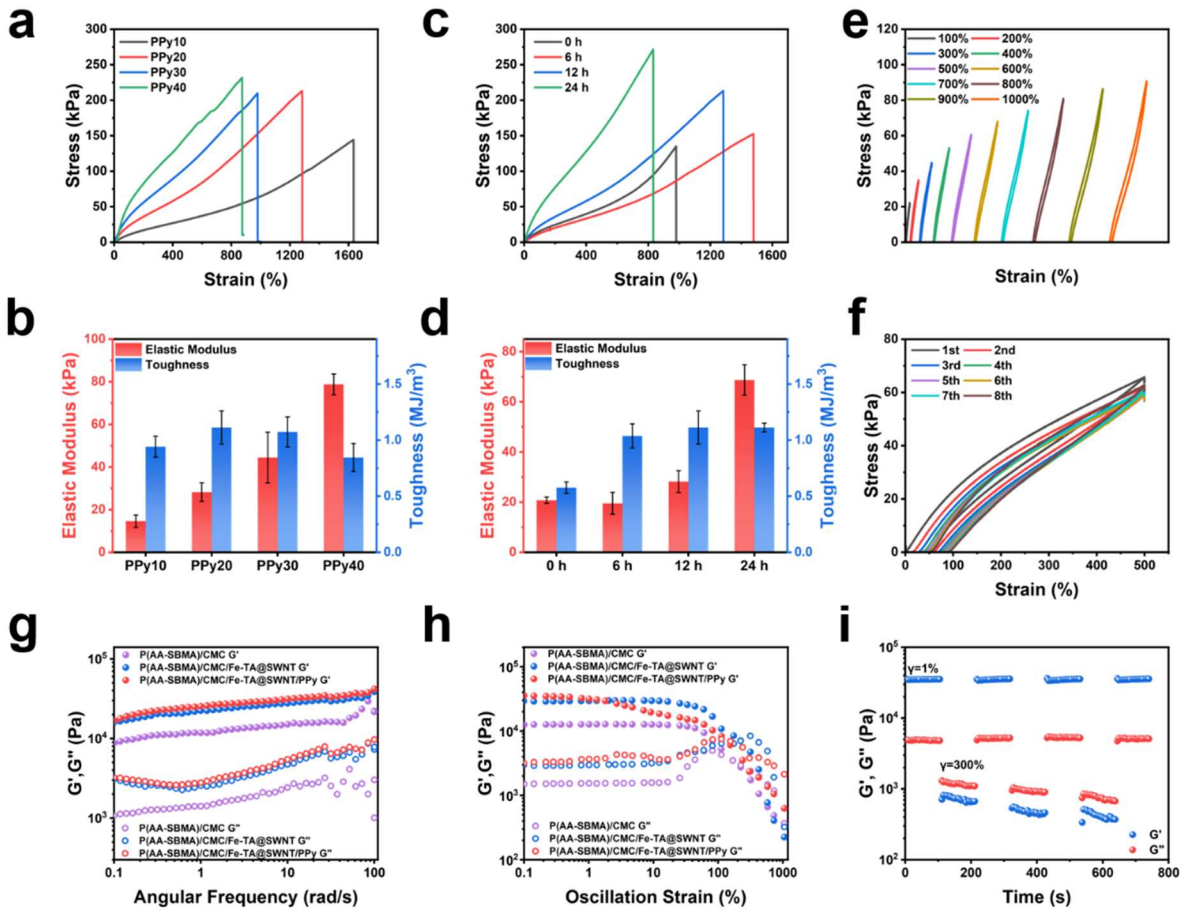


**Figure 3-2.** (a, b) Tensile stress-strain curves of P(AA-SBMA)/CMC/Fe-TA@SWNT/PPy hydrogels with different additions of Py and the corresponding calculated elastic modulus and toughness. (c, d) Tensile stress-strain curves of hydrogels with different oxidation time and the corresponding calculated elastic modulus and toughness. (e) Successive loading–unloading curves under the strain from 100 to 1000%. (f) Cyclic curves under 500% strain for 8 cycles. (g, h) Rheological behavior at varying angular frequencies and the dynamic shear scanning of hydrogels (i) $G'$ and $G''$ of P(AA-SBMA)/CMC/Fe-TA@SWNT/PPy hydrogel during three cycles between 1% and 300% strain.

**Adhesive performance**

For wearable sensors based on hydrogels, adhesive functional characteristics is crucial for establishing effective interfacial connections with substrates and providing reliable signals.[55] From **Figure 3-3a**, it can be observed that the hydrogels can directly adhere to a variety of various hydrophilic and hydrophobic substrates, such as plastic, glass, metal, wood, paper, rubber, ceramic, PTFE, silicone and porcine skin. Thus, the lap shear test was conducted to quantify the adhesion strength by assembling with hydrogels sandwiched between a pair of similar substrates (**Figure 3-3b**). According to **Figure 3-3c**, the maximum adhesive strengths at the interface of wood, rubber, glass, porcine skin, metal and PTFE were 21.8, 19.1, 14.0, 23.8, 14.6 and 10.4 kPa, respectively. Compared to other substrates, the hydrogel exhibited the highest adhesive strength with porcine skin, primarily due to the presence of catechol groups carried by tannic acid in the hydrogel.[56] The dependable adhesion of the P(AA-SBMA)/CMC/Fe-TA@SWNT/PPy hydrogel also demonstrated outstanding reusability and stability. In **Figure 3-3d**, the adhesion strength reduced to more than 30% of the original value after 5 times successive peeling-adhesion on different substrates, and the decrease in adhesion strength may be attributed to surface damage and contamination caused by dirt. This exceptional adhesion of gels to substrates could be attributed to the synergy effect

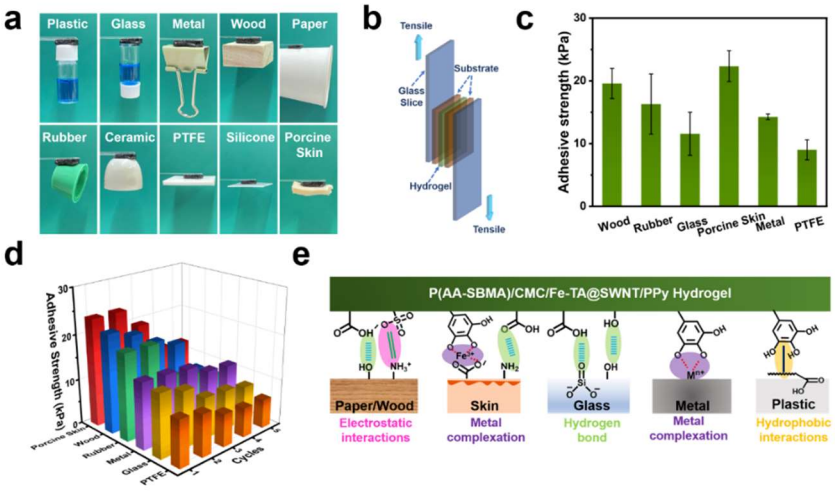


**Figure 3-3.** (a) Adhesive exhibitions of the hydrogel to various substrates. (b) Schematic diagram of the lap shear tests. (c) Lap-shear adhesion strength of the hydrogel to different substrates. (d) Consecutive adherence and separation cycles of the hydrogel to various substrates. (e) Potential adhesive interactions between the gel and the substrate.

of the amphoteric ion, carboxyl and catechol groups within the hydrogel matrix to different contacting interfaces (**Figure 3-3e**).

**Photothermal effect and actuation behavior**

The synergistic effect between Fe-TA coordination compounds modified SWNT and PPy not only provide electronic transport pathways for the hydrogel but also imparts excellent photothermal conversion capability, enabling rapid absorption of NIR light and efficient conversion into heat energy. **Figure 3-4a** illustrates the surface temperature variation over time under near-infrared light (808 nm) irradiation for P(AA-SBMA)/CMC, P(AA-SBMA)/CMC/Fe-TA@SWNT, and P(AA-SBMA)/CMC/Fe-TA@SWNT/PPy hydrogels. It is evident that the surface temperature of P(AA-SBMA)/CMC showed no significant change. By contrast, the surface temperature of the P(AA-SBMA)/CMC/Fe-TA@SWNT/PPy hydrogel increased from 20 °C to 81.1 °C within 60 s, significantly higher

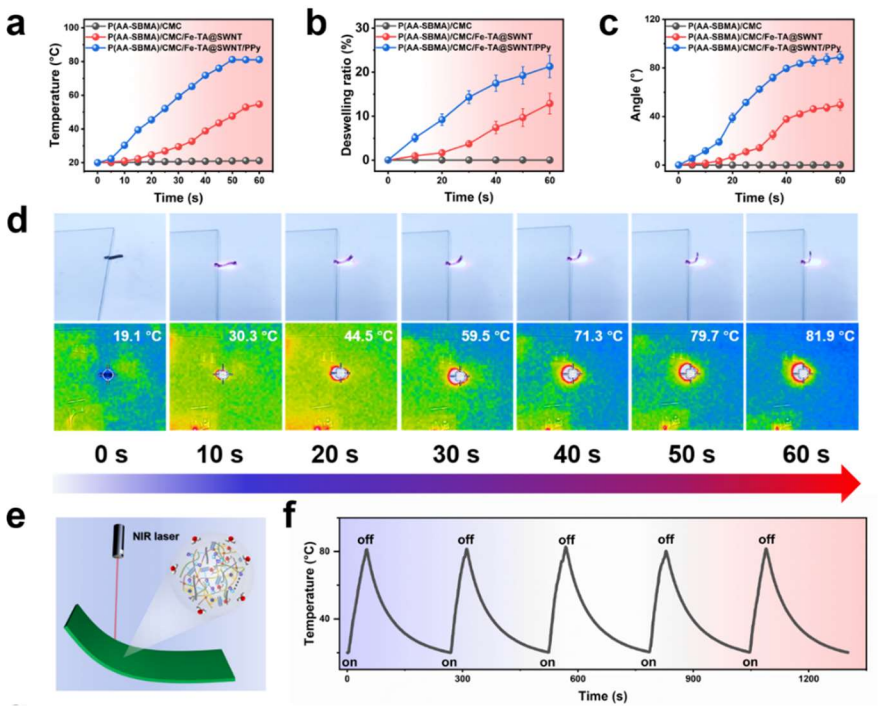


**Figure 3-4.** (a) Temperature-time, (b) Deswelling ratio-time, (c) Angle-time curves of the P(AA-SBMA)/CMC, P(AA-SBMA)/CMC/Fe-TA@SWNT and P(AA-SBMA)/CMC/Fe-TA@SWNT/PPy hydrogels under NIR irradiation. (d) NIR light responsive bending behavior of the P(AA-SBMA)/CMC/Fe-TA@SWNT/PPy hydrogel. (e) Schematic of the bending behavior of the P(AA-SBMA)/CMC/Fe-TA@SWNT/PPy hydrogel during NIR irradiation. (f) Temperature-time curves of P(AA-SBMA)/CMC/Fe-TA@SWNT/PPy hydrogel during five cycles of the turning on/off of the NIR irradiation.

than the temperature increase of P(AA-SBMA)/CMC/Fe-TA@SWNT hydrogel over the same period, indicating that the synergistic effect between Fe-TA@SWNT and PPy enhanced the photothermal performance of the hydrogel. Moreover, the reversible photothermal effect of the P(AA-SBMA)/CMC/Fe-TA@SWNT/PPy hydrogel was investigated by cyclically turning NIR light on/off. As depicted in **Figure 3-4f**, the surface temperature of the hydrogel remained stable over five cycles, demonstrating its exceptional photothermal stability. Furthermore, the extraordinary photothermal effect of hydrogels can readily induce volume phase transition.[21] When the temperature reaches or exceeds the volume phase transition temperature (VPTT) of the hydrogel, a volume phase transition occurs, resulting in the hydrogel shrinking and expelling water from its network.[57] The author also evaluated the deswelling behavior of the NIR light-triggered hydrogel. As shown in **Figure 3-4b**, the deswelling ratio of the P(AA-SBMA)/CMC/Fe-TA@SWNT/PPy hydrogel exceeded 20% after 60 s, significantly higher than the other two hydrogels. The deswelling behavior of the hydrogel induced by NIR light, combing with the high spatiotemporal precision of NIR light, easily induces anisotropic volume shrinkage, thereby achieving macroscopic shape folding deformation.[58] As anticipated, both the P(AA-SBMA)/CMC/Fe-TA@SWNT/PPy and P(AA-SBMA)/CMC/Fe-TA@SWNT hydrogels responded to NIR light by rapidly bending towards the light source. Particularly, the P(AA-SBMA)/CMC/Fe-TA@SWNT/PPy hydrogel exhibited a bending angle of over 85° after 60 s, while the P(AA-SBMA)/CMC hydrogel did not show significant bending behavior (**Figure 3-4c**). **Figure 3-4d** clearly demonstrate the NIR light-induced bending behavior of the P(AA-SBMA)/CMC/Fe-TA@SWNT/PPy hydrogel under localized NIR light irradiation, accompanied by a gradual increase in surface temperature. As shown in **Figure 3-4e**, this anisotropic bending behavior resembles the heliotropic movement of sunflowers, resulting from a faster temperature increase and more pronounced volume shrinkage on the irradiated side compared to the non-irradiated side.[29] This biomimetic motion confirms the potential

application of P(AA-SBMA)/CMC/Fe-TA@SWNT/PPy hydrogel in the field of biomimetic robotics.

Benefiting from the outstanding photothermal conversion capability of P(AA-SBMA)/CMC/Fe-TA@SWNT/PPy hydrogel, combined with its conductivity, the author developed an intelligent remote NIR light-controlled electrical switch. As depicted in **Figure 3-5a**, before NIR light exposure, the hydrogel was horizontally connected to the circuit, with the blue light-emitting diode (LED) remaining illuminated. Upon exposure to NIR light, the hydrogel electronic switch rapidly exhibited bending deformation, moving away from the blue switch to turn off the blue LED and ultimately connecting the green switch to illuminate the green LED. Furthermore, a NIR light-controlled hydrogel liquid microvalve was designed to remotely control liquid flow (**Figure 3-5b**). Columnar hydrogel was fixed in glass tubing to regulate the flow rate of the methylene blue solution above. Upon NIR light exposure, the gel valve occurred volume shrinkage, causing the liquid to flow rapidly downward, thereby achieving flow control. The results above indicate that the P(AA-SBMA)/CMC/Fe-TA@SWNT/PPy hydrogel have potential applications in fields such as smart soft actuators and soft robotics.

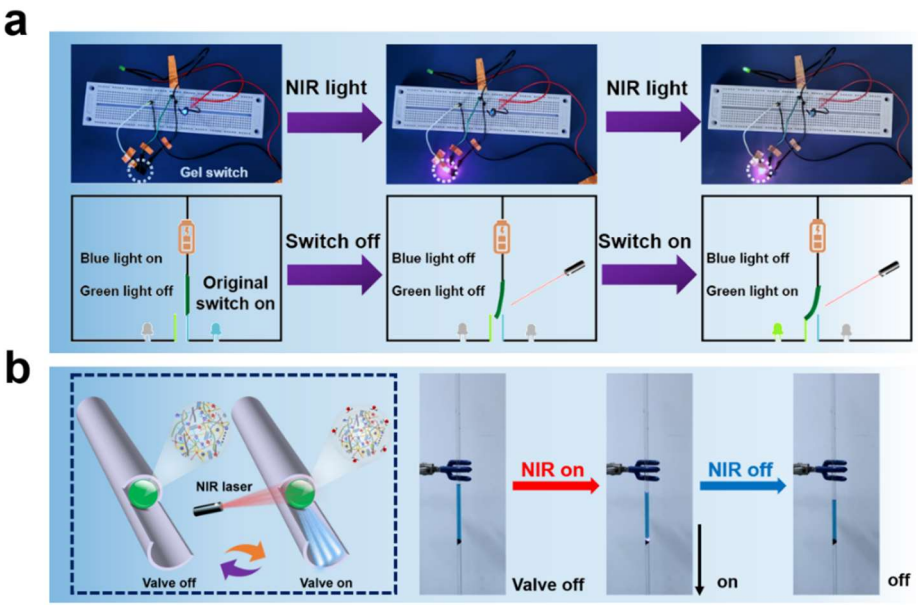


**Figure 3-5.** The application of P(AA-SBMA)/CMC/Fe-TA@SWNT/PPy hydrogel actuator. (a) As a smart electric switch and (b) as a liquid microvalve.

**Electromechanical Properties**

The conjugated PPy formed highly interconnected conductive pathways within the P(AA-SBMA)/CMC/Fe-TA@SWNT/PPy hydrogel, endowing it with excellent conductivity, reaching a conductivity of 1.24 mS/cm. As a result, this composite hydrogel could be assembled into strain sensors capable of detecting a wide range of strains. As indicated by **Figure 3-6a**, the brightness of the LED dimmed with increasing strain and then returned to its original state when the applied strain was removed, consistent with the change in resistance of the conductive hydrogel caused by mechanical deformation. This phenomenon could be attributed to the narrowing of the conductive pathways due to stretching, leading to an increase in resistance.[29] In other words, when a hydrogel material with a uniform conductive network is subjected to tensile strain, the average distance between the polymer molecular chains that constitute the hydrogel increases, resulting in an increase in material resistance. The gauge factor (GF) was used to evaluate the strain sensitivity of the

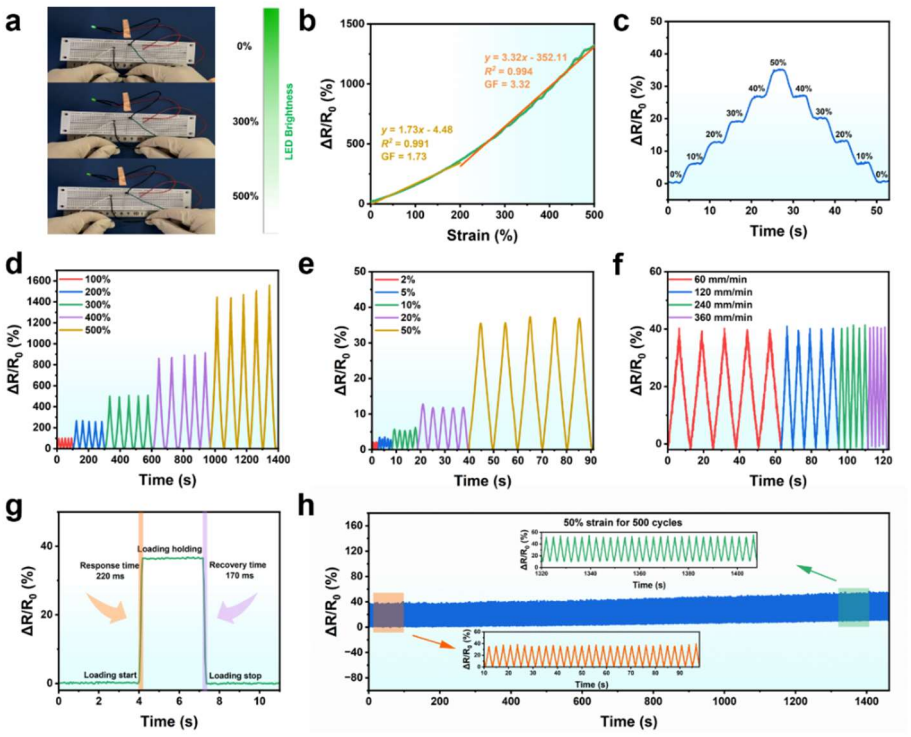


**Figure 3-6.** (a) Images depicting changes in brightness of an LED bulb at various levels of hydrogel elongation. (b) Relative resistance changes within the applied strains. (c) Relative resistance changes of the hydrogel during the incremental stretching and releasing process. Relative resistance changes of the hydrogel train sensor at various strain levels, (d) for large strain (100-500%) and (e) for small strain (2-50%). (f) Relative resistance changes of hydrogel with different stretching frequencies. (g) Response time and recovery time of the hydrogel sensor. (h) 500 cycling stability tests of the hydrogel sensor (0-50%).

strain sensors, defined as the slope of the relative resistance change versus strain. As shown in **Figure 3-6b**, the relative resistance change demonstrated a nearly linear increase within the strain range of 0-500%. Linear regression analysis was conducted on two segments of the GF curve, resulting in values of 1.73 (0-200%, $R^2$ = 0.991) and 3.32 (200-500%, $R^2$ = 0.994), respectively. This moderate GF values ensure that the hydrogel sensor maintains good conductivity over a wide range of strains, ensuring a stable and responsive electrical response during deformation.[59] Subsequently, the hydrogel sensor was subjected to stepwise changes in strain from 0 to 50% and then returned to 0%. Consequently, the relative resistance changing curves exhibited a distinct stair-stepping symmetric pattern with changes in strain, and no significant resistance hysteresis was observed in either the loading or unloading processes at specific strains (**Figure 3-6c**). Additionally, to assess the hydrogel sensor's response to various strains, strain sensing tests were conducted over a wide stretching range of 2-500%. As depicted in **Figure 3-6d-e**, the relative resistance change corresponded to the applied strain, indicating the sensor's ability to accurately and reversibly monitor electrical signals for both small and large strains. Taking into account dynamic responsiveness, the hydrogel exhibited consistent peak relative resistance values at various strain frequencies under a fixed strain of 50%, demonstrating reliable and rapid electromechanical response performance (**Figure 3-6f**). Besides, when the hydrogel was suddenly subjected to a large strain of 50% and rapidly unloaded, a fast response time (220 ms) and recovery time (170 ms) were detected (**Figure 3-6g**). This impressive response speed facilitates rapid and real-time monitoring of complex movements.[48, 60] As a flexible sensor, maintaining electrical stability during long-term strain cycles is a critical evaluation criterion in practical applications. As shown in **Figure 3-6h**, the hydrogel sensor underwent 500 cycles of loading and unloading tests at 50% strain. Throughout this process, the relative resistance changes for each cycle remained nearly constant, demonstrating satisfactory durability.

Therefore, benefiting from extraordinary electrical sensitivity and signal accuracy, the P(AA-SBMA)/CMC/Fe-TA@SWNT/PPy hydrogel meets the requirements as wearable sensors for monitoring physiological signals and motion states of the human body. As shown in **Figure 3-7e**, the author further assembled the hydrogel into strain sensors, which were then attached to different parts of the human body, recording the resistance signals to monitor physiological movements. In **Figure 3-7a**, when the hydrogel sensor adhered to the face of volunteers, it could clearly perceive facial tiny deformations, thereby identifying actions such as smiling, cheek-bulging, and chewing, with each action yielding repeatable waveforms. Similarly, when the hydrogel adhered to the throat, the vibrations of the vocal cords produced distinct and repeatable waveforms in the phrases "how are you" and "OK" uttered by volunteers, which can be easily identified by the sensor (**Figure 3-7c**). This speech recognition capability holds promise for the application of hydrogel sensors in vocal cord rehabilitation and human-machine interaction domains.[61] Besides, it was also suitable for sensing substantial limb movements during daily exercises. For instance, as the bending angle of the finger increased, the relative resistance signal output by the hydrogel sensor gradually increased (**Figure 3-7g**). Likewise, repetitive movements and actions of the neck (**Figure 3-7b**), elbows (**Figure 3-7h**), and knee joints (**Figure 3-7i**), as well as the magnitude, frequency, and even the rate of chest breathing (**Figure 3-7d**), could all be sensed by the hydrogel sensor and rapidly and accurately converted into corresponding changes in resistance signals for the potential diagnosis of joint disease. Additionally, the hydrogel sensors could facilitate the medical monitoring of subtle signals within the human body.[62] The sensor can detect stable electrocardiogram (ECG) signals when assembled as wireless ECG devices adhered to the human skin (**Figure 3-7f**). Additionally, owing to the hydrogel's sensitivity to subtle movements, the P(AA-SBMA)/CMC/Fe-TA@SWNT/PPy hydrogel can also serve as smart writing panels for handwriting recognition on their surface (**Figure 3-7j**). As shown in **Figure 3-7k-l**, when volunteers handwrote the

letters “X”, “Y”, “Z” and the word “APPLE” on the surface of the hydrogel, distinct and reproducible peaks were observed for each letter. In summary, the P(AA-SBMA)/CMC/Fe-TA@SWNT/PPy hydrogel shows significant prospect for monitoring human movements due to its excellent signal repeatability, stable electrical conductivity, and high sensitivity.

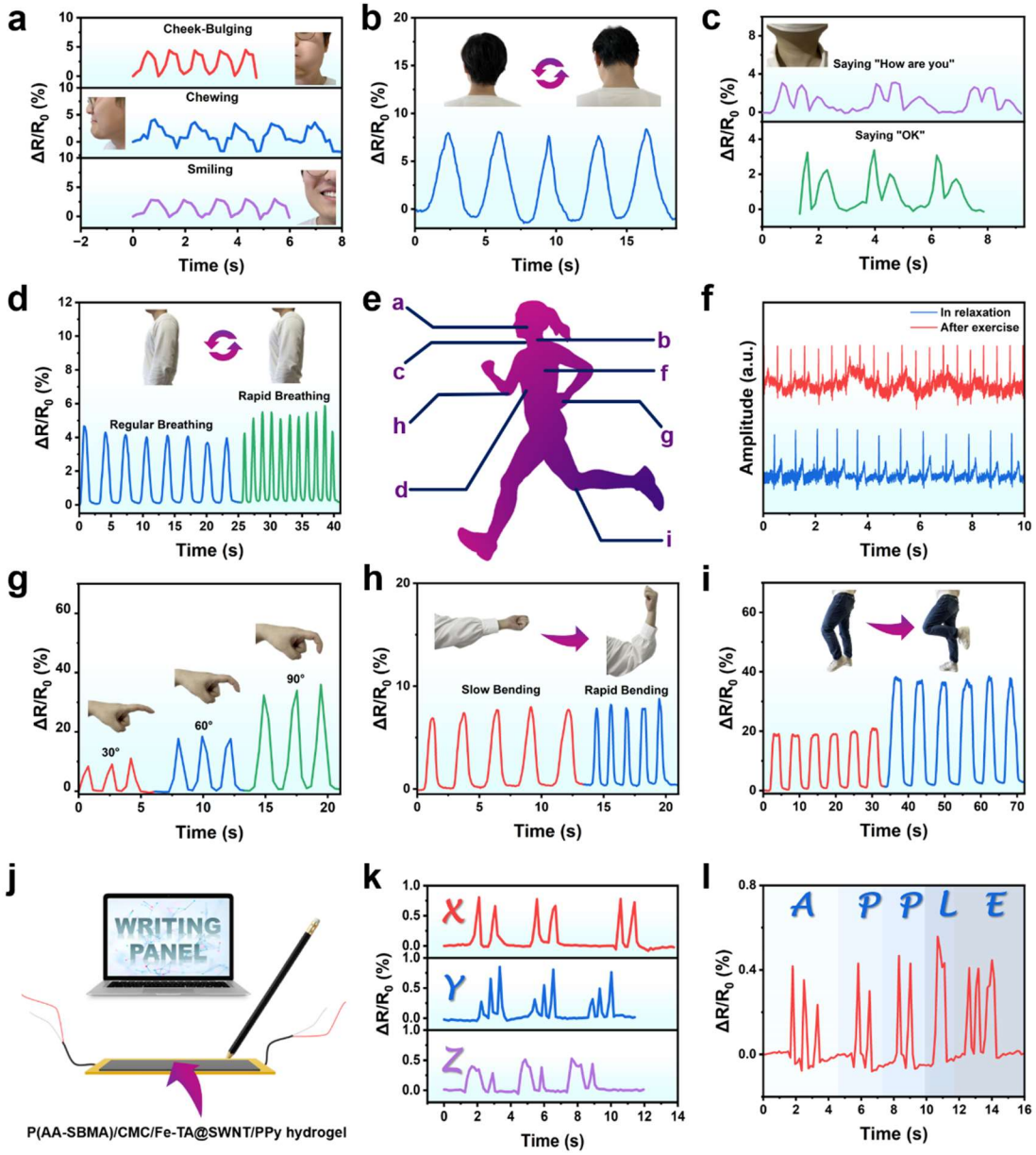


**Figure 3-7**. The application of the hydrogel as sensors for monitoring human activities and subtle physiological changes. (a) Monitoring facial expressions and movements. (b) Monitoring neck movements. (c) language identification. (d) Monitoring breathing. (e) Description of monitoring locations in human body. (f) ECG signals captured by the sensor. (g) Monitoring finger movements. (h) Monitoring elbow movements. (i) Monitoring knee movements. (j) Schematic diagram of the sensor for writing panel. Relative resistance changes for handwriting (k) “X”, “Y”, “Z” and (l) “APPLE”.

## 3.4 Conclusions

In summary, a multifunctional hydrogel sensor with integrated properties, including self-adhesion, NIR light responsiveness, and conductivity, was developed by incorporating iron-phenolic coordination complexes-coated SWNT and using $Fe^{3+}$ as an oxidizing agent to achieve in situ polymerization of conductive PPy polymer networks. Due to the synergistic effects of hydrogen bonding, electrostatic bonds, cation-π interactions and ion coordination bonds among Fe-TA@SWNT, CMC, PPy, and P(AA-SBMA), P(AA-SBMA)/CMC/Fe-TA@SWNT/PPy hydrogel exhibits high extensibility (1283.42%), remarkable self-recovery performance, and repeatable self-adhesive properties. At the same time, benefiting from the significant photothermal effect of Fe-TA@SWNT and PPy, the fabricated hydrogel actuators demonstrated repeatable photothermal conversion capability and efficient NIR light-triggered actuation behavior. Furthermore, based on the highly interconnected conductive channels formed by Fe-TA@SWNT and PPy within the hydrogel network, the hydrogel sensors exhibited high sensitivity (GF up to 3.32 within 500% strain) and rapid response capability (220 ms). Therefore, the hydrogel could be assembled into multifunctional strain sensors for real-time monitoring of various human motion at large and small strains, even capable of detecting subtle physiological signals such as vocal cord vibrations and heartbeats. It can also be utilized as a smart writing panel for information recognition. The author believe that this novel hydrogel can inspire the design and fabrication of next-generation NIR light-driven actuators, soft robots, wearable devices and smart information storage and recognition devices.

## 3.5 References

1. Y. Cai, J. Shen, C.-W. Yang, Y. Wan, H.-L. Tang, A. A. Aljarb, C. Chen, J.-H. Fu, X. Wei, K.-W. Huang, Y. Han, S. J. Jonas, X. Dong and V. Tung, *Sci. Adv.*, **6**, eabb5367.
2. A. Chortos, J. Liu and Z. Bao, *Nat. Mater.*, 2016, **15**, 937-950.
3. Y. Luo, M. R. Abidian, J.-H. Ahn, D. Akinwande, A. M. Andrews, M. Antonietti, Z. Bao,

M. Berggren, C. A. Berkey, C. J. Bettinger, J. Chen, P. Chen, W. Cheng, X. Cheng, S.-J. Choi, A. Chortos, C. Dagdeviren, R. H. Dauskardt, C.-a. Di, M. D. Dickey, X. Duan, A. Facchetti, Z. Fan, Y. Fang, J. Feng, X. Feng, H. Gao, W. Gao, X. Gong, C. F. Guo, X. Guo, M. C. Hartel, Z. He, J. S. Ho, Y. Hu, Q. Huang, Y. Huang, F. Huo, M. M. Hussain, A. Javey, U. Jeong, C. Jiang, X. Jiang, J. Kang, D. Karnaushenko, A. Khademhosseini, D.-H. Kim, I.-D. Kim, D. Kireev, L. Kong, C. Lee, N.-E. Lee, P. S. Lee, T.-W. Lee, F. Li, J. Li, C. Liang, C. T. Lim, Y. Lin, D. J. Lipomi, J. Liu, K. Liu, N. Liu, R. Liu, Y. Liu, Y. Liu, Z. Liu, Z. Liu, X. J. Loh, N. Lu, Z. Lv, S. Magdassi, G. G. Malliaras, N. Matsuhisa, A. Nathan, S. Niu, J. Pan, C. Pang, Q. Pei, H. Peng, D. Qi, H. Ren, J. A. Rogers, A. Rowe, O. G. Schmidt, T. Sekitani, D.-G. Seo, G. Shen, X. Sheng, Q. Shi, T. Someya, Y. Song, E. Stavrinidou, M. Su, X. Sun, K. Takei, X.-M. Tao, B. C. K. Tee, A. V.-Y. Thean, T. Q. Trung, C. Wan, H. Wang, J. Wang, M. Wang, S. Wang, T. Wang, Z. L. Wang, P. S. Weiss, H. Wen, S. Xu, T. Xu, H. Yan, X. Yan, H. Yang, L. Yang, S. Yang, L. Yin, C. Yu, G. Yu, J. Yu, S.-H. Yu, X. Yu, E. Zamburg, H. Zhang, X. Zhang, X. Zhang, X. Zhang, Y. Zhang, Y. Zhang, S. Zhao, X. Zhao, Y. Zheng, Y.-Q. Zheng, Z. Zheng, T. Zhou, B. Zhu, M. Zhu, R. Zhu, Y. Zhu, Y. Zhu, G. Zou and X. Chen, *ACS Nano*, 2023, **17**, 5211-5295.

4. J. Gao, Y. Fan, Q. Zhang, L. Luo, X. Hu, Y. Li, J. Song, H. Jiang, X. Gao, L. Zheng, W. Zhao, Z. Wang, W. Ai, Y. Wei, Q. Lu, M. Xu, Y. Wang, W. Song, X. Wang and W. Huang, *Adv. Mater.*, 2022, **34**, 2107511.

5. H. Wang, Q. Ding, Y. Luo, Z. Wu, J. Yu, H. Chen, Y. Zhou, H. Zhang, K. Tao, X. Chen, J. Fu and J. Wu, *Adv. Mater.*, 2024, **36**, 2309868.

6. Z. Fu, D. Li, H. Liu, R. Liu, Q. Lyu, Y. Han, Y. Wang, K. Zhang, G. Chen and Y. Tian, *Chem. Eng. J.*, 2024, **488**, 150775.

7. J. L. Guo, Y. S. Kim, V. Y. Xie, B. T. Smith, E. Watson, J. Lam, H. A. Pearce, P. S. Engel and A. G. Mikos, *Sci. Adv.*, **5**, eaaw7396.

8. Y. Cheng, K. H. Chan, X.-Q. Wang, T. Ding, T. Li, X. Lu and G. W. Ho, *ACS Nano*, 2019, **13**, 13176-13184.

9. Y. Zhang, K. Liu, T. Liu, C. Ni, D. Chen, J. Guo, C. Liu, J. Zhou, Z. Jia, Q. Zhao, P. Pan and T. Xie, *Nat. Commun.*, 2021, **12**, 6155.

10. M. Hua, S. Wu, Y. Ma, Y. Zhao, Z. Chen, I. Frenkel, J. Strzalka, H. Zhou, X. Zhu and X. He, *Nature*, 2021, **590**, 594-599.

11. Z. Qin, G. Zhao, Y. Zhang, Z. Gu, Y. Tang, J. T. Aladejana, J. Ren, Y. Jiang, Z. Guo, X. Peng, X. Zhang, B. B. Xu and T. Chen, *Small*, 2023, **19**, 2303038.

12. L. Pan, G. Yu, D. Zhai, H. R. Lee, W. Zhao, N. Liu, H. Wang, B. C. K. Tee, Y. Shi, Y. Cui and Z. Bao, *Proceedings of the National Academy of Sciences*, 2012, **109**, 9287-9292.

13. W. Qian, J. Texter and F. Yan, *Chem. Soc. Rev.*, 2017, **46**, 1124-1159.

14. T. Matsuda, R. Kawakami, R. Namba, T. Nakajima and J. P. Gong, *Science*, 2019, **363**, 504-508.

15. H. Li, Y. Liang, G. Gao, S. Wei, Y. Jian, X. Le, W. Lu, Q. Liu, J. Zhang and T. Chen, *Chem. Eng. J.*, 2021, **415**, 128988.

16. S. Li, H. Yang, N. Zhu, G. Chen, Y. Miao, J. Zheng, Y. Cong, Y. Chen, J. Gao, X. Jian and J. Fu, *Adv. Funct. Mater.*, 2023, **33**, 2211189.

17. L. Dong, A. K. Agarwal, D. J. Beebe and H. Jiang, *Nature*, 2006, **442**, 551-554.

18. L. Li, W. Zhang, Z. Ren, L. Chang, X. Xu and Y. Hu, *Chem. Eng. J.*, 2024, **479**, 147550.

19. P. Xue, H. K. Bisoyi, Y. Chen, H. Zeng, J. Yang, X. Yang, P. Lv, X. Zhang, A. Priimagi,

L. Wang, X. Xu and Q. Li, *Angew. Chem. Int. Ed.*, 2021, **60**, 3390-3396.
20. M. Li, F. Zhu, Y. Ge, J. Zhou, X.-M. Chen, W. Chen and N. Li, *ACS Mater. Lett.*, 2023, **5**, 1841-1850.
21. X. Zhang, L. Chen, C. Zhang and L. Liao, *ACS Appl. Mater. Interfaces*, 2021, **13**, 18175-18183.
22. S. Ma, P. Xue, C. Valenzuela, X. Zhang, Y. Chen, Y. Liu, L. Yang, X. Xu and L. Wang, *Adv. Funct. Mater.*, 2024, **34**, 2309899.
23. G. Ge, Y.-Z. Zhang, W. Zhang, W. Yuan, J. K. El-Demellawi, P. Zhang, E. Di Fabrizio, X. Dong and H. N. Alshareef, *ACS Nano*, 2021, **15**, 2698-2706.
24. M. Zhou, S. Liu, Y. Jiang, H. Ma, M. Shi, Q. Wang, W. Zhong, W. Liao and M. M. Q. Xing, *Adv. Funct. Mater.*, 2015, **25**, 4730-4739.
25. C. Lv, Z. Zhou, Y. Li, S. Lu and Y. Bai, *Chem. Eng. J.*, 2023, **477**, 147059.
26. C.-H. Zhu, Y. Lu, J. Peng, J.-F. Chen and S.-H. Yu, *Adv. Funct. Mater.*, 2012, **22**, 4017-4022.
27. Y. Li, X. Xie, Q. Zhu, S. Lu and Y. Bai, *J. Mater. Chem. A*, 2022, **10**, 22205-22213.
28. M. Kim, J. Choi and S. Y. Kim, *Mater. Today Chem.*, 2022, **26**, 101014.
29. X. Cui, Z. Liu, B. Zhang, X. Tang, F. Fan, Y. Fu, J. Zhang, T. Wang and F. Meng, *Chem. Eng. J.*, 2023, **467**, 143515.
30. C. Qian, Y. Li, C. Chen, L. Han, Q. Han, L. Liu and Z. Lu, *Chem. Eng. J.*, 2023, **454**, 140263.
31. I. Marangon, C. Ménard-Moyon, A. K. A. Silva, A. Bianco, N. Luciani and F. Gazeau, *Carbon*, 2016, **97**, 110-123.
32. X. Ding, Y. Yu, W. Li, F. Bian, H. Gu and Y. Zhao, *Nano Today*, 2024, **54**, 102124.
33. Y. Shi, L. Pan, B. Liu, Y. Wang, Y. Cui, Z. Bao and G. Yu, *J. Mater. Chem. A*, 2014, **2**, 6086-6091.
34. Y. Liu, Y. Gao, B. J. Kim, M. Xia, Y. Zhou, Y. Zhang, Y. Li, J. Huang, D. Cao, S. Zhao, J.-H. Ahn and Y. Lai, *SmartMat*, 2023, **n/a**, e1247.
35. C. Liu, R. Zhang, P. Li, J. Qu, P. Chao, Z. Mo, T. Yang, N. Qing and L. Tang, *ACS Appl. Mater. Interfaces*, 2022, **14**, 26088-26098.
36. D. Gan, L. Han, M. Wang, W. Xing, T. Xu, H. Zhang, K. Wang, L. Fang and X. Lu, *ACS Appl. Mater. Interfaces*, 2018, **10**, 36218-36228.
37. Y. Zhang, S. Li, Z. Gao, D. Bi, N. Qu, S. Huang, X. Zhao and R. Li, *Carbohydr. Polym.*, 2023, **315**, 120953.
38. J. Y. Oh, Y. Jung, Y. S. Cho, J. Choi, J. H. Youk, N. Fechler, S. J. Yang and C. R. Park, *ChemSusChem*, 2017, **10**, 1675-1682.
39. H. Zhao, S. Hao, Q. Fu, X. Zhang, L. Meng, F. Xu and J. Yang, *Chem. Mater.*, 2022, **34**, 5258-5272.
40. J. Wang, P. Du, Y.-I. Hsu and H. Uyama, *Chem. Eng. J.*, 2024, **480**, 148324.
41. P. Du, J. Wang, Y.-I. Hsu and H. Uyama, *ACS Appl. Mater. Interfaces*, 2023, **15**, 23711-23724.
42. H. Huang, J. Zhao and R. Liu, *J. Colloid Interface Sci.*, 2021, **582**, 396-404.
43. H. Fan, L. Wang, X. Feng, Y. Bu, D. Wu and Z. Jin, *Macromolecules*, 2017, **50**, 666-676.
44. Z. Tian, Z. Zhu, S. Yue, Y. Liu, Y. Li, Z.-Z. Yu and D. Yang, *Nano Energy*, 2024, **122**, 109276.

45. J. H. Kim, J. Y. Oh, Y. E. Shin, Y. C. Jeong, T. Kim, Y. Jung, J. S. Byun, S. J. Sung, C. R. Park and S. J. Yang, *Carbon*, 2019, **144**, 402-409.
46. S. Yamada, *Chem. Rev.*, 2018, **118**, 11353-11432.
47. J. C. Ma and D. A. Dougherty, *Chem. Rev.*, 1997, **97**, 1303-1324.
48. Z. Sun, C. Dong, B. Chen, W. Li, H. Hu, J. Zhou, C. Li and Z. Huang, *Small*, 2023, **19**, 2303612.
49. P. Du, J. Wang, Y.-I. Hsu and H. Uyama, *Chem. Mater.*, 2024, **36**, 1318-1332.
50. X.-F. He, Z.-F. Zeng, Q.-Y. Ni, Z.-C. Xu, P.-F. Mao, B. Jiang, Q. Wu, B. Wang, L.-X. Gong, L.-C. Tang and S.-N. Li, *Composites, Part B*, 2023, **266**, 111022.
51. S. Hao, C. Shao, L. Meng, C. Cui, F. Xu and J. Yang, *ACS Appl. Mater. Interfaces*, 2020, **12**, 56509-56521.
52. Y. Li, X. Liu, Y. Yang, C. Qian, C. Chen, L. Han and Q. Han, *Colloids Surf., A*, 2022, **636**, 128145.
53. C. Shao, H. Chang, M. Wang, F. Xu and J. Yang, *ACS Appl. Mater. Interfaces*, 2017, **9**, 28305-28318.
54. L. Zeng and G. Gao, *ACS Appl. Mater. Interfaces*, 2023, **15**, 28993-29003.
55. X. Zhang, C. Cui, S. Chen, L. Meng, H. Zhao, F. Xu and J. Yang, *Chem. Mater.*, 2022, **34**, 1065-1077.
56. D. Gan, W. Xing, L. Jiang, J. Fang, C. Zhao, F. Ren, L. Fang, K. Wang and X. Lu, *Nat. Commun.*, 2019, **10**, 1487.
57. C. Sang, S. Wang, X. Jin, X. Cheng, H. Xiao, Y. Yue and J. Han, *Carbohydr. Polym.*, 2024, **333**, 121947.
58. Y. Liu, Z. Zhang, Z. Liang, Y. Yong, C. Yang and Z. Li, *J. Mater. Chem. A*, 2022, **10**, 16928-16940.
59. M. Wu, M. Pan, C. Qiao, Y. Ma, B. Yan, W. Yang, Q. Peng, L. Han and H. Zeng, *Chem. Eng. J.*, 2022, **450**, 138212.
60. B. Song, X. Dai, X. Fan and H. Gu, *Journal of Materials Science & Technology*, 2024, **181**, 91-103.
61. S. Xia, Q. Zhang, S. Song, L. Duan and G. Gao, *Chem. Mater.*, 2019, **31**, 9522-9531.
62. Y. Gao, Y. Gao, Z. Zhang, Y. Wang, X. Ren, F. Jia and G. Gao, *J. Mater. Chem. C*, 2022, **10**, 12873-12882.

# Concluding remarks

In this doctoral thesis, three multifunctional smart hydrogels with excellent physical properties using a combination of rigid and flexible cellulose/synthetic polymers were constructed. These composite hydrogels not only exhibited excellent mechanical properties but also possessed characteristics such as fluorescence, self-healing, self-adhesion, and conductivity. Therefore, their applications are being explored in areas such as smart anti-counterfeiting, information storage, flexible wearable sensors, actuators, and smart handwriting panels.

In Chapter 1, the assembly of nano-cellulose hydrogel doped with naturally originated and multiple active sited carbon dots (CDs) was developed, using cellulose as a carrier for the CDs. The problem of CDs leaching from the hydrogel matrix was solved *via* strong chemical interactions between the CDs and cellulose nanofibers. The facilely prepared hydrogels showed extraordinary mechanical properties and fatigue resistance using uniaxial compression tests. Furthermore, this cellulose-based gel displayed bright green fluorescence under UV light, which could be quenched by $Fe^{3+}$ ions and recovered in an ascorbic acid/EDTA-2Na mixture solution. Therefore, coded information can be easily input and interpreted *via* ionoprinting technique, realizing a simple display and erasing procedure. This elaborately designed biomimetic hydrogel can serve as effective communication media to improve security and expand critical applications in optoelectronic storage devices.

In Chapter 2, cellulose nanocrystals (CNC) served as an important crosslinking point in the formation of the hydrogel and provided efficient self-healing functionality. Lignin sulfonate (LS)-$Fe^{3+}$ dynamic redox system was utilized to induce the generation of ammonium persulfate (APS) radicals at room temperature. Additionally, the polymerization of acrylamide (AM), sodium acrylate (AAS), and 3-acrylamidophenylboronic acid (APBA) formed polymer

networks through multiple dynamic crosslinking *via* the synergistic interactions of $Fe^{3+}$ and CNC. The dynamic and reversible boronic ester bonds, ion coordination bonds, and hydrogen bonds endowed the hydrogel with high stretchability, low hysteresis and efficient self-healing capability. Interestingly, the intermediate catechol groups generated by the LS-$Fe^{3+}$ dynamic catalytic system provided the hydrogel with repeatable and reliable adhesive performance. Due to the excellent ionically conductivity, the fabricated hydrogel-based sensors exhibited a wide sensing range, rapid response time, and high sensitivity, that accomplished specific voice recognition and subtle body motion detection for real-time elderly health and sleep management. This multifunctional hydrogel is of great significance for efficiently developing prolonged lifespan wearable electronics and healthcare flexible devices.

In Chapter 3, carboxymethylcellulose (CMC) serves as one of the molecular templates for controlling the in-situ formation of polypyrrole (PPy) inside the hydrogel networks. A multifunctional hydrogel composite with integrated sensing and actuating capabilities was proposed through the incorporation of $Fe^{3+}$-tannic acid (TA) coordination compound-coated carbon nanotubes (Fe-TA@SWNT) and the in-situ formation of conductive polymer PPy inside the hydrogel networks composed of CMC and a copolymer of acrylic acid (AA) and [2-(methacryloyloxy) ethyl]dimethyl-(3-sulfopropyl) ammonium hydroxide (SBMA). Benefiting from multiple effective dynamic interactions within the internal matrix, the prepared hydrogel exhibits excellent stretchability and toughness. Additionally, the catechol groups carried by Fe-TA@SWNT, along with the zwitterionic monomer SBMA, provide the hydrogel with repeatable self-adhesion performance. Based on the outstanding photothermal effect of Fe-TA@SWNT and PPy, the hydrogel demonstrates reversible and stable photothermal responsiveness, exhibiting exceptional actuation performance under near-infrared (NIR) radiation. As a strain sensor, the hydrogel shows excellent sensitivity, rapid response time, and reliable stability, enabling precise monitoring of various physiological signals in the human

body, including joint movements, facial expressions, and heartbeats. Therefore, this work significantly expands the application prospects of multifunctional smart hydrogels in fields of wearable electronics, soft robotics, and remote light-controlled devices.

In summary, this thesis designed and prepared a multifunctional hydrogel network system based on cellulose composites, and explored the applications of cellulose composite hydrogels in smart information storage, flexible sensors, dynamic health monitoring, and bio-inspired actuators. The author believes that this work provides new methods for designing environmentally friendly, sustainable, high-performance, and multifunctional flexible sensors.

# List of Publications

1. Cellulose Luminescent Hydrogels Loaded with Stable Carbon Dots for Duplicable Information Encryption and Anti-counterfeiting

**Juan Wang**, Peng Du, Yu-I Hsu* and Hiroshi Uyama*

ACS Sustainable Chemistry & Engineering, **2023**, *11*, 10061–10073.

DOI: 10.1021/acssuschemeng.3c01838.

2. Rapid Preparation of Dynamic-Crosslinked Nanocomposite Hydrogel Sensors with Efficiency Self-Healing and Adhesion Properties for Elderly Health and Sleep Management

**Juan Wang**, Peng Du, Yu-I Hsu*, and Hiroshi Uyama*

Chemical Engineering Journal, **2024**, *480*, 148324.

DOI: 10.1016/j.cej.2023.148324.

3. Smart Versatile Hydrogels Tailored by Metal-Phenolic Coordinating Carbon and Polypyrrole for Soft Actuation, Strain Sensing and Writing Recognition

**Juan Wang**, Peng Du, Yu-I Hsu*, and Hiroshi Uyama*

Chemical Engineering Journal, **2024**, *493*, 152671.

DOI: 10.1016/j.cej.2024.152671.

# Acknowledgments

The research presented in this thesis has been conducted at Uyama Lab., Department of Applied Chemistry, Graduate School of Engineering, Osaka University, from 2021 to 2024. I sincerely appreciate the immense support and guidance I have received from many individuals during this time.

First and foremost, I would like to express my deepest gratitude to Prof. Hiroshi Uyama. I am thankful for his funding support. I would also like to thank the other members of my thesis committee, Prof. Ken-ichi Nakayama and Prof. Masaya Nogi, for their insightful and constructive comments, as well as for the time they dedicated in the preparation of this thesis. I would also like to express my gratitude to the professors of the Materials Chemistry Course, Department of Applied Chemistry for taking the time to attend my doctoral thesis defense and providing many valuable suggestions. And I would like to thank Prof. Nobuhito Imanaka and Prof. Naoyoshi Nunotani. I appreciate their time and guidance on my “Research Proposal Seminar” course.

I am deeply grateful to Assoc. Prof. Yu-I Hsu for her insightful suggestions and inspiration that have significantly improved the quality of my research, as well as her continuous guidance and support in academic writing. I also appreciate her taking the time to patiently revise my thesis and for her warm care in my personal life. I am very grateful to Ms. Yoko Uenishi and Ms. Tomoko Shimizu for their assistance with my PhD program enrollment, participation in academic conferences, and the procurement of daily supplies and equipment for the laboratory. I would also like to extend my thanks to the support of past and present members in Uyama Lab: Prof. Dr. Jinjun Yang, Mr. Ruiqi Zhang, Mr. Yihan Gao, Mr. Yi-ho Chen, Mr. Xinyu Lou, Ms. Izzah Durrati Binti Haji Abdul Hamid, Ms. Sooyeon Noh, Ms. Shafinee Yarnina, Ms. Thuy Le Huynh An, Ms. Akane Odagaki, Ms. Chikako Abe, Ms. Erina Katsuragawa, Mr. Shunya

Kubo and Mr. Atsuki Takagi etc., for their kind-hearted help in my experimental and daily life. I am very grateful to Mr. Peng Du for his assistance with my research. I appreciate his contribution in providing experimental ideas, helping design experiments, assisting with hydrogel electrical sensing tests, and revising my thesis draft and defense slides. I wish you have new breakthroughs in your future research endeavors.

Finally, I would like to thank my parents deeply for their endless companionship and encouragement, allowing me to complete my doctoral studies without any concerns. I am also grateful for the scholarship grant of the Ministry of Education, Culture, Sports, Science and Technology (MEXT), Japan.

June 2024

Juan Wang